University of Alberta

Investigation of the Polymer Electrolyte Membrane Fuel Cell Catalyst Layer Microstructure

by

Peter Dobson

A thesis submitted to the Faculty of Graduate Studies and Research
in partial fulfillment of the requirements for the degree of

Master of Science

Department of Mechanical Engineering

Fall 2011
Edmonton, Alberta

To all who gave me their unconditional love and support...

Abstract

Computer modeling is critical for catalyst layer (CL) design in polymer electrolyte membrane fuel cells. Water-filled and ionomer-filled agglomerate models have been suggested as representations of the CL microstructure. In this thesis, improved water-filled and ionomer-filled agglomerate models are developed. Results indicate that the agglomerates provide identical current densities at low and high overpotentials, but differ at mid-range values. These models are integrated in a multiscale simulation of a 2D membrane electrode assembly (MEA) model. A comparative analysis shows that the choice of agglomerate alters the reaction distribution in the CL but does not significantly change the model's performance. Lastly, it is proposed that the CL microstructure be characterized by optimization-based parameter estimation, which matches MEA model predictions to experimental data. Results suggest that experimental data is not readily characterized by an agglomerate model; the MEA model requires more detail to describe the phenomena across a range of operating conditions.

Acknowledgements

I thank my supervisor, Dr. Marc Secanell, for giving me the opportunity to be a part of this research. His dedication, guidance, patience and encouragement were instrumental in the completion of this work.

I thank my colleagues in the Energy Systems Design Lab for sharing their ideas and making life around the lab a little easier.

I acknowledge the financial contribution and thank NSERC for continuing to support Canadian students and research.

Most importantly, I thank my family and friends who supported me through all my years of education and pushed me, *ever so gently*, to pursue this work and reach for something greater.

Contents

1 Introduction **1**

1.1 Background and Motivation 1

1.2 Fuel Cell Background 3

1.3 Literature Review 6

1.3.1 Cathode Catalyst Layer Models 7

1.3.2 PEM Fuel Cell Parameter Estimation 11

1.4 Contributions 15

1.5 Thesis Outline 15

2 Catalyst Layer Agglomerate Models **17**

2.1 Introduction 17

2.2 Ionomer-Filled Agglomerates 20

2.2.1 Governing Equations 21

2.2.2 Solution Methods 24

2.2.3 Model Validation 30

2.3 Water-Filled Agglomerates 33

2.3.1 Governing Equations 34

2.3.2 Solution Methods 37

2.3.3 Model Validation 38

2.4 Results and Discussion 38

2.4.1 Model Parameters 40

2.4.2 Agglomerate Performance 42

3 PEM Fuel Cell Modeling **54**

3.1 Introduction 54

3.2 Membrane Electrode Assembly Model 55

3.2.1 Governing Equations 59

3.2.2 Solution Method 70

3.2.3 Catalyst Layer Agglomerate Models 73

3.3 Results and Discussion 78

3.3.1 Characteristic Solution 78

3.3.2 Multiscale Validation 83

3.3.3 Water-Filled Agglomerate Multiscale Model 89

4 Catalyst Layer Parameter Estimation **95**

4.1 Introduction 95

4.2 Nonlinear Least-Squares Parameter Estimation 95

4.2.1 Problem Formulation 96

4.2.2 Solution Method 97

4.2.3 Experimental Setup 101

4.3 Results and Discussion 103

5 Conclusions and Outlook **112**

5.1 Conclusions 112

5.2 Outlook 115

Bibliography **118**

Appendices **125**

Appendix A Mathematical Derivations **126**

A.1 Ionomer-Filled Agglomerate Model 126

A.1.1 Formulation of Model Equations 126

A.1.2 Alternate Formulation 128

List of Tables

1.1 Review of Agglomerate Model Parameters 10

2.1 Electrochemical, transport, and global constants for the agglomerate simulations. 42

2.2 Operating conditions for three cases at which the agglomerate models will be compared 43

2.3 Results comparing the two types of agglomerate at the five reference cases. 48

3.1 List of subdomain names and abbreviations 60

3.2 Percolation constants for each of the subdomains used in the MEA simulations 69

3.3 Electrode geometry 80

3.4 GDL, MPL, CL, and Membrane physical properties 80

3.5 CL Structure and Microstructure by agglomerate type 81

3.6 GDL, MPL and CL transport properties 81

3.7 Catalyst layer electrochemical properties 82

3.8 Multiscale agglomerate validation. 87

4.1 Cell operating conditions 102

4.2 Electrode geometry 103

4.3 Results from least-squares parameter estimation for a single curve fit 104

4.4 Results from least-squares parameter estimation for fitting multiple curves 108

4.5 Quality of fit parameter by experimental curve 109

List of Figures

1.1 Schematic of a PEM Fuel Cell 3

1.2 3D reconstruction of the catalyst layer of a PEMFC by SEM imaging 8

1.3 Characteristic PEMFC polarization curve 12

2.1 High Resolution TEM image of agglomerate structure 18

2.2 Schematic of the catalyst layer agglomerate structure. 19

2.3 Schematic of the two types of agglomerates that are thought to exist within the catalyst layer. 19

2.4 Schematic of the ionomer-filled agglomerate and the assumed 3D domain used for modeling. 20

2.5 One-dimensional domain of a spherical agglomerate of radius r_{agg} and thin-film thickness of δ_{agg} 24

2.6 Validation of the numerical model against the analytical solution for oxygen concentration. 31

2.7 Comparison of the numerical and analytical agglomerate model current densities. 32

2.8 Schematic of the water-filled agglomerate and the assumed 3D domain used for modeling. 33

2.9 Validation of the water-filled agglomerate model. 39

2.10 Profiles of proton concentration and electrolyte potential within the water-filled agglomerate. 45

2.11 Reaction profiles within water-filled and ionomer-filled agglomerates. 46

2.12 Oxygen concentration profiles within water-filled and ionomer-filled agglomerates. 47

2.13 Comparison of the water-filled and ionomer-filled agglomerates. . . . 49
2.14 Comparison of the current density response for a water-filled agglomerates of differing oxygen reaction orders. 51
2.15 Comparison of water-filled agglomerates with differing reaction orders. 52
2.16 Response by the two models to changes in agglomerate size for a thin film thickness of 10nm. 53

3.1 Three dimensional representation of a single cell used for the simulation 55
3.2 Grid representation of the computational domain used for modeling the MEA 61
3.3 Membrane sorption isotherm and the resulting membrane conductivity 66
3.4 Curve fit of the oxygen diffusion coefficient in catalyst layers of differing porosities. 68
3.5 Flowchart for the implementation of a multiscale agglomerate model. 77
3.6 Gradient accuracy by step size for multiscale agglomerate models . . 79
3.7 Oxygen, water vapour, and electric potential distributions within the MEA 84
3.8 Electrolyte potential and membrane water content distribution in the ACL, PEM, and CCL 85
3.9 Oxygen, overpotential, and current density profiles in the cathode catalyst layer. 86
3.10 Grid study at two levels of convergence tolerance 88
3.11 Comparison of multiscale agglomerate models 90
3.12 Distribution of oxygen and water vapour within the cathode catalyst layer at 1.05 A/cm^2 92
3.13 Overpotential and current density profiles within the cathode catalyst layer at 1.05 A/cm^2 93

4.1 Schematic of the fuel cell analysis code and DAKOTA Optimization interface 98
4.2 Schematic of the dividing rectangles (DIRECT) optimization algorithm. 102

4.3 Single curve fit from least-squares parameter estimation 105
4.4 Multiple curve fit from least-squares parameter estimation 109
4.5 Kinetic region of multiple curve fit from least-squares parameter estimation 110

Nomenclature

A_v	Area utilized for the ORR per unit volume of CL ($cm^2\ cm^{-3}$)
a_w	Water activity
c_H^{ref}	Reference proton concentration ($mol\ cm^{-3}$)
$c_{O_2}^{ref}$	Reference Oxygen concentration ($mol\ cm^{-3}$)
c_H	Concentration of protons ($mol\ cm^{-3}$)
c_{O_2}	Concentration of oxygen ($mol\ cm^{-3}$)
$c_{SO_3^-}$	Concentration of sulphonic groups in Nafion ($mol\ cm^{-3}$)
c_{tot}	Total mixture concentration ($mol\ cm^{-3}$)
D_H^{eff}	Effective diffusivity of protons in porous media ($cm^2\ s^{-1}$)
$D_{H,N}$	Diffusivity of protons in ionomer (Nafion) ($cm^2\ s^{-1}$)
$D_{H,w}$	Diffusivity of protons in water ($cm^2\ s^{-1}$)
$D_{O_2,N}$	Diffusivity of Oxygen in ionomer (Nafion) ($cm^2\ s^{-1}$)
$D_{O_2,w}$	Diffusivity of Oxygen in water ($cm^2\ s^{-1}$)
$D_{O_2}^{eff}$	Effective diffusivity of Oxygen in porous media ($cm^2\ s^{-1}$)
E^{eq}	Equilibrium cell voltage (V)
E_0	Theoretical cell voltage (V)
EW	Equivalent weight of Nafion ($g\ mol^{-1}$)

F Faraday constant ($96,485\ \ C\,mol^{-1}$)

$H_{O_2,N}$ Henry's constant for O_2 in Nafion ($Pa\,cm^3\,mol^{-1}$)

i Local volumetric current in the agglomerate ($A\,cm^{-3}$)

i_0^{ref} Reference exchange current density ($A\,cm^{-2}$)

i_{agg} Volumetric current density per volume of agglomerate ($A\,cm^{-3}$)

i_{cell} Cell current density per facial area of catalyst layer ($A\,cm^{-2}$)

i_{CL} Volumetric current density per volume of catalyst layer ($A\,cm^{-3}$)

L^{cl} Catalyst layer thickness (cm)

L^{gdl} Gas diffusion layer thickness (cm)

L^{mpl} Micro-porous layer thickness (cm)

L^{m} Membrane thickness (cm)

L_{MEA} Membrane electrode assembly thickness (cm)

m_{Pt} Platinum mass loading per unit area in the catalyst layer ($g\,cm^{-2}$)

n Number of moles of the species per mole of reactant

n_d Electro-osmotic drag coefficient

N_j Flux of species j

n_{agg} Number of agglomerates per volume of CL (cm^{-3})

p Pressure (atm)

$Pt|C$ Mass percentage of Platinum on the support Carbon black

R Gas constant ($8.315\ \ J\,K^{-1}\,mol^{-1}$)

r_{agg} Radius of the agglomerate (nm)

T Temperature (K)

w Fixed charge density of a domain ($C\ cm^{-3}$)

W_{cc} Width of the current collector (cm)

W_{ch} Width of the gas channel (cm)

X_N Mass percentage of electrolyte (Nafion) in the catalyst layer ink

z_j Valency of species j ($C\ mol^{-1}$)

Greek Letters

α_c	Cathodic reaction transfer coefficient
δ_{agg}	Thickness of the ionomer thin film (nm)
ϵ_{agg}	Porosity of the agglomerate
η_c	Local cathodic overpotential (V)
γ_H	Reaction order wrt. protons
γ_{O_2}	Reaction order wrt. oxygen
λ	Membrane water content
ϕ_m	Electrolyte (membrane) phase potential (V)
ϕ_s	Solid phase (Electric) potential (V)
ρ_c	Density of Carbon ($g\,cm^{-3}$)
$\rho_{m,dry}$	Density of dry membrane ($g\,cm^{-3}$)
σ_m^{eff}	Effective conductivity of protons ($S\,cm^{-2}$)
ε	Relative permittivity
ε_0	Permittivity of free space ($8.854 \times 10^{-14}\ \ C^2 J^{-1} cm^{-1}$)
ε_N	Volume fraction of ionomer (Nafion) in the CL
ε_S	Solid phase volume fraction in the CL
ε_V	Porosity (Void volume fraction) of the CL
ε_W	Volume fraction of water-filled pores in the CL

Abbreviations

CCL Cathode Catalyst Layer

CL Catalyst Layer

GDL Gas Diffusion Layer

HOR Hydrogen Oxidation Reaction

MEA Membrane Electrode Assembly

MPL MicroPorous Layer

ORR Oxygen Reduction Reaction

PDE Partial Differential Equation

PEM Polymer Electrolyte Membrane

PEMFC Polymer Electrolyte Membrane Fuel Cell

PFSI Perfluorosulfonated Ionomer

STP Standard Temperature and Pressure

Chapter 1

Introduction

1.1 Background and Motivation

Models of fuel cells are frequently used as tools to understand the complex, interconnected processes that occur in fuel cell systems. Modeling is a critical step to fuel cell development, as it naturally leads to intelligent design, numerical optimization, and design validation in state of the art fuel cells [1]. This is especially true for the catalyst layer (CL) of polymer electrolyte membrane (PEM) fuel cells (PEMFC), where the size of the layer and fabrication of the membrane electrode assembly (MEA) make it very difficult to observe phenomena experimentally. Modeling, however, has its own challenges. Semi-empirical models can be used to describe and predict fuel cell performance but are typically zero-dimensional and do not provide enough detail to add to the understanding of the CL and MEA. Physical models can add layers of complexity but also contribute to uncertainty as an increasing number of equations are used to describe processes, each with their own uncertain parameters.

Much of the complexity in the model is due to the complex reaction process in the catalyst layer. In particular, the cathode catalyst layer (CCL) is the focus of many fuel cell modeling studies, as it is known to be one of the limiting factors to fuel cell performance. Plagued with slow reaction kinetics and a requirement for high catalyst loading, the CCL is a major contributor to the cost of PEMFCs and thus one of the barriers to short term commercialization. Over the past two decades numerical models of the CCL have moved from thin interface models, to homogeneous models, and most recently to agglomerate models. Each step represented a leap in complexity and required more sophisticated numerical modeling techniques.

Agglomerate models provide researchers with a method to describe the microstructure of the catalyst layer. Agglomerates are groupings of the particles sup-

porting the catalyst, and are bound together by the ionomer in the layer. These agglomerates are assumed to be the resultant structure of the layer after fabrication. They create a larger mass transport barrier, which leads to the low utilization of catalyst. Modeling the agglomerate processes, however, can be difficult as it creates a need to define the size, structure, transport, and kinetics. This adds complexity and more parameters to the model that must be determined.

In most cases, choices of parameters used to describe these complex processes are based on literature surveys or approximate trends of performance at a limited sample of operating points. As a result, it is difficult to find input parameters that are valid over a large range of operating conditions. Researchers attempt to determine parameter values in the governing equations by matching experimental data. In the case of fuel cells, polarization curves, impedance spectroscopy, water balances, and segmented cells can be used to test model behavior. In general, however, the polarization curve, or I-V curve, is the most common data used to fit parameters. Parameter estimation in the vast majority of published works comes from trial-and-error processes or parametric studies; there are very few attempts in the literature to systematically determine model parameters. Since fuel cell models are highly non-linear, regression analysis is not sufficient and optimization-based, nonlinear least-squares parameter estimation techniques are the best option for characterizing physical, structural, and electrochemical parameters. These methods demand large computational resources as they require many function evaluations. Generally, gradient based algorithms are best suited to least-squares problems but any algorithm may be used successfully. As models become more complex, these methods become prohibitive, as each function and gradient evaluation can be time consuming.

The objective of this thesis is to develop a framework for numerical optimization and parameter estimation in order to characterize the microstructure of the catalyst layer using an agglomerate model. As there are several proposed agglomerate models, the first goal is to analyze the existing models for clarity and understanding. They will then be enhanced by applying new knowledge and understanding of the catalyst layer. It is then proposed to use a full MEA model to estimate the size and structure of agglomerates by nonlinear least-squares parameter estimation. The results will not only attempt to characterize the catalyst layer microstructure, but the developed framework will provide researchers with a method to validate models and determine multiple uncertain parameters using a set of physical data.

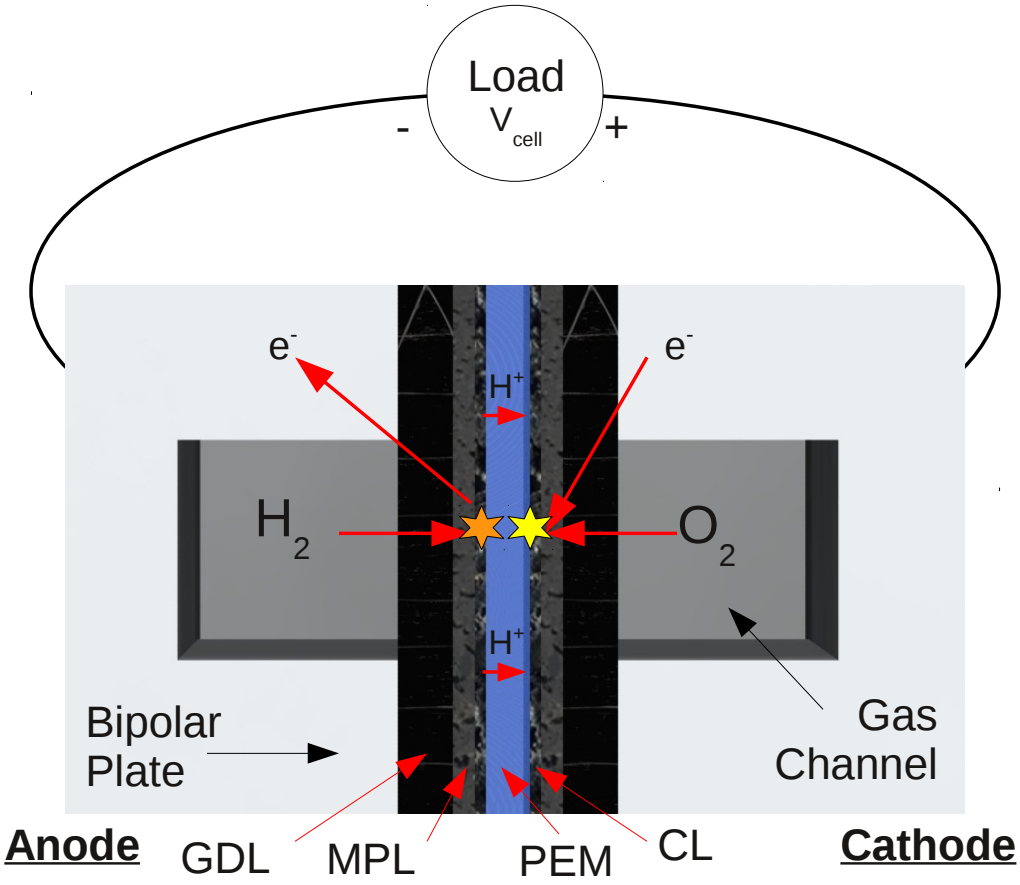

Figure 1.1: Schematic of a PEM Fuel Cell

1.2 Fuel Cell Background

The basic function of a fuel cell is to convert the chemical energy in a fuel to electrical energy by an electrochemical reaction, rather than to heat by combustion. Fuel cells come in many types and configurations and can use various types of fuel. In this work, the PEM fuel cell is considered, which uses hydrogen as its fuel. Much like combustion, the overall chemical process that occurs in a PEMFC is the conversion of hydrogen and oxygen to water.

$$O_2 + 2H_2 \rightleftharpoons 2H_2O \tag{1.1}$$

The electrical energy in the reaction is harnessed by isolating the half-cell reactions (equations (1.2) and (1.3)) and passing the current around an external circuit. Figure 1.1 shows a schematic of the construction and processes in a single cell PEMFC. The cell is arranged into the anode and cathode, which are constructed in a similar manner. An end plate (bi-polar plate) houses the gas channels which

transport the reacting gases to the individual cell. Between these end plates is the membrane electrode assembly. The first layer is the gas diffusion layer (GDL), typically a very porous, fibrous layer that allows the gas to diffuse towards the electrode while distributing more evenly under the current collector portion of the bi-polar plate. In many cells, the layer that follows is a microporous layer (MPL). This layer is constructed out of a solid conductive, but porous material that has been treated so that the pores are hydrophobic. This is thought to help expel liquid water that may accumulate in the electrode. The final layer of the electrode assembly is the catalyst layer (CL), where the reaction occurs. Naturally, the requirement is that the layer contains the catalyst that allows the reaction to proceed. There are many proposed constructions for the CL, from an ultra-thin layer of catalyst deposited on the membrane, to nano-structured layers, to thicker porous layers similar to the MPL [2]. The CL, however, must also allow for the transport of protons, electrons, and gases, which all must be present at the catalyst surface for a reaction to occur. Electrons may travel through the solid phase, but the layer must also be porous to allow for gas transport. Lastly it must contain an electrolyte for the transport of protons. The most common electrolyte used is a perfluorosulfonated ionomer (PFSI), typically Nafion® - a product offered by manufacturer DuPont™.

The anode and cathode electrodes are separated by a membrane, whose function it is to separate the reactant gases and transport the ionic reaction intermediates - in this case protons to the cathode. Thus, the membrane must be impermeable to gases while being a good conductor of protons. This material is typically a Polymer Electrolyte Membrane (usually Nafion), hence the acronym PEM, which characterizes and lends its name to the cell (although a commonly used alternative to the acronym is a proton exchange membrane). Multiple cells can be connected in series, separated by the current collector, i.e. the bi-polar plate. Gas channels on either side of the plate facilitate construction, assembly, and the distribution of gases during operation.

Once hydrogen flows out of the gas channels and through the diffusive layers, it is oxidized at the anode catalyst layer (ACL) by equation (1.2), the hydrogen oxidation reaction (HOR). The electrons flow back through the solid network in the diffusion layers, into the current collector plate and around an external circuit (through a load) to the cathode. Protons generated by the reaction are allowed to pass through the membrane separating the anode and cathode catalyst layers. In the

cathode, protons, electrons, and oxygen flowing in from the gas channel combine to form water, as shown in equation 1.3. This is know as the oxygen reduction reaction (ORR).

$$2H_{2(g)} \rightleftharpoons 4H^{+}_{(aq)} + 4e^{-} \tag{1.2}$$

$$O_{2(g)} + 4H^{+}_{(aq)} + 4e^{-} \rightleftharpoons 2H_2O_{(l)} \tag{1.3}$$

The amount of energy given by this process is determined by the work potential of the reactions. From a thermodynamic perspective, the maximum theoretical electrical cell potential can be obtained from the change in Gibbs free energy.

$$E_0 = \frac{-\Delta G}{nF} \tag{1.4}$$

At standard temperature and pressure (STP), this potential is $1.229\,V$. If the reaction does not proceed at STP, the thermodynamic equilibrium shifts and is governed by the Nernst equation [3]

$$E^{eq} = E_0 + \frac{\Delta s}{nF}\left(T - T_0\right) + \frac{RT}{nF}\ln\left(p_{H_2}\, p_{O_2}^{1/2}\right) \tag{1.5}$$

Potentials that differ from this point will drive the reaction in a specific direction. Applying a load at a lower voltage will draw current and consume hydrogen. Applying higher voltages will reverse reaction (1.1) and produce hydrogen. The half-cell reactions are governed by different reaction kinetics, but for the cell to be in equilibrium, must produce the same total current. Therefore, the shift in the equilibrium potentials, or overpotentials, will be different in the anode and cathode. The HOR is characteristically a fast reaction, and is used in many electrochemical electrode potential tables as a reference reaction (the standard hydrogen electrode). The ORR at the cathode is a much slower reaction, and contributes to most of the kinetic losses in the cell by requiring large overpotentials to proceed. The focus of this work is on the cathode ORR, which will be described in detail in the following sections and chapters. The HOR is only briefly described in Chapter 3.

The spontaneous reaction in the cathode occurs at negative overpotentials, defined as $\eta = E - E^{eq}$. This reaction, however, is a multi-step process as the 4 electrons are consumed in the reaction. From Sun et al. [4], it is assumed that the reaction can be described by Butler-Volmer Kinetics. For this assumption to be

made, it must also be assumed that the overall reaction rate is governed by a single limiting intermediate reaction, called the rate determining step (RDS). Furthermore, this rate determining step must be free to proceed uninhibited by other reactants. This means that catalyst surface be available for the reaction and therefore must be nearly completely free of intermediate species or contaminates. If these conditions are met, the reaction can be described by

$$i = i_0 \left[\left(\frac{c_{O_2}}{c_{O_2}^{ref}} \right)^{\gamma_{O_2}} \left(\frac{c_H}{c_H^{ref}} \right)^{\gamma_H} \exp\left(\frac{-\alpha_c F}{RT} \eta \right) - \exp\left(\frac{\alpha_a F}{RT} \eta \right) \right] \tag{1.6}$$

By this definition, the reaction will proceed at a different rate depending on reactant concentrations, where the order of this change, γ, is determined by the reaction pathway. Similarly, the transfer coefficients, α, are determined by the electrochemical reactions in the pathway, and the transfer coefficient of the RDS. There are many proposed reaction pathways and it is still unclear which mechanism, or combinations thereof, govern the ORR kinetics. Walch et al. [5] provide a thorough review of proposed mechanisms for the ORR reaction as they introduce their model and discuss non-electrochemical reactions in the cell. Recently, Shi et al. [6] also discussed these mechanisms in the context of contamination and how this may affect the reaction. Many theoretical and modeling works [7–11] cite the experimental work by Parthasarathy et al. [12, 13] and Sepa et al. [14] where it is shown that the order of the reaction with respect to oxygen concentration is 1, and that there are two distinct regions where the order of the reaction with respect to proton concentration and the cathodic transfer coefficient change - a low current density region where $\gamma_H = 1.5$ and $\alpha_c = 1.0$, and a high current density region where $\gamma_H = 1.0$ and $\alpha_c = 0.5$. There is still no agreement over what the value of the transfer coefficient should be, and values spanning from 0.5 to 2.0 have been used to describe the reaction [7]. Furthermore, numerical studies where γ_H differs from unity have not been discovered. In fact, due to the presence of Nafion, many models ignore the effect of proton concentration, as it is assumed to be uniform within the layer and thus never varies from the reference condition. There are many ways to model the catalyst layer, some of which will be described in the following section.

1.3 Literature Review

This section provides a review of the literature and background information on the relevant aspects of this work. Section 1.3.1 is a review of PEMFC modeling with

a focus on the cathode catalyst layer. Herein, the developed agglomerate models will be discussed, with particular focus on their use within the CCL. The discussion in section 1.3.2 will shift to a review of the specific application of nonlinear least-squares parameter estimation using high-fidelity physical PEMFC models.

1.3.1 Cathode Catalyst Layer Models

The content of this thesis has its focus on a two-dimensional model of an MEA. Therefore, the review of the literature will only concern itself with high-fidelity, physical, dimensional models of fuel cell electrodes. Zero-dimensional, empirical, or so-called 'black box' heuristic models will be ignored, as they are best suited for other applications, such as system modeling or control. For electrode models at the single cell level, the approximation of the catalyst layer has grown vastly in complexity over the last few decades. In early studies where the catalyst layer was not the focus, it was appropriate to define it as a thin interface where the flux of species and cell current could be defined [15]. This method is still applied for three-dimension flow analysis and optimization by authors such as Grujijic et al.[16]. Conventional catalyst layers, however, have a finite thickness of approximately $10\mu m$. The layer is fabricated with a solid conductive material that supports a catalyst. This is called a catalyst support particle, and is conventionally platinum on carbon nanoparticles($Pt|C$), which are approximately 30nm in size. An electrolyte (PFSI, usually Nafion®), is used to bind the solid particles and to promote proton transport throughout the layer. The mixture, or catalyst ink, is applied to a membrane and dried, forming the pores required for gas transport. Figure 1.2 shows a segment of a catalyst layer from a recent study by Thiele et al. [17] that has been digitally reconstructed using a technique involving a focused ion beam - scanning electron microscope (FIB-SEM). The figure shows the random structure of the layer, with pore space as the dark segments, and the remaining structure is the solid and electrolyte network.

When the entire layer is assumed to be a uniform mixture of solid, electrolyte, and pores, the model is called a macrohomogeneous, or pseudo-homogeneous catalyst layer model. Each of the reactants are transported in a single phase: oxygen through the pores, protons through the electrolyte, and electrons through the solid network. The reaction can only take place on the surface of the catalyst when all three reactants are present. Therefore, there must be contact between all three

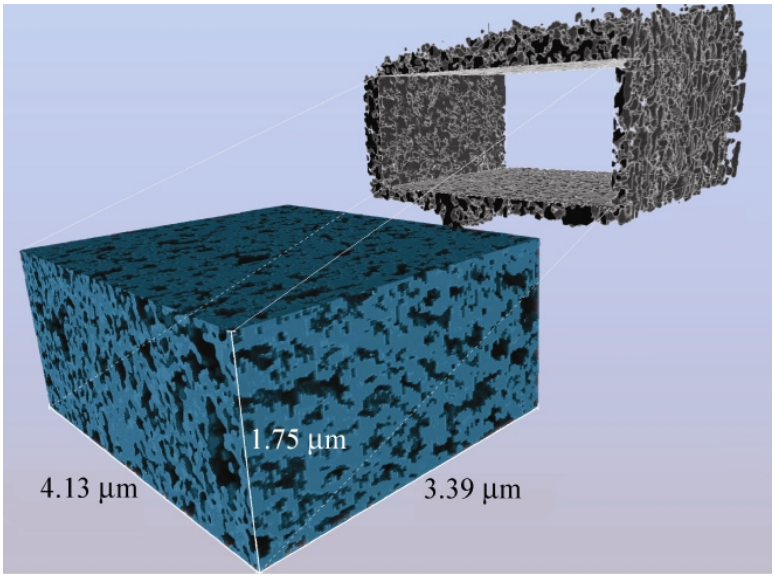

Figure 1.2: 3D reconstruction of the catalyst layer of a PEMFC by SEM imaging from Thiele et al. [17]. The SEM captures 2D images as the FIB cuts away small sections. The 3D image is the result of an overlay of many 2D images. The dark regions in the extracted segment represent the pores, while the remaining structure is the solid and electrolyte network. Note that these two phases cannot be visually separated by the FIB-SEM.

phases. This will not be a common occurrence and it is likely that oxygen must dissolve in order to reach the reaction site. Oxygen can then be transported by two different mechanisms. In early models, it was not known whether oxygen was transported in liquid water flooding the CL pores [18–20], or transported through gaseous pores and reacted at a solid/electrolyte interface [21–25]. These two assumptions lead to dramatic differences in the transport resistance of oxygen within the catalyst layer. The latter, however, lead to the necessity to define the microstructure, and thus development of agglomerate models.

In agglomerate models, the network shown in Figure 1.2 is assumed to be comprised of interconnected groups of solid and electrolyte. It is suggested that during fabrication the carbon particles aggregate and form clusters, or agglomerates, with the long ionomer chains acting as a binder and maintaining the structure of the overall layer [10]. It is postulated that mass transport limitations inhibit the reaction towards the center of the agglomerate, thus low catalyst utilization. There are two overarching assumptions for the mechanisms behind this limitation. One assumption is that the ionomer penetrates the micropores in the agglomerate (known

as primary pores) and facilitates proton transport in the agglomerate. It can then be assumed that for the size of the agglomerate (0.1-1 μm diameter) that the overpotential is constant. The limiting factor is then oxygen transport to the center of the agglomerate. There are many examples of this type of implementation in numerical modeling [4, 7, 26–34]. The second assumption is that the primary pores are filled with water, and studies that model this process are few [7, 35]. Diffusion, rather than conduction drives the transport of protons towards the center of the agglomerate. A distribution of protons then induces an electric field within the agglomerate, which inhibits the transport of protons to the center, but increases the overpotential. These two balancing factors will contribute to the overall reaction rate but determining which process dominates depends on reaction kinetics [7]. The complex water-filled model has only been analyzed in the context of the catalyst layer in one work [35]. The lack of an analytical solution requires that a second set of partial differential equations (PDEs) must be solved to calculate the current density. Such a multiscale implementation is taxing and therefore the only CL model with this configuration is one-dimensional [35].

From the earliest implementations of the catalyst layer agglomerate model, it was noted that a better fit of experimental data could be obtained [26, 36]. Extra parameters are used to characterize the size and structure of the agglomerates: the radius (r_{agg}), the porosity (ϵ_{agg}), and the thickness of a thin film of ionomer over the agglomerate (δ_{agg}). While there are many studies that use such a model, a unique set of parameter values has not yet been established which characterizes the catalyst layer over a wide range of operating conditions. In numerical studies, the range of reported values for the agglomerate size alone is large, with radii simulated from 50nm to 1μm [4, 7, 32, 33, 37, 38]. Table 1.1 provides a summary of recent agglomerate models and the wide range of structural parameters that have been used. These values should be consistent with microscopy studies presented in the literature. In a recent study by Ma et al. [39], it is suggested that the carbon support particles of diameter of 30-40 nm aggregate to form grains of 100-120nm. This is in agreement with SEM images shown in an agglomerate modeling study by Rao et al. [40]. There is also little consistency in the value of the thin film thickness and agglomerate porosity, which cannot be seen through microscopy.

In previous agglomerate model studies, the agglomerate structure and composition was changed independently of the macroscopic properties in the CL. This may

Table 1.1: Review of Agglomerate Model Parameters

Author	r_{agg}, [nm]	δ_{agg}[nm]	ϵ_{agg}
Broka [26]	$1000 - 5000$[1]	-	-
Chan[41](see Broka)	1000	-	-
Chen[42]	1000	80	-
Das[43]	2500	-	0.4
Eikerling[32]	100-200	-	0.19
Gerteisen[37]	200	-[2]	0.4
Gode[44]	100	0	0.11-0.45
Ihonen[28]	110	0	0.38
Jain[38]	1000	80	0.5
Jaouen[27]	500	0-50	0.3
Kamarajugadda[45]	50-1000	0-100	0.2-0.5
Perry[46]	100	-	-
Madhusudana Rao[40]	100-1000	5-50	0.1-0.5
Secanell[33]	250-1000	0-80	0.5
Siegel[29]	3000	-	-
Shah[31, 47]	200	15	0.2
Sui[36]	1000-5000	-	-
Sun[4]	1000	80	0.5
Wang, Q.[7]	50-200	-	0.3
Xia[35]	100	10	0[3]

Notes:
1. r_{agg}=1-5μm Observed with SEM.
Model uses agglomerate characteristic length L = $\frac{r_{agg}}{3} = 3\mu m$
2. Thickness of film varies with water content
3. Water filled agglomerate

lead to unrealistic CL compositions. For example, if the size of the agglomerate is increased while maintaining the amount of electrolyte inside the agglomerate and the thin film thickness constant, an increase in the total amount of ionomer in the CL must be accounted for. When considering such changes, it becomes clear that there is only a small range of agglomerate sizes and compositions for which the total volume fraction of electrolyte in the CL is within reasonable values for conventional catalyst layer construction, e.g. 10-50% of the CL volume. Using the structure and composition of agglomerates in reference [4], reducing the radius of the agglomerate by half, which has been commonly done in previous studies, results in electrolyte volume fractions of more than 80%. This is clearly unreasonable. Previous studies in the literature that have compared the macrohomogeneous and agglomerate models [9, 26, 48] have all modified the microscale and macroscale input parameters in the

two models independently of each other. Relations developed by Secanell et al. [33] linking the microstructure to macroscale volume fractions can add consistency and reduce uncertainty in the model, but are not widely used. Kamarajugadda and Mazumder [45] have presented studies to numerically analyze the effect of cathode structure and composition. They note the change in macroscale properties (using the relations developed by Secanell et al. [33]) while they independently vary agglomerate parameters. The results of such a methodology provides insight into the coupling between the agglomerate parameters and catalyst layer composition, but they focus on cell performance with respect to macroscale transport properties.

Based on the discussion above, a gap in the literature can be identified for the analysis of agglomerate models in catalyst layers with geometrical constraints, specifically in the application to a water-filled agglomerate model. Only a single study exists for the direct comparison of the two types of agglomerates [7], and none in the context of a catalyst layer. Agglomerate models are not completely understood; the scope of the analysis in the literature allows for further investigation.

1.3.2 PEM Fuel Cell Parameter Estimation

As a part of the modeling procedure, input parameters must be chosen that define the model appropriately in relation to experimental results. In fuel cell modeling, the polarization curve, or I-V curve, is the most commonly used measure to fit models. The polarization curve for a fuel cell is the voltage-current response across the full range of operating conditions, and has a characteristic shape for a PEM fuel cell, as shown in Figure 1.3. At low current densities, the reaction is dominated by the kinetics, and therefore the losses are exponential. Once the current density increases, the losses are dominated by charge transport, or ohmic losses through the membrane. Finally, at high current densities, mass transport becomes the largest source of loss, as reactants are not transported to the reaction sites at a high enough rate. Typically, oxygen transport is limiting through the porous layers of the cathode, but the limitation may also be at the nano-scale in the CL.

Parameter estimation in the vast majority of published works comes from trial-and-error processes or parametric studies to fit data to the experimental curves. Numerous studies aim to optimize the electrodes for performance [11, 33, 38, 49–56] using numerical techniques; however, there are very few attempts to systematically estimate the parameters used in the model. For non-linear models, parameter esti-

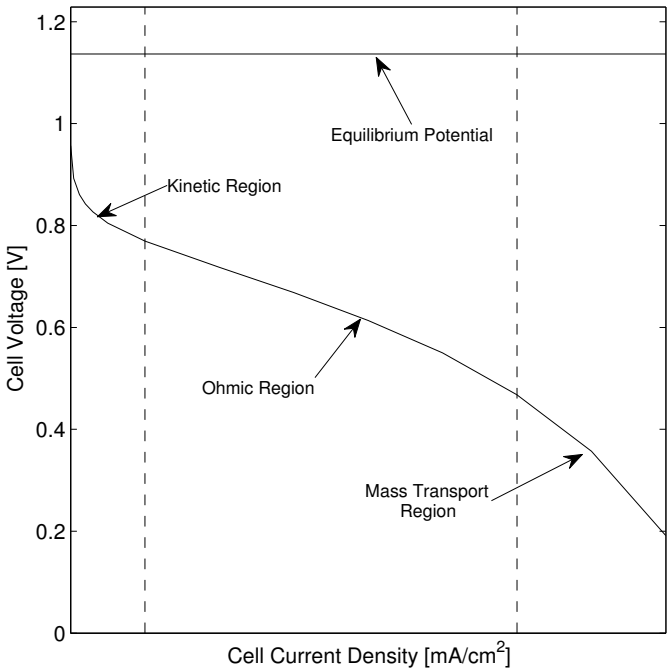

Figure 1.3: Characteristic PEMFC polarization curve showing the typical regimes. The theoretical cell voltage is 1.229V, but the equilibrium voltage drops due to the operating conditions. The three typical regimes are shown. The kinetic losses from the equilibrium potential occur all in the kinetic region. At higher currents, ohmic losses through the membrane have an effect and produce a linear drop in voltage. In the mass transport region, diffusion resistance prevents the reactants from reaching the catalyst sites until a limiting current is reached. The value of the limiting current depends on the cell construction and operating conditions

mation must be done using the same types of optimization methods, as regression analysis will not suffice. Optimization is a method where a set of parameters (or design variables) is manipulated in order to maximize or minimize a chosen objective function, $f(\vec{x})$, subject to a set of equality and inequality constraints, $h_i(\vec{x})$ and $g_i(\vec{x})$. A general formulation is [1]

$$\begin{array}{lll} \text{Minimize} & f(\vec{x}) & \\ \text{w.r.t.:} & x_k & \text{for } k = 1, 2, \ldots, n \\ \text{subject to:} & h_i(\vec{x}) = 0 & \text{for } i = 1, 2, \ldots, p \\ & g_j(\vec{x}) \leq 0 & \text{for } j = 1, 2, \ldots, q \\ & \vec{x}_L \leq \vec{x} \leq \vec{x}_U & \end{array} \tag{1.7}$$

With a fuel cell model, there are many different objectives that could be optimized, such as performance or cost [1]. In order to estimate parameters, a typical least-squares formulation for parameter estimation will minimize the error between experimental data and model predictions. This is accomplished by manipulating the model input parameters such that the total residual is driven to zero. A generic least-squares formulation is

$$\begin{array}{ll} \text{minimize:} & \frac{1}{2} \sum_{i=1}^{n} \left[r_i \left(\vec{x} \right) \right]^2 \\ \text{w.r.t:} & \vec{x} \\ \text{s.t:} & x_j^{lb} \leq x_j \leq x_j^{ub} \end{array} \tag{1.8}$$

where r_i is the residual at point i between the model and experimental values, and x_j are the parameters to be estimated. There are many different methods and algorithms to solve the optimization, and the best choice is problem dependent.

Optimization-based parameter estimation in fuel cells is limited to a few recent studies. Berg et al. [57] use a one-dimensional along-the-channel PEFC model to fit data to multiple I-V curves independently. They estimate the exchange current density, oxygen mass transfer coefficient, water diffusivity and membrane conductivity, by simulating data at points along the channel. The residuals are the cell voltage differences between the model and the data for a given current density. Few details of the optimization method are given, save that the Nelder-Mead algorithm is used. This algorithm uses the simplex method, where a polygon in N-dimensions with N+1 vertices is used to sample the design space for N parameters. The algorithm uses gradient data to update its search direction and find a minimum. The fitted values agree well with the data in previously published literature, but the 1D model is limiting and do not simulate effects under the current collector.

Carnes and Djilali [58] use a one-dimensional model to fit I-V curves independently with five parameters. They estimate membrane conductivity, oxygen mass transfer coefficients in the gas diffusion layer (GDL) and catalyst layer (CL), and cathode and anode exchange current densities. Directly estimating the membrane conductivity allows for model results to fit very closely with experimental data, as the effects of water movement, membrane hydration, and conductivity are decoupled. A tailored algorithm for nonlinear least-squares is used, solving the optimization with PDE constraints. This method is computationally efficient, as the model (described by a system of PDEs) is more closely linked to the optimization problem. The trade-off for this method is less versatility, as the optimization is no longer completely independent of the model. They obtain confidence intervals by estimating the parameters independently and proceed to fit curves by simultaneously estimating two and three of the five parameters. They conclude that simultaneous parameter estimation is more accurate as it captures the coupling between the parameters.

In the most detailed study, Guo et al. [59] present a one-dimensional cathode model to simultaneously fit curves at three different operating pressures. They use the Marquardt method for optimization, and note the difficulties with gradient-based methods for nonlinear systems of PDEs. Implementation of analytical sensitivities was considered for this study. These are gradient evaluations - obtained from the model by analytical differentiation - that are made available to the gradient estimator of the optimization algorithm. This method is efficient in that the extra function evaluations associated with finite differencing are avoided. Furthermore, the gradients are exact and never subject to the step-size dilemma of finite differencing. In the end, the choice for using numerical sensitivities was made, rather than attempting the complex implementation of analytical gradients. Their results compare the difference in parameter values when curves at different operating conditions are fit simultaneously, rather than individually. The conclusion is that the parameter values and confidence interval obtained by simultaneous fitting are more representative of the physical data and the range of uncertainty.

In all three of the aforementioned parameter estimation studies the one dimensional model is limiting, especially when evaluating mass transport coefficients. Carnes and Djilali note the natural progression of these methods to extend to two- and three-dimensions.

Jain et al. [60] extend this method to a two-dimensional along-the-channel MEA

model paired with the optimization program IPOPT. They estimate the water diffusion coefficient and cathode electrochemical properties by fitting the current density, but with cell voltage included as a fitting parameter for the polarization curve. Using the input as a fitting parameter is a modification to typical least-squares formulations which is called the errors-in-variables-measured (EVM) approach, in which it is assumed that there are errors in model output, errors in output from experimental measurement, and uncertainty in the input variables. This method should be used with caution as it effectively increases the number of design variables and improves the ability to fit the curve. However, if used properly it may reduce bias when the the input variables have measurable error.

Parameter estimation is a useful, and necessary step for determining the accuracy and range of predictability of a model. This task grows in complexity and computational requirements as the models become more and more detailed. In the only four examples in the literature for parameter estimation of PEMFCs, the reduced dimensions and model complexity are noted as being influential on the results.

1.4 Contributions

This work will expand the body of knowledge in the area of fuel cell modeling and analysis. The focus is on catalyst layer modeling and the characterization of its microstructure. The main contributions will be:

- The development of a new ionomer-filled agglomerate model.
- The development of a new water-filled agglomerate model that directly simulates the effect of an ionomer thin film.
- Integration of the agglomerate models as a unique multiscale simulation in the catalyst layer of a 2D MEA model.
- The development of a parameter estimation framework for the purpose of characterizing the CL structure and agglomerate parameters.

1.5 Thesis Outline

The objective of this work is to describe the catalyst layer microstructure in more detail with agglomerate models. This will be the topic of Chapter 2. In Chapter 3

these agglomerate models will be integrated into an existing numerical framework for modeling PEMFC developed by Secanell [54] in order to see the catalyst layer microstructure effects. Finally, the catalyst layer microstructure will be estimated using nonlinear least-squares parameter estimation in Chapter 4.

Chapter 2

Catalyst Layer Agglomerate Models

2.1 Introduction

While there are design obstacles to overcome in GDL and MPL design, the cathode catalyst layer is the biggest challenge in PEMFC design. Improving the conditions and mass transport in the cathode presents one of the largest opportunities for performance increase and cost reduction. Modeling can be a critical tool in understanding the complexities of the cathode and lead to more effective design of cell components and structure. The model, however, must be sufficiently complex to capture the physical processes.

The prevailing assumption for catalyst layer models is the presence of agglomerates. While this may not be a completely accurate physical representation, it is hypothesized that during fabrication the catalyst layer takes on a characteristic structure. In the catalyst ink preparation, the catalyst support nanoparticles aggregate in the presence of Nafion and a solvent. Figure 2.1 is a transmission electron microscope (TEM) image from Mukherjee et al. [61] of the interaction of the components on the nanometer scale. The image shows a small ionomer film around carbon particles supporting the platinum catalyst, supporting the agglomeration theory, however, the overall structure that results in the completed cell is largely unknown. In modeling, it is convenient and common to describe the agglomerates as spherical, and make simplifying assumptions about the inter-connectivity and structure of the overall catalyst layer. A schematic of the presumed structure used in this work is shown in Figure 2.2.

The catalyst layer has a full distribution of pore sizes from the nanometer scale

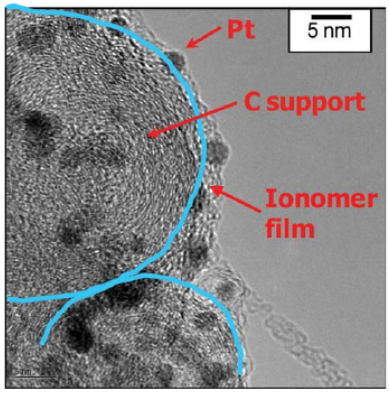

Figure 2.1: High Resolution TEM image of agglomerate structure in the catalyst layer from Mukherjee et al [61].

to the micron scale. The smallest pores, or the primary pores, exist within the agglomerate, while the secondary pores are larger, typically void, and allow for the transport of gaseous oxygen through the layer. The study by Thiele et al. [17], however, reveals that the majority of the pores are between 15-120nm in diameter. This means that at any modeling scale, agglomerate or catalyst layer, the diffusion process cannot ignore the effect of molecular contact with the pore walls. Their analysis shows that most of gaseous oxygen transport will be a 'transition zone' between slip flow and molecular flow, and none in continuous (bulk) flow. What still remains unclear is exactly how the structure and pores are physically arranged.

It is generally accepted that the long polymer chains of the ionomer bind the agglomerate together, wrapping around the outside of the particle to form a so-called thin-film. What is not agreed upon is the structure of the agglomerate core itself. Inside the agglomerates, it is not known whether pores are void or filled with ionomer. An assumption either way leads to the development of a vastly different model. Figure 2.3 shows a schematic of the two types agglomerate that will be investigated in this work. Figure 2.3(a) shows an agglomerate with the assumption that ionomer penetrates the pores, while Figure 2.3(b) assumes the pores to be free of ionomer and filled with water during cell operation.

Assuming an agglomerate structure in the catalyst layer leads to the inclusion of additional transport losses. These losses will affect the performance of both the anode and cathode, however, the cathode is of particular interest in PEM fuel cells as it is where most of the energy losses in the cell occur due to the sluggishness of

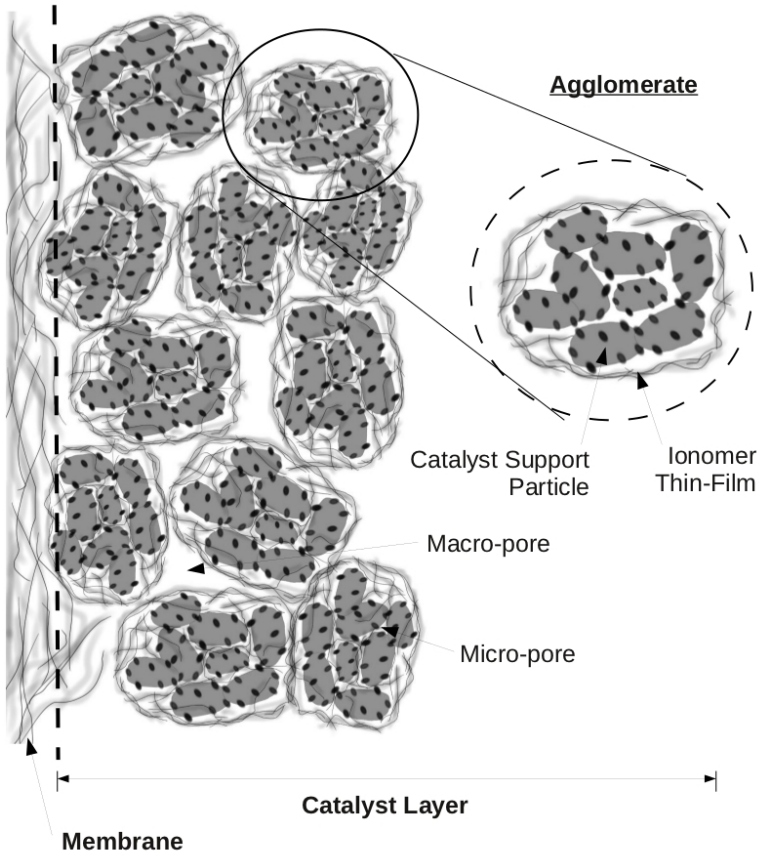

Figure 2.2: Schematic of the catalyst layer agglomerate structure.

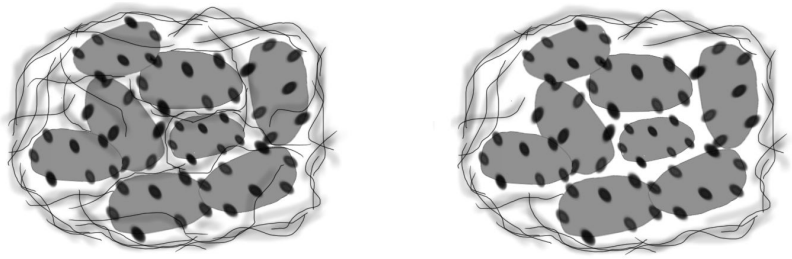

(a) Representation of the structure of a single, ionomer-filled agglomerate in the catalyst layer. The ionomer chains bind the agglomerate together in a thin film and penetrate the pores in the core

(b) Representation of the structure of a single, water-filled agglomerate in the catalyst layer. The ionomer chains only bind the agglomerate together by the thin film. The pores are free of ionomer and flood with water during operation

Figure 2.3: Schematic of the two types of agglomerates that are thought to exist within the catalyst layer.

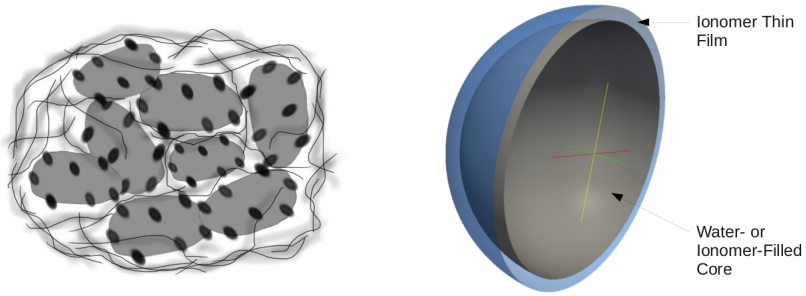

(a) Representation of the structure of a single, ionomer-filled agglomerate in the catalyst layer.

(b) 3D spherical domain on which the governing equations are applied.

Figure 2.4: Schematic of the ionomer-filled agglomerate and the assumed 3D domain used for modeling.

the ORR.

2.2 Ionomer-Filled Agglomerates

The reaction inside an agglomerate requires all three reactants, i.e. oxygen, protons, and electrons, to be readily available at the surface of the catalyst. For the reaction to occur throughout, there must be an effective transport mechanism for each species. The consequence of assuming that an agglomerate contains ionomer is that proton transport to the center of the agglomerate is not significantly restricted. Protons migrate from the membrane into the catalyst layer and agglomerates through the ionomer, aided by the sulphonic acid groups on the polymer backbone. The bulk movement of protons through both the membrane and the catalyst layers is governed by the electric potential in the electrolyte. At the agglomerate scale ($< 1\mu m$), this potential gradient is usually assumed to be constant. The case is similar for electron transport, as the solid network readily conducts electrons from the bi-polar plate through to the catalyst layer. Oxygen, therefore, becomes the limiting process in terms of species transport. Gaseous oxygen must diffuse from the pores in the catalyst layer into the ionomer thin film and towards the agglomerate core. Dissolved oxygen then diffuses through pores in the core which have been restricted by ionomer. As it contacts the pore walls, it reacts in the presence of a catalyst.

2.2.1 Governing Equations

The behavior of a general species in the agglomerate domain, shown in Figure 2.4, can be described starting from a simple mass balance.

$$\frac{\partial c_i}{\partial t} = -\vec{\nabla} \cdot \vec{N_i} + R_i \tag{2.1}$$

where c_i is the concentration of species i. This model will be solved at steady state; the left-hand side of the equation is zero. Of two remaining terms, R_i is the local source or sink for species i, which in this case is the electrochemical reaction. N_i represents the flux of species through the domain. If the species are considered infinitely dilute in the electrolyte and are free to move through the domain, fluxes can be described by the Nernst-Planck equation.

$$\vec{N_i} = -D_i^{eff} \left(\nabla c_i + \frac{z_i F}{RT} c_i \nabla \phi \right) + c_i \vec{v} \tag{2.2}$$

where D_i is the diffusion coefficient and z_i is the valency of the species. This model considers the transport of two species, oxygen and protons.

Protons - By ignoring convective transport, the average velocity of the solvent in the domain, $\vec{v}$ is zero. By assuming the ionomer chains are present across the domain, protons will be evenly distributed to maintain electroneutrality if conduction is sufficiently high. The gradient of proton concentration, ∇c_i, will be zero. Therefore proton flux can be obtained using

$$N_{H^+} = -\frac{z_i F}{RT} c_i \left(\vec{\nabla} \phi_m \right) \tag{2.3}$$

where ϕ_m is the only unknown and c_i will be equal to the concentration of negative ion groups in the ionomer.

Applying this to the mass balance equation in (2.1),

$$-\vec{\nabla} \cdot N_{H^+} = R_{H^+} = \frac{i}{n z_i F} \tag{2.4}$$

where $\frac{i}{n z_i F}$ relates the local volumetric current density (i) for a charged species to the reaction rate through the reaction stoichiometry and Faraday's constant. Noting that the conductivity can be defined as [3],

$$\sigma_m^{eff} = D_H \frac{(z_i F)^2}{RT} c_i \tag{2.5}$$

rearranging the coefficients in equation (2.4) results in the conductivity, therefore equation (2.1) for protons reduces to Ohm's law.

$$\vec{\nabla} \cdot \left[\sigma_m^{eff} \left(\vec{\nabla} \phi_m \right) \right] = i \tag{2.6}$$

Oxygen - Similar to protons, convective transport is ignored and the velocity term can be dropped from the equation. In the case of oxygen, the valency z_{O_2} is 0, and the flux equation simplifies to Fick's Law of diffusion.

$$\vec{N_{O_2}} = -D_{O_2}^{eff} \left(\nabla c_{O_2} \right) \tag{2.7}$$

The source term in equation (2.1) can be expressed as a function of the current given by the ORR, or

$$R_{ORR} = \frac{i}{nF} \tag{2.8}$$

where $n = 4$ for the oxygen mass balance equation, noting that the coefficients are negative to represent consumption of the species.

$$\vec{\nabla} \cdot D_{O_2}^{eff} \left(\vec{\nabla} c_{O_2} \right) = \frac{i}{4F} \tag{2.9}$$

If the potential in the solid phase, ϕ_s, is assumed to be constant, the processes can be defined by the system of two equations in (2.6) and (2.9)

Reaction Current Density - Defining an expression for the local volumetric current density, i, couples the two equations. Looking back to the Butler-Volmer equation, the resulting current density can be expressed by applying a few simplifying assumptions. Recall first from equation (1.6) in Chapter 1 that

$$i = i_0 \left[\left(\frac{c_{O_2}}{c_{O_2}^{ref}} \right)^{\gamma_{O_2}} \left(\frac{c_H}{c_H^{ref}} \right)^{\gamma_H} \exp\left(\frac{-\alpha_c F}{RT} \eta \right) - \exp\left(\frac{\alpha_a F}{RT} \eta \right) \right] \tag{2.10}$$

First, the concentration of protons is dropped from the equation, under the assumption that it will be constant under reference conditions. The reference exchange current density, i_0^{ref}, can then be defined as the exchange current of the cell under equilibrium conditions per unit area of catalyst. The active area of catalyst per unit volume in the domain (A_v) must then be included in the expression. Next, assuming that the cathode will always be operating at high negative overpotentials, it can be assumed that the reverse (anodic) reaction is negligible and can be

removed from the equation. Defining the cathode overpotential as positive value, $\eta_c = E^{eq} - (\phi_s - \phi_m)$, the current given by the reaction is

$$i = A_v i_0^{ref} \left[\left(\frac{c_{O_2}}{c_{O_2}^{ref}} \right)^{\gamma_{O_2}} \exp \left[\frac{\alpha_c F}{RT} \eta_c \right] \right] \tag{2.11}$$

Effective Transport Properties - Lastly, the diffusion coefficient for oxygen and the effective conductivity of the bulk electrolyte must be obtained from experimental values. In the thin film subdomain this nominal value is typically used, e.g. $D_{O_2,N}$ is represents bulk oxygen diffusion in Nafion. Within the agglomerate core diffusion will be impeded by the structure of the pores. The effective transport properties in porous media are commonly calculated by the Bruggeman relation [4]. The oxygen diffusion coefficient, for example, is

$$D_{O_2}^{eff} = D_{O_2,N}\, \epsilon_{agg}^{1.5} \tag{2.12}$$

2.2.1.1 Thin film Subdomain

It is important to note that the reaction only exists in the agglomerate core. In the thin film, the reaction will be zero and the problem reduces to simple transport with mass conservation. Thus, two distinct subdomains exist on which to solve the system of equations. Furthermore, the transport properties of both oxygen and protons change between the thin-film and agglomerate core subdomains, as transport is inhibited by the micropores, i.e. $D_{O_2}^{eff}$ and σ_m^{eff} are not constant over the domain.

2.2.1.2 Summary

In an ionomer-filled agglomerate, the system of equations must be described on two distinct subdomains with different transport and reaction coefficients. The full system of equations is given below.

$$\begin{aligned} &\text{Agglomerate Core:} && \begin{cases} \vec{\nabla} \cdot D_{O_2}^{eff} \left(\vec{\nabla} c_{O_2} \right) &= \frac{i}{4F} \\ \vec{\nabla} \cdot \sigma_m^{eff} \left(\vec{\nabla} \phi_m \right) &= i \end{cases} \\ &\text{Thin Film:} && \begin{cases} \vec{\nabla} \cdot D_{O_2,N} \left(\vec{\nabla} c_{O_2} \right) &= 0 \\ \vec{\nabla} \cdot \sigma_m \left(\vec{\nabla} \phi_m \right) &= 0 \end{cases} \end{aligned} \tag{2.13}$$

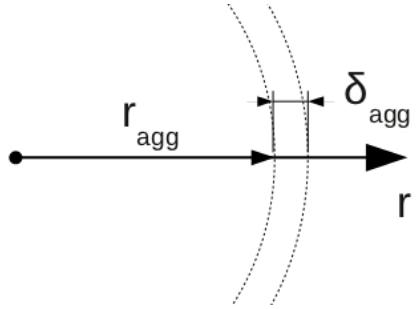

Figure 2.5: One-dimensional domain of a spherical agglomerate of radius r_{agg} and thin-film thickness of δ_{agg}

2.2.2 Solution Methods

The equations in (2.13) will results in a set of nonlinear partial differential equations. The solution can be obtained in a few different ways, some of which will be described in this section.

2.2.2.1 Boundary Value Problem Solvers

A numerical boundary value problem (BVP) solver can be used to solve a system of PDEs. The limitation is that most BVP solvers can only obtain a solution in one dimension. The equations must therefore be expressed in the appropriate coordinate system, with assumptions of symmetry in the un-modeled dimensions. In this case, it is assumed that the agglomerate is spherical. It is then necessary to assume that symmetry exists in the zenith and azimuthal directions. It is then convenient to describe the problem in spherical coordinates, which simplifies to the radial direction, r. The new computational domain is shown in Figure 2.5.

Equations - In order to guarantee conservation of flux over the domain, the condition is explicitly imposed; the problem is expressed as a system of 4 first-order equations, rather than 2 second-order. The four variables become the two fluxes and the concentrations. The overall equations become

$$\frac{1}{r^2}\frac{\partial}{\partial r}\left(r^2 N_{O_2}\right) = \frac{i}{4F} \tag{2.14}$$

$$\frac{1}{r^2}\frac{\partial}{\partial r}\left(r^2 N_{H^+}\right) = i \tag{2.15}$$

Expanding equation (2.14) will allow the gradient of the flux to be isolated. Note

that equation (2.15) is expanded similarly.

$$\frac{1}{r^2}\left(2rN_{O_2} + r^2\frac{\partial}{\partial r}N_{O_2}\right) = \frac{i}{4F} \tag{2.16}$$

$$\frac{\partial}{\partial r}N_{O_2} = \frac{i}{4F} - \frac{2}{r}N_{O_2} \tag{2.17}$$

The flux is defined as before (noting that the negative coefficient has already been moved to equation (2.14)).

$$N_{O_2} = D_{O_2}^{eff}\frac{\partial}{\partial r}c_{O_2} \tag{2.18}$$

$$\frac{\partial}{\partial r}c_{O_2} = \frac{N_{O_2}}{D_{O_2}^{eff}} \tag{2.19}$$

The equations are solved on a non-dimensional mesh from $\hat{r} = 0$ to $\hat{r} = 1$, where $\hat{r} = \dfrac{r}{(r_{agg} + \delta_{agg})}$. The change in variables is applied as follows.

$$N_{O_2} = \frac{1}{(r_{agg} + \delta_{agg})}D_{O_2}^{eff}\frac{\partial}{\partial \hat{r}}c_{O_2} \tag{2.20}$$

A new flux variable can then be defined as

$$\hat{N}_{O_2} = N_{O_2}\left(r_{agg} + \delta_{agg}\right) \tag{2.21}$$

so that

$$\hat{N}_{O_2} = D_{O_2}^{eff}\frac{\partial}{\partial \hat{r}}c_{O_2} \tag{2.22}$$

The transformation is first applied to equation (2.17), by substituting for r

$$\frac{1}{(r_{agg} + \delta_{agg})}\frac{\partial}{\partial \hat{r}}N_{O_2} = \frac{i}{4F} - \frac{1}{(r_{agg} + \delta_{agg})}\frac{2}{\hat{r}}N_{O_2} \tag{2.23}$$

and then for N_{O_2}

$$\frac{1}{(r_{agg} + \delta_{agg})^2}\frac{\partial}{\partial \hat{r}}\hat{N}_{O_2} = \frac{i}{4F} - \frac{1}{(r_{agg} + \delta_{agg})^2}\frac{2}{\hat{r}}\hat{N}_{O_2} \tag{2.24}$$

A similar approach is taken to obtain the non-dimensional equation for proton transport. The resulting set of equations on the non-dimensional domain is then

$$\begin{aligned}
&\text{Oxygen:} \quad \begin{cases} \dfrac{\partial}{\partial \hat{r}}c_{O_2} &= \dfrac{\hat{N}_{O_2}}{D_{O_2}^{eff}} \\ \dfrac{\partial}{\partial \hat{r}}\hat{N}_{O_2} &= \dfrac{i\left(r_{agg} + \delta_{agg}\right)^2}{4F} - \frac{2}{\hat{r}}\hat{N}_{O_2} \end{cases} \\
&\text{Protons:} \quad \begin{cases} \cdot\dfrac{\partial}{\partial \hat{r}}\phi_m &= \dfrac{\hat{N}_{H^+}}{\sigma_m^{eff}} \\ \dfrac{\partial}{\partial \hat{r}}\hat{N}_{H^+} &= i\left(r_{agg} + \delta_{agg}\right)^2 - \frac{2}{\hat{r}}\hat{N}_{H^+} \end{cases}
\end{aligned} \tag{2.25}$$

Boundary Conditions - Boundary conditions must be applied in order to obtain a solution. At the inner boundary symmetry must be maintained, and thus both variables will have a no flux condition.

$$\begin{aligned} N_{O_2}\left(r=0\right) &= 0 \\ N_{H^+}\left(r=0\right) &= 0 \end{aligned} \tag{2.26}$$

Values are prescribed at the outer boundary. For the electrolyte potential, a value corresponding to the local conditions in the catalyst layer can be set. The concentration of oxygen at the boundary must be carefully selected, as the reaction is directly dependent on this value. If the partial pressure of oxygen in the secondary pores of the catalyst layer is known, the concentration in the thin film can be determined. For a steady state solution, the dissolution of oxygen into the thin film will be at equilibrium. This process will be governed by Henry's Law, and the concentration at the inner surface of the thin film is given by

$$c_{O_2}^0 = \frac{p_{O_2}}{H_{O_2,N}} \left[\frac{Pa}{Pa \cdot cm^3/mol}\right] \tag{2.27}$$

where Henry's constant at equilibrium, $H_{O_2,N}$, is known from experimental testing. The boundary conditions at the surface of the thin film are then given by

$$\begin{aligned} c_{O_2}\left(r = r_{agg} + \delta_{agg}\right) &= c_{O_2}^0 \\ \phi_m\left(r = r_{agg} + \delta_{agg}\right) &= \phi_m^0 \end{aligned} \tag{2.28}$$

Performance Measures - The solution to these equations gives the concentration and electrolyte potential profiles through the domain. The most useful result, however, is the total current produced. The solution is used to obtain the current density distribution, which can be integrated over the sphere. Assuming symmetry in the radial and azimuth directions, the integral is obtained as follows

$$I_{agg} = \int_V i \, \mathrm{d}V = \int_0^{r_{agg}} 4\pi r^2 \, i(r) \, \mathrm{d}r \tag{2.29}$$

and in non-dimensional form as

$$\hat{I}_{agg} = \int_V i \, \mathrm{d}\hat{V} = \int_0^1 4\pi \hat{r}^2 \, i(\hat{r}) \, \mathrm{d}\hat{r} \tag{2.30}$$

On a numerical grid, the total current is obtained by Gaussian integration. Finally, the total current is averaged over the volume that agglomerate and thin film

occupy,

$$i_{agg} = \frac{I_{agg}}{4\pi \left(r_{agg} + \delta_{agg}\right)^3} \tag{2.31}$$

$$= \frac{\hat{I}_{agg}}{4\pi \left(1\right)^3} \tag{2.32}$$

Another measure of performance is the agglomerate effectiveness, E_{agg}. It is defined here as the average current given by the agglomerate as a fraction of the maximum, i.e. if the conditions at the boundary were maintained throughout the agglomerate core [35].

$$E_{agg} = \frac{i_{agg}}{i_{agg}^{max}} \tag{2.33}$$

The maximum current density is obtained by integrating equation (2.11) with $c_{O_2} = c_{O_2}^0$ and $\phi_m = \phi_m^0$ over the agglomerate domain (from 0 to r_{agg}). The integral over the domain and average current are again calculated using equations (2.29) and (2.31). This maximum current density represents the case where all of the available catalyst is used for the reaction. Thus, the effectiveness is an indication of the performance of an agglomerate inclusive of mass transport effects. Using this measure, the microscale transport losses can be accurately evaluated rather than qualitatively described when analyzing cell performance.

Solver - The system here is solved with a general purpose BVP solver named COLDAE developed by Ascher and Spiteri [62]. COLDAE has extended functionality beyond solving simple ODE's and can obtain a solution for mixed order systems of differential algebraic equations using a *selective projected collocation method*. The open source code written in FORTRAN is accessed through function wrappers in C++, which is the native language for all programs presented in this work. The solution and post-processing routines (e.g., integration for the average current and effectiveness) are calculated by accessing COLDAE's solution - a piecewise continuous polynomial function (up to order 7) defined on each sub interval on the mesh. Solutions here are defined on 100 sub-intervals with third-order polynomials.

2.2.2.2 Analytical Solution

It is possible, under certain conditions, to obtain an analytical solution to the agglomerate problem described above. Firstly, the solution must only be a function of the oxygen concentration. A solution with variation in the overpotential, temperature, or proton concentration has not been found in the literature. Secondly,

the reaction in the agglomerate must be first order with respect to this oxygen concentration. Lastly, the domain is only described in one dimension. The full domain was shown previously in Figure 2.5.

The following is a summary of the analysis; a full derivation of the solution is presented in Appendix A.1. This derivation is similar to Sun et al. [4] and Secanell et al. [33] and starts with an analysis of oxygen transport through the thin-film subdomain. The flux of oxygen (N_{O_2}) through the thin film surface must be equal to the total consumption of oxygen in the agglomerate, i.e. from 0 to r_{agg}

$$F_{O_2} = N_{O_2} \cdot 4\pi r^2 \tag{2.34}$$

Using Fick's Law for oxygen transport,

$$\frac{\mathrm{d}c_{O_2}}{\mathrm{d}r} = \frac{1}{4\pi r^2} \frac{F_{O_2}}{D_{O_2,N}} \tag{2.35}$$

The solution is given by integration over the thin film domain

$$\frac{c_{O_2,(g|l)} - c_{O_2,(l|s)}}{\delta_{agg}} = \frac{1}{r_{agg}\left(r_{agg} + \delta_{agg}\right)} \frac{F_{O_2}}{4\pi D_{O_2,N}} \tag{2.36}$$

where subscript (g/l) denotes the gas/liquid interface of the outer boundary, and the inner boundary is the liquid/solid interface (l/s). The concentration at the outer boundary is known explicitly through Henry's Law (see (2.27)). To obtain the value at the inner boundary, all that remains is to define the consumption of oxygen in the agglomerate.

The volumetric reaction rate with respect to oxygen in the agglomerate (R_{O_2}) can be obtained by using the solution for a reaction in a porous catalyst, as summarized by Bird, Stewart, and Lightfoot [63]. If an effectiveness factor (E_r, similar to section 2.2.2) is defined as the average reaction rate in the agglomerate as a fraction of the reaction at the surface, the total reaction rate can be defined as

$$R_{O_2} = E_r k_c c_{O_2,(l|s)} \tag{2.37}$$

where k_c is the reaction rate at the surface for an oxygen concentration of $c_{O_2,(l|s)}$.[1]

$$k_c = \frac{A_v i_0^{ref}}{4F\left(1-\varepsilon_V\right) c_{O_2}^{ref}} \exp\left[\frac{\alpha_c F}{RT}\left(E_0 - \left(\phi_s - \phi_m\right)\right)\right] \tag{2.38}$$

[1]The term $(1-\varepsilon_V)$ in equation (2.38) comes from the scaling of the active area. Typically, the active area for an electrode is given as the area per volume of catalyst layer. Since the agglomerate deals only with the solid and electrolyte phases, dividing by $(1-\varepsilon_V)$ gives the active area of Pt (cm^2_{Pt}) per volume of agglomerate (cm^3_{agg}). See also Appendix A.1

The equation for the effectiveness factor comes from the analytical solution the oxygen transport equation on the agglomerate domain [63].

$$E_r = \frac{1}{\phi_L}\left(\frac{1}{\tanh(3\phi_L)} - \frac{1}{3\phi_L}\right) \tag{2.39}$$

where ϕ_L is Thiele's modulus, which characterizes the reaction-transport process for a given geometry. For a sphere, the characteristic length is $\frac{r_{agg}}{3}$, so Thiele's modulus becomes

$$\phi_L = \frac{r_{agg}}{3}\sqrt{\frac{k_c}{D_{O_2}^{eff}}} \tag{2.40}$$

Equation (2.37) defines oxygen consumption on a volumetric basis. As the volume of the agglomerate is known, the total oxygen consumption within the agglomerate can be defined.

$$F_{O_2} = R_{O_2} V_{agg} = E_r k_c c_{O_2,(l|s)}\left(\frac{4\pi r_{agg}^3}{3}\right) \tag{2.41}$$

This is where the derivation differs from Sun et al. [4], who instead looked at the total consumption as a function of the flux through the outer surface of the thin film (See Appendix A.1 for details). Substituting equation (2.41) into equation (2.36), an expression for the concentration at the inner boundary can be obtained.

$$c_{O_2,(l|s)} = \frac{P_{O_2}}{H_{O_2,N}}\left[\frac{\delta_{agg} r_{agg}^2}{3\left(r_{agg}+\delta_{agg}\right)}\frac{E_r k_c}{D_{O_2,N}} + 1\right]^{-1} \tag{2.42}$$

The volumetric current density of the agglomerate can now be defined by the reaction rate and the stoichiometry of the ORR.

$$i_{agg} = 4F E_r k_c c_{O_2,(l|s)} \tag{2.43}$$

However, this gives a current density per unit volume of the agglomerate core. To obtain the average current produced over the full agglomerate volume the current must be scaled by the volume of the entire domain. Simply

$$\bar{V}_{agg} = \frac{V_{agg}}{V_{tot}} = \frac{\frac{4\pi r_{agg}^3}{3}}{\frac{4\pi(r_{agg}+\delta_{agg})^3}{3}} = \frac{r_{agg}^3}{\left(r_{agg}+\delta_{agg}\right)^3} \tag{2.44}$$

$$i_{agg} = 4F\bar{V}_{agg} E_r k_c c_{O_2,(l|s)} \tag{2.45}$$

Combining and rearranging the solution, the final expression for agglomerate current can be obtained.

$$i_{agg} = 4F\bar{V}_{agg}\frac{P_{O_2}}{H_{O_2,N}}\left[\frac{1}{E_r k_c} + \frac{\delta_{agg} r_{agg}^2}{3\left(r_{agg}+\delta_{agg}\right) D_{O_2,N}}\right]^{-1} \tag{2.46}$$

2.2.3 Model Validation

The 1D model shown in section 2.2.2.1 is validated against that presented in section 2.2.2.2. First, a comparison is made between the numerical model and the analytical solution for a spherical porous catalyst (with no thin film) [63]. The derivation gives an analytical solution for the oxygen concentration across all r based on the conditions at the boundary, R. The function is given as

$$\frac{c_{O_2}}{c_{O_2}(R)} = \frac{R \sinh\left(r\sqrt{k_c \Big/ D_{O_2}^{eff}}\right)}{r \sinh\left(R\sqrt{k_c \Big/ D_{O_2}^{eff}}\right)} \tag{2.47}$$

The solution presented in Figure 2.6 shows the relative oxygen concentration as a function of radial position for the two models. Two cases are presented, a medium current density case (Figure 2.6(a)) at an overpotential of $0.5\,V$ and a high current density case (Figure 2.6(b)) at $0.8\,V$ overpotential. Note that a low overpotential results in a flat oxygen profile. For reference, the agglomerate parameters are presented in Table 2.1 on page 42. The first case illustrates a typical solution profile and an agglomerate effectiveness of 81%, while the second is a more extreme case where the oxygen is completely consumed and does not penetrate deeper than 2% of the radius resulting in a 1.1% effectiveness factor. These results clearly show that the models match and it is concluded that the numerical model will match the analytical solution for any set of parameter values. These results also demonstrate the capability of the numerical solver, which easily handles a wide range of conditions, including oxygen depletion.

The analytical model with the thin film developed in section 2.2.2.2 can now be compared with the numerical model from section 2.2.2.1. The models are compared by their predictions of average current density over the domain. This integral quantity provides a more convenient measure for validation than a direct comparison of the concentration as it takes the solution over the whole domain into account. For the same set of parameters and boundary conditions, the difference in the current density given by either method is within 0.1%. A sample of this result is shown in Figure 2.7. The slight deviation can be explained by the inclusion of the electrolyte potential in the numerical solution and precision in the numerical integration over the mesh. The previous validation against published work and comparison between newly developed models gives high confidence in the accuracy and robustness of the

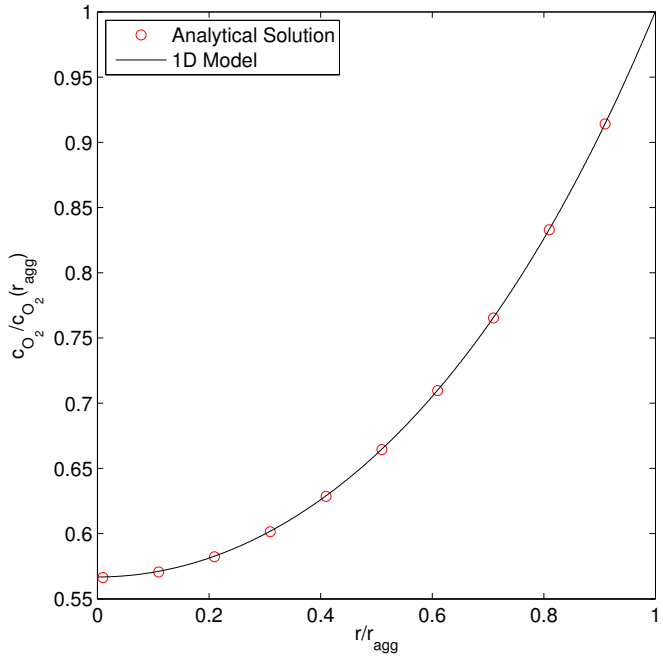

(a) Validation of the numerical model at $\eta_c = 0.5V$. Agglomerate effectiveness is 81%

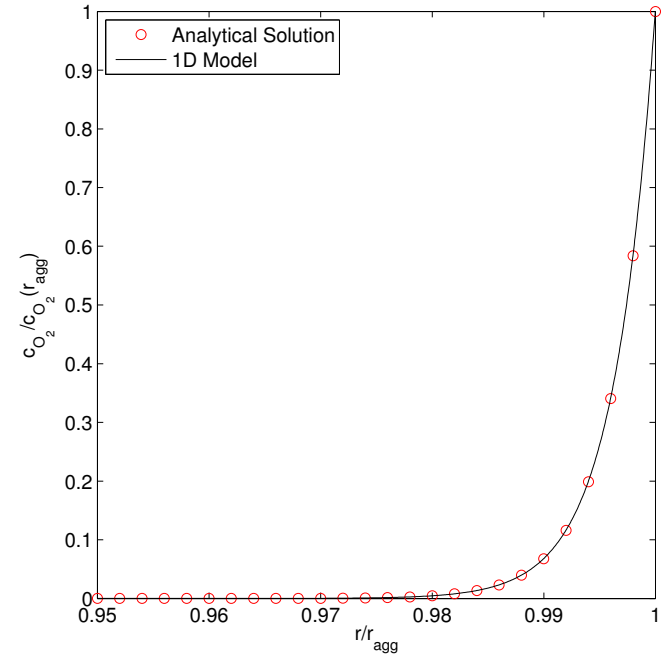

(b) Validation of the numerical model at $\eta_c = 0.8V$. Agglomerate effectiveness is 1.1%

Figure 2.6: Validation of the numerical model against the analytical solution for oxygen concentration given in equation (2.47) at medium and high overpotentials.

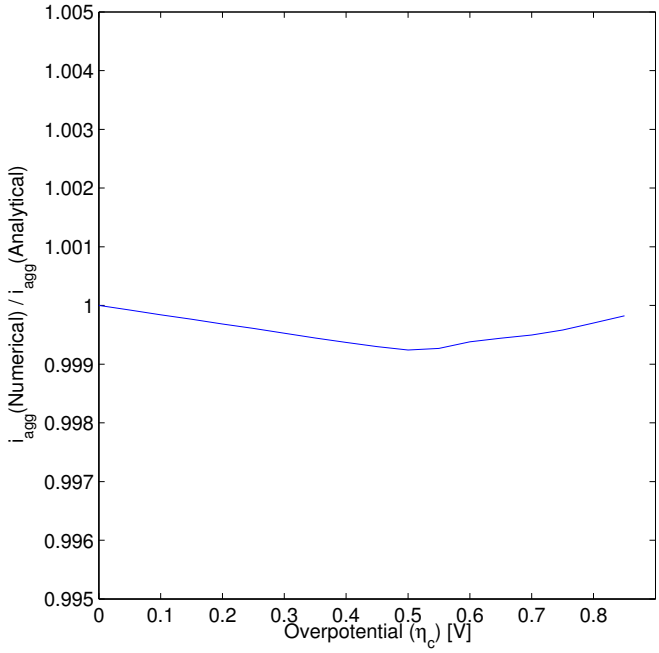

Figure 2.7: Comparison of the numerical and analytical agglomerate model current densities. Result were obtained for a range of overpotentials and a partial pressures at the thin film boundary. Shown here is a sample for a partial pressure of oxygen of 0.1 atm. Changes in the partial pressure yield identical results. Random variation in the agglomerate size and thin film from 50-300nm and 5-20nm respectively give the same trends, the difference between the solutions remaining within 0.1%.

solution.

The numerical method offers an advantage over the analytical solution. The expression for current density is not limited to a first order, single variable method. This means that any order of reaction can be simulated without approximation. Neyerlin et al. [64] for example, obtain a reaction order of around 0.5 from fitting curves to experimental data. Alternately, a vastly different kinetic model can be used. Dual path kinetic models, such as that suggested by Wang et al. [65] may offer a more accurate representation of ORR kinetics over the entire operating range of a PEM fuel cell. Substituting an expression for local current density using dual path kinetics will give a unique model of an agglomerate never presented in the literature. This will be a topic of future work.

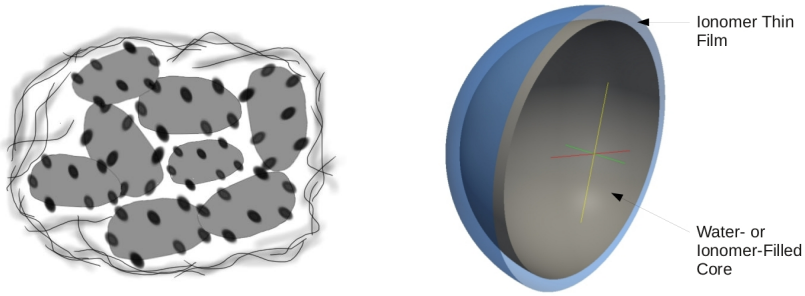

(a) Representation of the structure of a single, water-filled agglomerate in the catalyst layer.

(b) 3D spherical domain on which the governing equations are applied.

Figure 2.8: Schematic of the water-filled agglomerate and the assumed 3D domain used for modeling.

2.3 Water-Filled Agglomerates

The processes and solution described throughout section 2.2 was based around the principal assumption that the primary pores of the agglomerate are flooded with hydrated ionomer to facilitate proton transport. In this section, a similar model will be developed with the assumption that ionomer does not penetrate the micropores. This phenomenon was demonstrated by Malek et al. [66] who performed molecular dynamic simulations that revealed that there is a phase separation between the carbon and ionomer phases. The carbon particles will tend to group together, surrounded by ionomer. It is thought that the pores between the carbon particles fill with water. This conclusion can be drawn from two separate approaches.

During cell operation, water is assumed to be produced in liquid form. At steady state and sufficient current densities, this water will necessarily flood the pores of the agglomerate.

Alternately, it can be assumed that water is produced in vapour form. The cell is typically run at 80℃ but a temperature gradient may develop within the catalyst layer. Cells can also be designed to run closer to the boiling point where vapour is more likely to exist. However, an assumption that the pore walls are hydrophilic leads to a conclusion that vapour will condense and will flood the pores during cell operation due to a low saturation pressure. Using the Kelvin equation, the saturation pressure inside of a pore can be shown to be a function of its radius,

r_p.

$$p_r^{sat}(T) = p_\infty^{sat}(T) \exp\left(\frac{-2\sigma\cos(\theta)V_m}{RTr_p}\right) \tag{2.48}$$

In this equation, the saturation pressure for water on a flat surface, $p_\infty^{sat}(T)$, is transformed by an expression based on the surface tension (σ), molar volume (V_m), and contact angle (θ). The agglomerate pore walls are assumed to have a contact angle less than 90°, i.e. a hydrophilic surface, and pore diameters ranging from 15-40nm [17]. In this case, the exponential will tend to zero and drive the saturation pressure to a very small value. Therefore the assumption that water will always be a liquid in the agglomerate pores is in agreement with the representation of the physical phenomena occurring in the agglomerate. A schematic of a water-filled agglomerate is shown in Figure 2.8(a).

2.3.1 Governing Equations

A set of equations is presented here which describe the processes that are presumed to occur within a water-filled agglomerate. These equations and the resulting model are based on the work by Wang et al. [7], but are expanded by directly modeling the thin-film subdomain. The set of governing equations is developed, starting with a steady state mass balance for each species. These equations are applied to a spherical domain similar to the ionomer-filled model. A schematic and a representation of the domain are shown in Figure 2.8(a) and 2.8(b).

Oxygen - The equations describing the movement of oxygen within the domain are identical to an ionomer-filled with coefficients chosen appropriately for the new transport medium. To reiterate, the Nernst-Planck equation is used for the flux term in the mass balance of equation (2.49). This again simplifies to Fick's Law by eliminating the ion migration term and the convective transport term with the assumptions that there is no net flow in the pores.

$$\frac{\partial c_{O_2}}{\partial t} = -\vec{\nabla}\cdot\vec{N}_{O_2} + R_{O_2} \tag{2.49}$$

$$\vec{N}_{O_2} = -D_{O_2}^{eff}\left(\nabla c_{O_2}\right) \tag{2.50}$$

The source term is defined by the current density given by the ORR, adjusted for the reaction stoichiometry. The oxygen equation is again

$$\vec{\nabla}\cdot D_{O_2}^{eff}\left(\vec{\nabla}c_{O_2}\right) = \frac{i}{4F} \tag{2.51}$$

Protons - A mass balance for protons is included in the system of equations.

$$\frac{\partial c_H}{\partial t} = -\vec{\nabla} \cdot \vec{N_H} + R_H \tag{2.52}$$

The Nernst-Planck equation is again used to describe the flux. It can no longer be assumed that the transport of protons is governed by Ohm's law, as the conducting ion chains of Nafion are not present to allow protons to distribute evenly through the domain.

$$\vec{N_H} = -D_H^{eff} \left(\nabla c_H + \frac{z_H F}{RT} c_H \nabla \phi_m \right) + c_H \vec{v} \tag{2.53}$$

The zero velocity assumption applies to both species; the convective transport term is dropped. Ion migration can not be neglected for protons and thus the full expression for diffusion must include the transport effects in the presence of an electric field. Finally, defining the reaction similar to the equation for oxygen

$$R_H = \frac{i}{nF} \tag{2.54}$$

where $n = 1$ according to the reaction stoichiometry. The equation defining proton movement in the domain becomes

$$\vec{\nabla} \cdot \left[D_H^{eff} \left(\vec{\nabla} c_H + \frac{F}{RT} c_H \vec{\nabla} \phi_m \right) \right] = \frac{i}{F} \tag{2.55}$$

Equations (2.55) and (2.51) both use the Bruggeman relation to calculate the effective transport properties in the porous structure of the agglomerate [7], similar to the ionomer-filled model described in section 2.2.

The system of equations is not yet closed, as it cannot be assumed that the electrolyte potential remains constant through the domain. It follows that an extra equation is required to solve for the three variables in equations (2.51) and (2.55). For this, Poisson's equation can be used [67], which defines the potential according to the distribution of charges across the domain, given by $z_j c_j$.

$$\vec{\nabla}^2 \phi = \frac{-F}{\varepsilon \varepsilon_0} \sum_j z_j c_j + w \tag{2.56}$$

where w is a fixed charge density that depends on the properties of the domain. In the agglomerate subdomain, the fixed charge density is assumed to be zero. Substituting the appropriate variables and values defined in Table 2.1 into equation (2.56), the final equation required to close the system of equations becomes

$$\vec{\nabla}^2 \phi_m = \frac{-F}{\varepsilon \varepsilon_0} c_H \tag{2.57}$$

The equations are coupled by describing the local current density with Tafel reaction kinetics.

$$i = A_v i_0^{ref} \left[\left(\frac{c_{O_2}}{c_{O_2}^{ref}} \right)^{\gamma_{O_2}} \left(\frac{c_H}{c_H^{ref}} \right)^{\gamma_H} \exp\left(\frac{\alpha_c F}{RT} \eta_c \right) \right] \tag{2.58}$$

For the water-filled agglomerate, proton concentration varies throughout the domain. While the $\left(\frac{c_H}{c_H^{ref}} \right)^{\gamma_H}$ term was ignored in the ionomer-filled model due to constant concentrations, it plays a significant role on the local volumetric reaction rate in the water-filled model.

2.3.1.1 Thin film Subdomain

Similar to the ionomer-filled agglomerate, the problem must be redefined on the thin film subdomain. Firstly, there is no reaction within the thin film subdomain and thus the volumetric current density, i, will always be zero. Secondly, the bulk diffusion coefficients for protons and oxygen in Nafion are used to describe their movement. Equations (2.59) and (2.60) can now be used in the thin film to describe proton and oxygen transport, respectively.

$$\vec{\nabla} \cdot \left[D_{H,N} \left(\vec{\nabla} c_H + \frac{F}{RT} c_H \vec{\nabla} \phi_m \right) \right] = 0 \tag{2.59}$$

$$\vec{\nabla} \cdot \left[D_{O_2,N} \left(\vec{\nabla} c_{O_2} \right) \right] = 0 \tag{2.60}$$

The remaining equation changes to reflect the structure of the ionomer. It is assumed that each sulphonic group $\left(SO_3^- \right)$ on the polymer chains that comprise the ionomer will be balanced by a proton. This means that the bulk electrolyte can be considered electroneutral, i.e. there should be no local net charge in the ionomer. To translate this into the equations, this means that the fixed charge density in the thin film is equal to the concentration of sulphonic groups in the ionomer, $c_{SO_3^-}$. It is assumed that the ionomer also does not move or flow, so the charge density is constant. Poisson's equation can be re-written as:

$$\vec{\nabla}^2 \phi_m = \frac{-F}{\varepsilon \varepsilon_0} \left(c_H - c_{SO_3^-} \right) \tag{2.61}$$

The concentration of SO_3^- in the ionomer can be approximated with an estimate of the density of the dry membrane ($\rho_{m,dry}$) and the equivalent weight (EW), defined

as the mass of dry membrane per mole of SO_3^- [3] and is typically specified by the manufacturer.

$$c_{SO_3^-}\left[\frac{mol}{cm^3}\right] = \frac{\rho_{m,dry}}{EW}\left[\frac{g/cm^3}{g/mol}\right] \tag{2.62}$$

2.3.1.2 Summary

The water-filled agglomerate model described here requires a set of three nonlinear coupled partial differential equations, and is solved on two distinct subdomains. The full system of equations is presented in (2.63)

$$\begin{aligned}
&\text{Agglomerate Core:} \quad \begin{cases} \vec{\nabla}\cdot D_{O_2}^{eff}\left(\vec{\nabla}c_{O_2}\right) = \frac{i}{4F} \\ \vec{\nabla}\cdot\left[D_H^{eff}\left(\vec{\nabla}c_H + \frac{F}{RT}c_H\vec{\nabla}\phi_m\right)\right] = \frac{i}{F} \\ \vec{\nabla}^2\phi_m = \frac{-F}{\varepsilon\varepsilon_0}c_H \end{cases} \\
&\text{Thin Film:} \quad \begin{cases} \vec{\nabla}\cdot\left[D_{O_2,N}\left(\vec{\nabla}c_{O_2}\right)\right] = 0 \\ \vec{\nabla}\cdot\left[D_{H,N}\left(\vec{\nabla}c_H + \frac{F}{RT}c_H\vec{\nabla}\phi_m\right)\right] = 0 \\ \vec{\nabla}^2\phi_m = \frac{-F}{\varepsilon\varepsilon_0}\left(c_H - c_{SO_3^-}\right) \end{cases}
\end{aligned} \tag{2.63}$$

2.3.2 Solution Methods

The non-linearity of the system makes a numerical method the most appropriate way to obtain a solution. A BVP solver can be used for this purpose, with the appropriate definition of the problem in one dimension. Using a spherical agglomerate and assuming symmetry, the system of equations described in (2.63) becomes.

$$\begin{aligned}
&\tfrac{1}{r^2}\frac{\partial}{\partial r}\left(r^2 N_{O_2}\right) = \tfrac{i}{4F} \\
&N_{O_2} = D_{O_2}^{eff}\left(\frac{\partial}{\partial r}c_{O_2}\right) \\
&\tfrac{1}{r^2}\frac{\partial}{\partial r}\left(r^2 N_H\right) = \tfrac{i}{F} \\
&N_H = D_H^{eff}\left(\frac{\partial}{\partial r}c_H + \tfrac{F}{RT}c_H\frac{\partial}{\partial r}\phi_m\right) \\
&\tfrac{1}{r^2}\frac{\partial}{\partial r}\left(r^2\phi_m\right) = \tfrac{-F}{\varepsilon\varepsilon_0}\left(c_H - c_{fixed}\right)
\end{aligned} \tag{2.64}$$

where $c_{fixed} = 0$ in the agglomerate core and the effective diffusion coefficients, D_i^{eff}, are defined by the Bruggeman equation. The volumetric current density, i, is zero in the thin film. Note that similar to the ionomer-filled agglomerate, the transport equations have been defined as first order equations to ensure conservation of flux over the two domains.

Similar to the previous numerical model, the total current density in the agglomerate, is defined by equation (2.31) and the agglomerate effectiveness by equation (2.33). The equations are again non-dimensionalized to a unit domain for solving and plotting.

2.3.3 Model Validation

The characteristic solution given by this model is much different than the ionomer-filled model. The tendency is that proton transport becomes more limiting than oxygen [7]. This phenomenon is confirmed here in a validation of the model against that of Wang et al. [7], using their base case conditions and parameters, i.e. a 100nm agglomerate with no thin film, boundary conditions set at reference values, and an overpotential of $0.4\,V$. With the thin film removed, the model equations become identical. The results in Figure 2.9 show very good agreement. Comparing the proton concentration, Wang et al. [7] report a "proton penetration depth" of 13%. This value is defined as the radial distance into the agglomerate (from the surface to the core) where the proton concentration drops to 2% of the boundary value. Here, that value is found to be exactly 13.0% as well, as shown in Figure 2.9(b). A direct comparison of the electrolyte potential shows an increase towards the centre of the agglomerate of $0.176\,V$, which is similar to the published results of approximately $0.18\,V$. For equal comparison, the electrolyte potential is transposed to match the boundary value of the published data. In this simulation, the electrolyte potential at the boundary is set to zero, where the solid phase potential (ϕ_s) and the equilibrium potential (E_0) are set so that the overpotential (η_c) is $0.4\,V$. The reaction rate also compares directly, with a maximum value at the boundary of $1.75 \times 10^{-4}\ mol\ cm^{-3}s^{-1}$ and reducing to $0.35 \times 10^{-4}\ mol\ cm^{-3}s^{-1}$ at the centre. It can be concluded that the models are equivalent for an agglomerate with no thin film. There is no analytical model in the literature to compare. The inclusion of the thin film on the water-filled agglomerate is a novel contribution, unique to this work.

2.4 Results and Discussion

With both the ionomer-filled and water-filled models validated against cases with no thin film, it is now necessary to discuss how each reacts to the presence of a thin film. Comparing the two will give insight into their performance within a

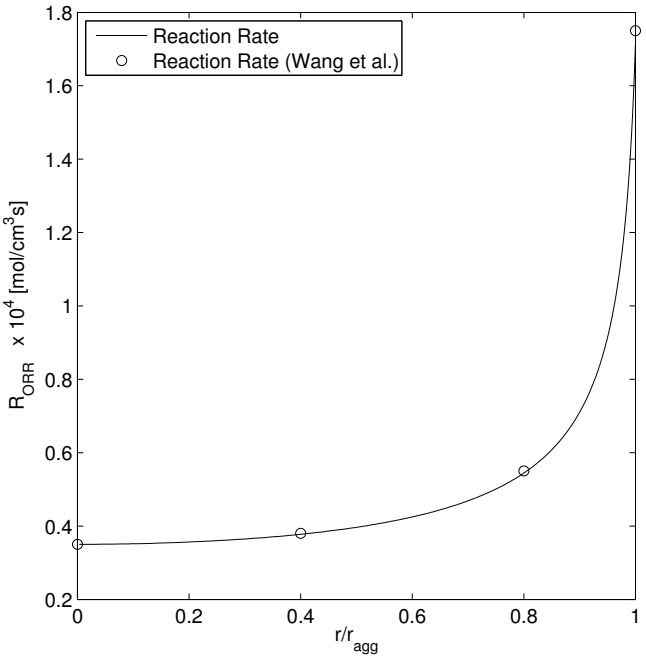

(a) Reaction rate profile within the agglomerate

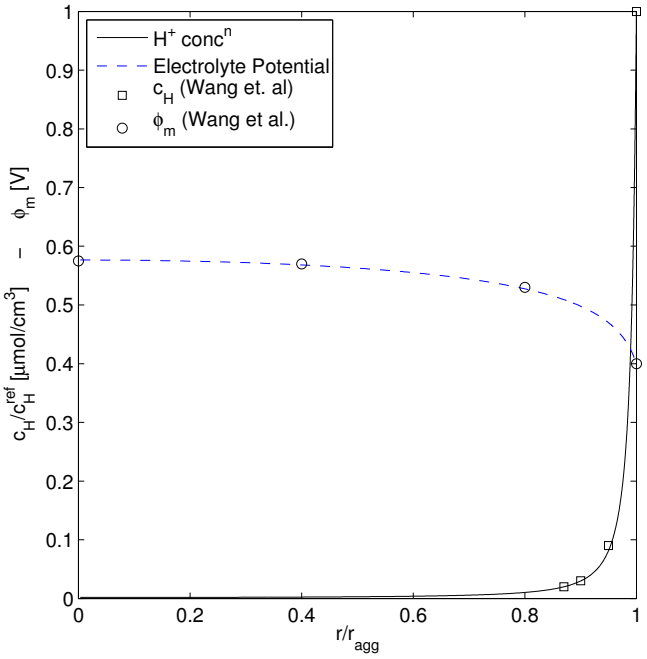

(b) Profiles of proton concentration and electrolyte potential within the agglomerate

Figure 2.9: Validation of the water-filled agglomerate model. Results compare the water-filled agglomerate models at the reference case conditions presented in reference [7]

catalyst layer model. In this section a comparison will be made directly between single agglomerates. Chapter 3 will investigate the effects of integrating agglomerate models into the catalyst layer.

2.4.1 Model Parameters

The performance of each of the models depends greatly on the choice of effective transport parameters and kinetic parameters used in the set of governing equations. Table 2.1 lists these parameters and the relevant physical constants. The kinetic parameters are consistent between the two models, and will be the starting point for the description.

The reference exchange current density is one of the most uncertain and sensitive parameters in the model. The value that is often used in PEM cathode models comes from the seminal works by Parthasarathy et al. [12, 13] investigating the pressure and temperature effects on electrode kinetics. However, a wide range of values used in models are obtained from various studies characterizing the ORR kinetics. Neyerlin et al. [64] provide a review of the range of kinetic parameters used in these studies, including the reference exchange current density at the cathode. The disparity between reported values stems from inconsistent definitions, but they provide a clear method to normalize the data to consistent reference conditions. Neyerlin also provides a clear explanation for setting the cathode transfer coefficient (α_c) to 1.0 over the range of operation, avoiding defining regimes where the Tafel slope doubles due to the kinetics. The model presented herein is built on the same belief that the changes in the Tafel slope observed at higher current densities are due to mass transport limitations rather than changes in electrode kinetics. Furthermore, changes in the kinetics are best determined a priori by models such as the aforementioned dual-path kinetic model by Wang et al [65]. In this manner, changes in slope are observed without having to apply changes to the model over transition zones determined empirically. Finally, the order of the reaction, γ, with respect to oxygen and proton concentration in these equations is set to one [4].

The transport parameters are obtained from published works investigating the bulk properties of water and Nafion. Specifically, the relative permittivity (or dielectric constant) of water is obtained from the work of Archer and Wang [68], who perform an in-depth study of the dielectric constant of water from Kirkwood equation and relate it to experimental results over a broad range of conditions. Most

importantly, the constant depends strongly on the temperature. The value used here accounts for the variation from STP in the simulation. Similarly, the relative permittivity of hydrated Nafion is obtained from the first of a series of works by Paddison et al [69] studying the dependence of water content on the permittivity. It is assumed here that the ionomer is fully hydrated and the permittivity can be approximated for a Nafion water content (λ) of 12 [70]. The oxygen diffusion coefficient in Nafion is one that takes a wide range of values in the literature, from a common value obtained from Parthasarathy [13], to the extremities in recent works published by Kudo et al. [71] and Peron et al. [70]. For this work, the values from Peron et al. [70] are examined over the range of operating conditions and a curve following an Arrhenius equation is fit to account for the changes in temperature.

$$D_{O_2,N} = D_0 \exp\left(\frac{E_d}{RT}\left(1 - \frac{T}{T_0}\right)\right) \tag{2.65}$$

For a reference temperature of 353K D_0 is $9.73 \times 10^{-6}\ cm^2/s$, while the activation energy of oxygen diffusion, E_d, was fit to a value of $39.76\ kJ/mol$.

The diffusion coefficient of protons through ionomer is not often discussed in such terms, but rather with respect to conductivity. It is known that the membrane properties are very sensitive to humidification levels and temperature. One of the founding models of PEMFC by Springer [72] describes a sorption isotherm for an extruded Nafion 117 membrane. This formula is updated with a new description of the sorption isotherm in equation (2.66), given by Mittelsteadt and Liu [73]

$$\lambda\left(a_w, T\right) = \left[1 + 0.2352a_w^2\left(\frac{T(^oC) - 30}{30}\right)\right]\left[14.22a_w^3 - 18.92a_w^2 + 13.41a_w\right] \tag{2.66}$$

where a_w is the water activity. The membrane proton conductivity can then be defined by membrane hydration but must be updated to reflect the change to recast ionomer membranes in catalyst layers and newer fuel cell designs. Data from BekkTech LLC [74] was used to obtain an expression for conductivity in Nafion NR-211®.

$$\sigma_m(\lambda, T) = \left(0.020634 + 0.01052\lambda - 1.0125 \times 10^{-4}\lambda^2\right)\left[\frac{E}{R}\left(\frac{1}{T_0} - \frac{1}{T}\right)\right] \tag{2.67}$$

Where $T_0 = 303K$ and conductivity is given in S/cm. Membrane modeling is discussed in more detail in Chapter3; figures of the sorption isotherm and membrane conductivity can be found on page 66.

Note that for the water-filled model, the proton diffusion coefficient in water-filled nanopores is obtained from Wang et al. [7]. The diffusion coefficient in the

Table 2.1: Electrochemical, transport, and global constants for the agglomerate simulations.

Description	Variable	Value	
Electrochemical constants			
Cathodic Transfer Coefficient	α_c	1.0	[64]
CL Active surface area of Pt	A_v	$2.00\,e5\ (cm^2/cm^3)$	[this work]
Ref. exchange current density	i_0^{ref}	$2.47\,e-8\ (A/cm^2)$	[64]
Ref. oxygen concentration	$c_{O_2}^{ref}$	$7.25\,e-6\ (mol/cm^3)$	[13]
Ref. proton concentration	c_H^{ref}	$1.818\,e-3\ (mol/cm^3)$	[this work]
Reaction order wrt. protons	γ_H	1.0	[7]
Reaction order wrt. oxygen	γ_{O_2}	1.0	[7]
Water transport constants			
Bulk Oxygen diffusion coef.	$D_{O_2,w}$	$9.19\,e-5\ (cm^2/s)$	[7]
Bulk proton diffusion coef.	$D_{H,w}$	$9.20\,e-5\ (cm^2/s)$	[7]
Relative permittivity of water	ε	60	[68]
Ionomer transport constants			
Bulk Oxygen diffusion coef.	$D_{O_2,N}$	$9.726\,e-6\ (cm^2/s)$	[70]
Bulk proton diffusion coef.	$D_{H,N}$	$9.20\,e-5\ (cm^2/s)$	[7]
Relative permittivity of ionomer	ε	20	[69]
Henry's constant	$H_{O_2,N}$	$3.1664\,e10\ (Pa\,cm^3\,mol^{-1})$	[4]
Global constants			
Universal constant	R	$8.314\ (J\,mol^{-1}K^{-1})$	
Faraday's constant	F	$96485\ (C/mol)$	
Permittivity of free space	ε_0	$8.854\,e-14\ (C^2\,J^{-1}cm^{-1})$	

thin film is assumed to of a similar order. Changes to this value will not significantly affect the results from the model as the boundary condition and electroneutrality condition dominate the behavior of protons in the thin film subdomain.

2.4.2 Agglomerate Performance

To compare the two types of agglomerates, five cases are chosen which represent current density regimes from very low to very high. From a cell perspective, the points would span the kinetic, ohmic, and mass transport regions of the polarization curve. At the thin film boundary, the oxygen concentration is set based on conditions that may be seen at a point in the catalyst layer using humidified air at atmospheric pressure. The electrolyte potential is set at a reference potential of $0.0\,V$, and the overpotential is defined as it was previously, $\eta_c = E^{eq} - (\phi_s - \phi_m)$. Recall that the solid phase potential is constant through the domain and E^{eq} is calculated by the Nernst equation. The operating conditions for the simulations are listed in Table 2.2. The cases are compared for an agglomerate with a 100nm radius and a 10nm thin film. All the results are presented on a grid normalized to r_{agg}. Therefore, the

Table 2.2: Operating conditions for three cases at which the agglomerate models will be compared

	Very Low I	Low I	Medium I	High I	Very High I
Case	(i)	(ii)	(iii)	(iv)	(v)
$x_{O_2}\,[-]$	0.15	0.125	0.100	0.075	0.05
$\eta_c\,[V]$	0.2	0.4	0.5	0.6	0.8

region of the plot for $1.0 < r/r_{agg} < 1.1$ represents the thin film subdomain. As such, reaction profiles are not plotted in this region due to the absence of catalyst.

Across all operating conditions, the most notable difference in the two models is the change in proton concentration and overpotential throughout the domain in the water-filled model. Recall that potential and proton concentration in the ionomer-filled model will be constant through the domain. These effects are well understood and explained by Wang et al. in their 2004 work [7]. Similarly here, Figure 2.10 shows that the proton concentration drops rapidly in the agglomerate core - three orders of magnitude in the first 15% of the radius and approximately 4 orders of magnitude at the center. Consequently, the local electrolyte potential increases to counter the imbalance of protons through the domain. The difference from the model by Wang et al. is the inclusion of the thin film. Figure 2.10 shows that there is not a sharp change at the agglomerate boundary like the ionomer-filled model, but rather a smooth transition from a conducting material to one where proton transport is limited. In the model, this transition takes place over a nanometer before the domain change. Physically, this domain change is not a single point, and the transition is likely a more gradual decrease in concentration. The consequence is that there is a notable change in the conditions at the interface from the reference conditions, leading to a lower maximum current density prediction. The discrepancy can be seen in Figure 2.11 where the reaction at the interface ($r/r_{agg} = 1$) is higher for the ionomer-filled model than the water-filled. At low current densities the difference is subtle. The overpotential increases at the boundary, counteracting the proton concentration drop and raising the reaction rate. The compensation is not sufficiently high at larger overpotentials.

For the water-filled models alone, the transition to higher overpotentials does not have a significant effect on the proton concentration and electrolyte potential profiles, as shown in Figure 2.10. The trend is that higher reaction rates cause marginal decreases in proton concentration at the center of the agglomerate and consequently

lower electrolyte potentials are observed. The anomaly in the simulations is the extreme case of high current density where all of the oxygen is consumed and no reaction occurs from $r = 0$ to $r = 0.89\, r_{agg}$. The behavior of protons in this case more closely resembles the low current density case. It can be said that generally, the reaction rate has little effect on the proton concentration profile.

The primary difference between the two model types is in the reaction profiles and the oxygen concentration profiles, shown in figures 2.11 and 2.12, respectively. At lower current densities of case (i) and (ii), the reaction profiles are nearly flat, and produce nearly the same total current density. Table 2.3 shows the total current density and the agglomerate effectiveness for each agglomerate at all five cases. The table and figures clearly show that the results start to diverge in cases (iii)-(iv). The oxygen profiles in Figure 2.12(b) show the limiting diffusion in the ionomer agglomerate due to the restricted pore size from the penetration of ionomer into the core. This effect, combined with a higher reaction rate at the boundary causes oxygen to be nearly depleted in case (iv) by $0.33 r_{agg}$, whereas in the water-filled model oxygen is still available to react through the entire domain. The drop in concentration over the water-filled agglomerate for the cases in Figure 2.12(a) is much less pronounced. This trend is reflected in the current density profiles of Figure 2.11, in the total current density, and the effectiveness factor. The higher oxygen concentration and overpotential in the water-filled agglomerate lead to a total current density more than double that of the ionomer-filled, which only performs at an effectiveness of 24%. This extra current comes from the inner 80% of the agglomerate core where the current drops less than an order of magnitude from its value at the interface, relative to the three orders of magnitude drop in local current density shown by the ionomer-filled agglomerate.

The model predictions start to converge in case (v) when oxygen becomes limiting for the water-filled agglomerate as well. Such a case is never examined by Wang et al. [7], who compare performances at much lower reaction rates. They claim that oxygen diffusion in water-filled pores is not the limiting step, and that the concentration will be quite uniform. In these extreme cases it is shown that both proton and oxygen transport play a role in the limiting current. The high reaction rate causes a large oxygen flux through the thin film, lowering the value at the boundary. Oxygen is then completely depleted (below $10^{-12}\ mol \cdot cm^{-3}$ in the simulation) in the first 11% of the water-filled agglomerate in case (v), compared to

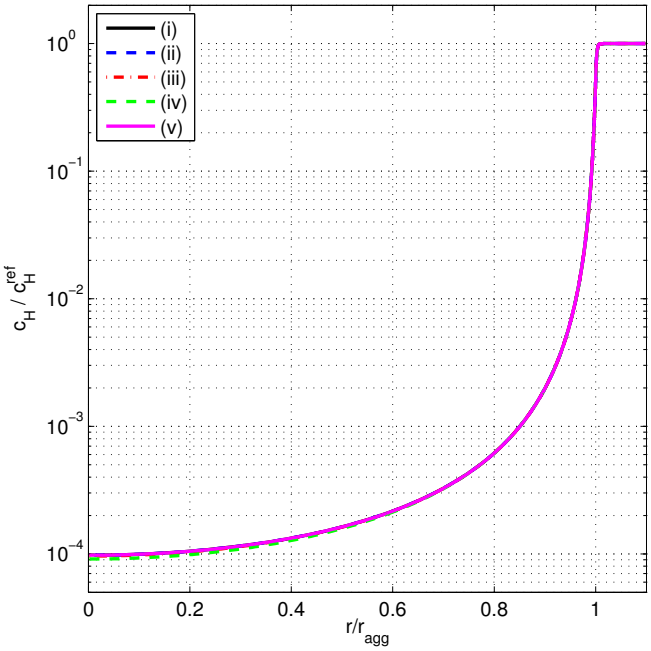

(a) Profile of proton concentration.

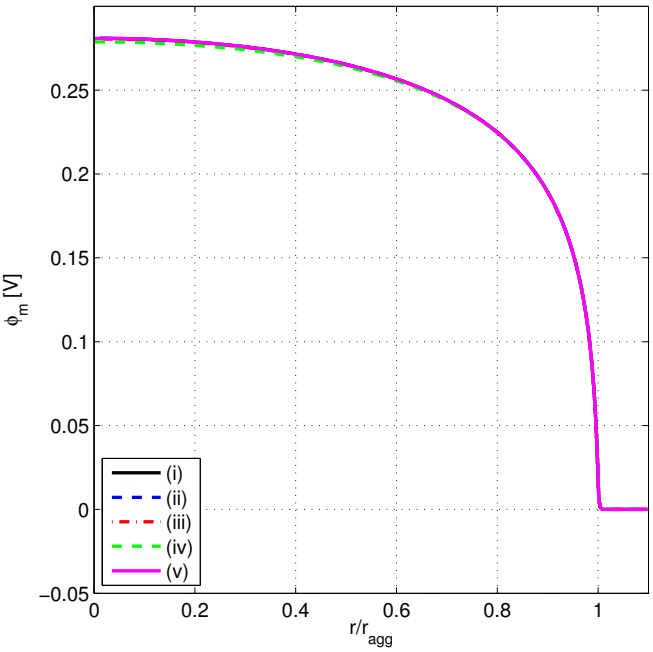

(b) Profile of electrolyte potential.

Figure 2.10: Profiles of proton concentration and electrolyte potential within the water-filled agglomerate for the five presented cases in Table 2.2.

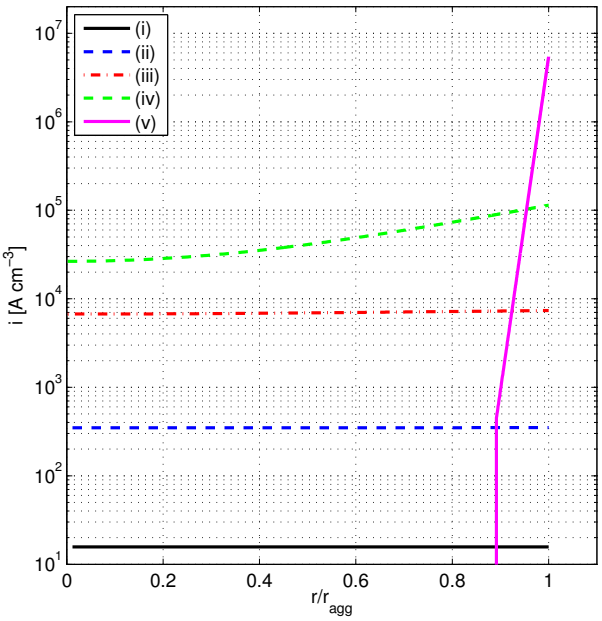

(a) Reaction profiles for the water-filled agglomerate.

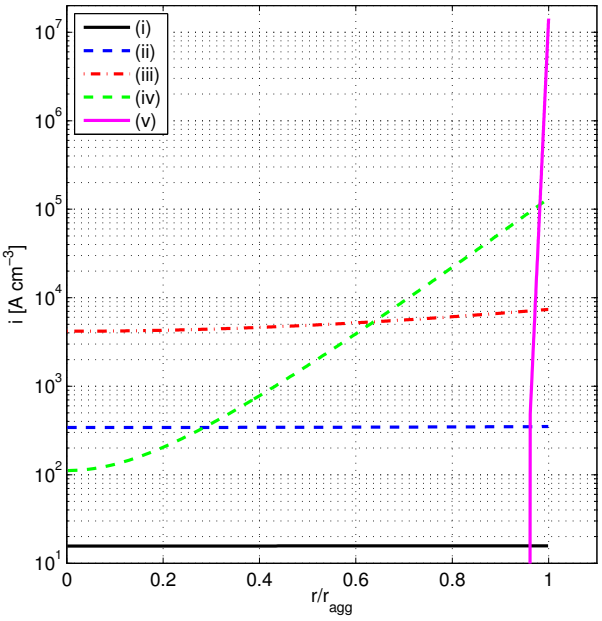

(b) Reaction profiles for the ionomer-filled agglomerate.

Figure 2.11: Reaction profiles within water-filled and ionomer-filled agglomerates for the five presented cases in Table 2.2.

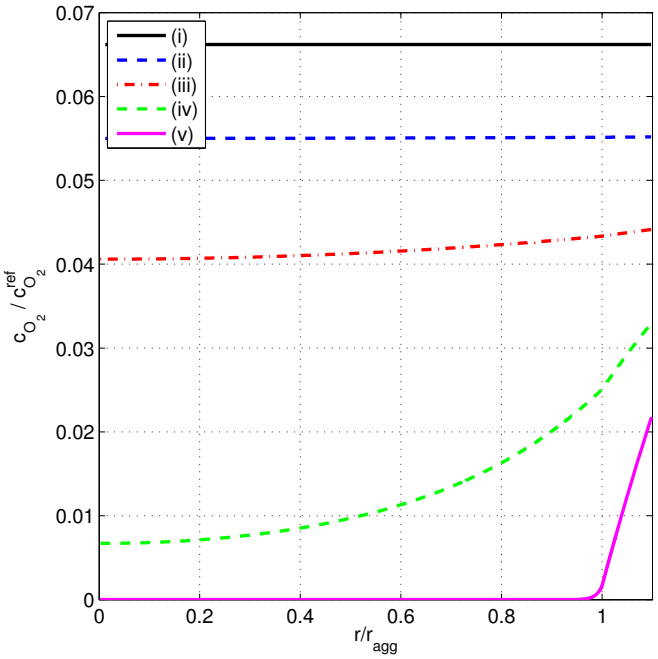

(a) Oxygen concentration profiles for the water-filled agglomerate.

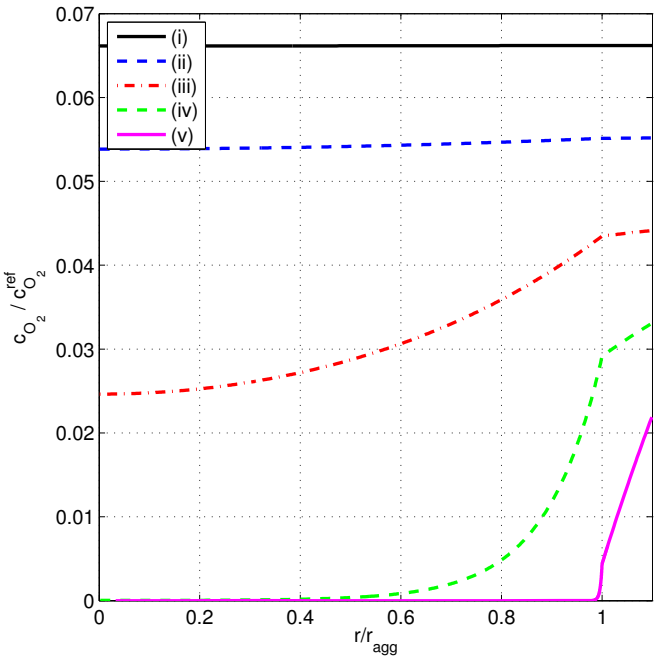

(b) Oxygen concentration profiles for the ionomer-filled agglomerate.

Figure 2.12: Oxygen concentration profiles within water-filled and ionomer-filled agglomerates for the five presented cases in Table 2.2.

Table 2.3: Results comparing the two types of agglomerate at the five reference cases.

Case	(i)	(ii)	(iii)	(iv)	(v)
Water-filled Agglomerate					
Current density (i_{agg}) [$A\,cm^{-3}$]	4.71	105	2147	21692	55066
Effectiveness factor (E_{agg}) [%]	100	99.8	95.3	47.9	0.25
Ionomer-filled Agglomerate					
Current density (i_{agg}) [$A\,cm^{-3}$]	4.71	104	1805	10676	47692
Effectiveness factor (E_{agg}) [%]	100	99.0	80.1	23.6	0.22

4% in ionomer-filled pores. These combined effects bring the total current given by both models much closer together.

2.4.2.1 Parameter Studies

Operating Conditions - The difference between the models is better demonstrated by looking at the current density response of both over the range of operating conditions. A parameter study was performed to obtain the agglomerate current from both models over oxygen partial fractions of 0.025 to 0.15, and for overpotentials of $0.0\,V$ to $0.9\,V$. It was found that while there are nonlinear changes in the current density across the parameter space, the models only differ across changes in overpotential. In other words, an increase in oxygen concentration at the thin film boundary causes equal percentage increases in either model at any given overpotential. To illustrate this phenomenon, the results are plotted in Figure 2.13 for a partial pressure of oxygen of 0.100. At low overpotentials the models are equal, as mass transport losses have little effect on the solution. A difference in the models only appears above overpotentials of $0.45\,V$. The water-filled agglomerate gives higher current densities than the ionomer-filled, and the difference peaks around $0.6\,V$. As discussed above, higher overpotentials drive the reaction to such a high rate that oxygen becomes limiting, and the models become equal as all of the oxygen reacts at the outer surface (at $\eta_c > 0.9\,V$).

Reaction Order - In section 2.2.3 it was noted that the numerical models allowed for different kinetics to be applied. Specifically, the results from Neyerlin et al. [64], were highlighted, where it was suggested that a reaction order (γ_{O2}) of 0.5 best characterizes their experimental data. The effects of applying this change are demonstrated in Figure 2.14 and 2.15. Figure 2.14 is an I-V plot comparing

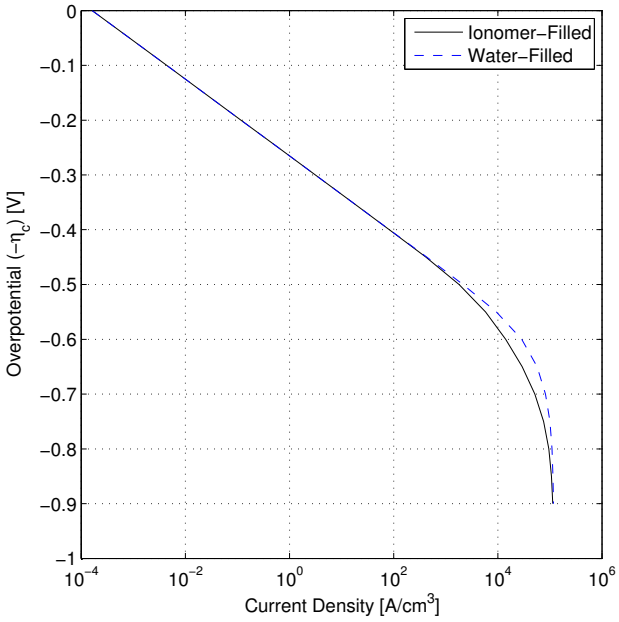

(a) Plot of cell overpotential vs. log of agglomerate current density for $x_{O_2} = 0.1$. Note that the cathode overpotential (η_c) is defined as positive, while the real cell overpotential is negative.

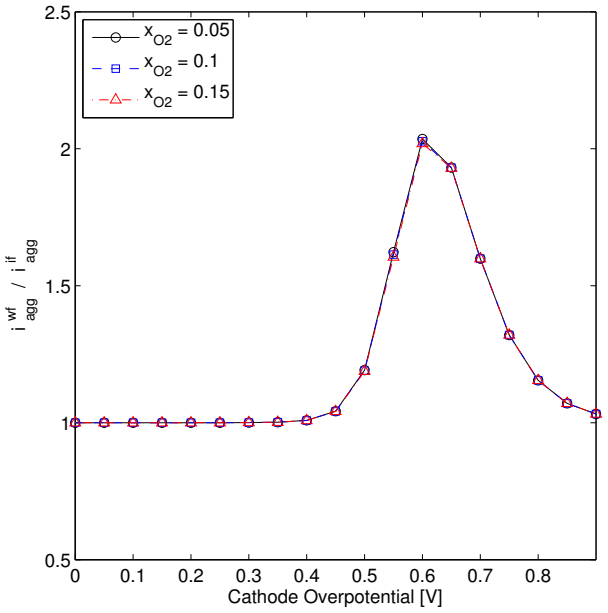

(b) Difference between the two models (Water-filled current density as a fraction of ionomer-filled). The difference shown here is nearly identical for any value of x_{O_2}

Figure 2.13: Comparison of the water-filled and ionomer-filled agglomerates.

first- and half-order reactions for a water-filled model at the same reference conditions as Figure 2.13(a). Points below overpotentials of $-0.55\,V$ are not shown, as the model does not achieve convergence. The case is similar for the ionomer-filled model, which gives identical results only to overpotentials of $-0.45\,V$. Convergence is not obtained due to the extremely high current densities. The current given by the half-order reaction under these conditions is approximately 4 times greater than the first order reaction. For some of the conditions tested the difference is nearly a full order of magnitude. Consequently, the agglomerate reaches oxygen depletion conditions and a limiting current at smaller overpotentials. A near limiting case for a water-filled agglomerate is shown in Figure 2.15. The reaction at the surface of the agglomerate is much higher, and remains high through the agglomerate core, but following a very nonlinear profile (see Figure 2.15(a)). This leads to higher rates of oxygen consumption through the core, nearly causing depletion at the center as shown in Figure 2.15(b).

For cases at even higher reaction rates, oxygen depletion occurs. This is generally troublesome for a numerical model. Concentrations are not allowed to be negative when modeling these physical phenomena . Iterative solvers, however, will typically test infeasible solutions. Some cases - such as the previously presented case (v) in Figure 2.12 - are able to be resolved around zero by the solver and a solution is obtained within the specified tolerance. Here, the problem is so nonlinear that COLDAE cannot obtain a solution that meets the constraint. Shampine et al. [75] give a detailed description of this type of problem and offer solution methods using common examples.

The lesson that can be learned from this work is that solutions can be obtained by applying special numerical treatment such as those described in [75], but a generalized solution for all problem types does not exist. Techniques to improve convergence were successfully used to obtain a solution, but not over the entire range of operating conditions. This topic, however, is outside of the scope of work and will not be described in detail.

Agglomerate Size - The size, composition, and thin film thickness of the agglomerate is not known explicitly from catalyst layer imaging. It is therefore useful to know the response of changing these parameters and how the models compare. Current density predictions were obtained for both agglomerates between sizes of

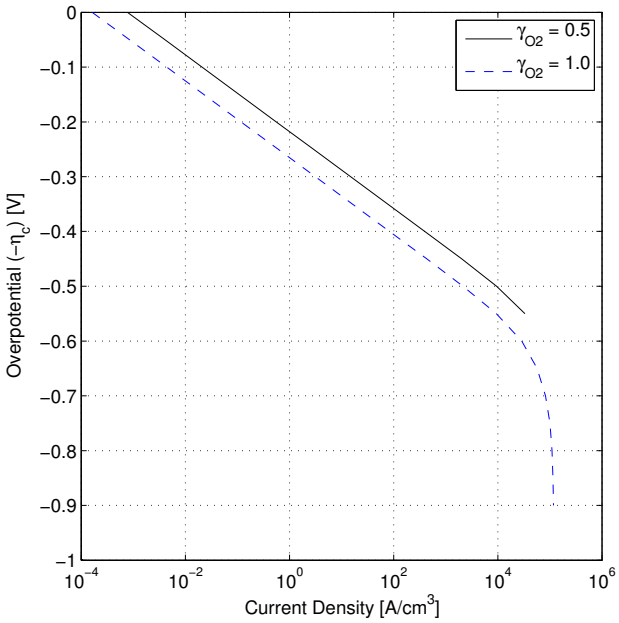

Figure 2.14: Comparison of the current density response for a water-filled agglomerates of differing oxygen reaction orders.

20nm and 300nm, and thin film thicknesses from 0 to 35nm. Operating conditions were fixed at an overpotential of 0.5 V and oxygen partial pressure of 0.100. An overpotential outside of the kinetic region was chosen to illustrate the difference in mass transport limitations. Points below 0.4 V will not effectively illustrate the difference between the models for reasons previously discussed.

The current density is nonlinear with respect to changes in radius and thin film thickness for both models, but it was found that the difference between the models is almost independent of the thin film thickness. A sample of the results for different radii with a thin film thickness of 10nm is presented in Figure 2.16. This figure illustrates two points. The first is that there is a radius that will maximize the average agglomerate current for any given thin film thickness. It may be expected that decreasing the agglomerate size will increase the average current density due to shorter diffusive paths, but it is not intuitive to suggest that a maximum is reached before the smallest size.[2] The second is that the difference in the models monotonically increases for growing agglomerate size, despite the shape of the curve. This means that for any given current density (outside the kinetic region), the estimated

[2]Since the current density is averaged by the volume of the entire agglomerate, a large ratio of thin-film to agglomerate radius decreases the volume fraction available for reaction.

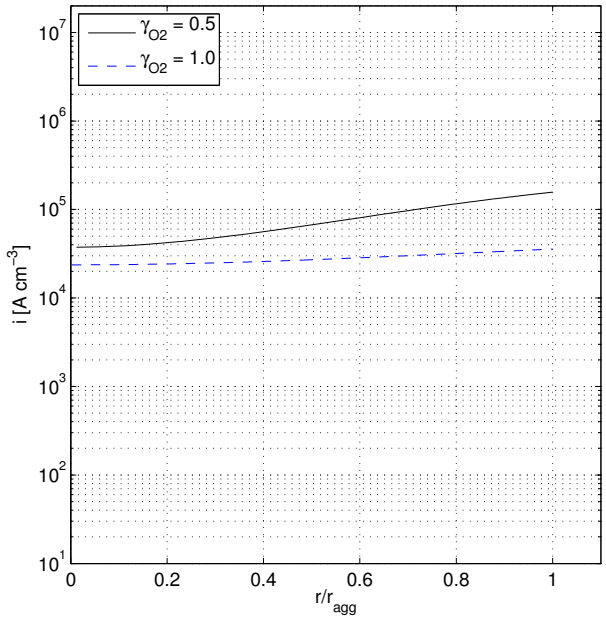

(a) Reaction profiles for water-filled agglomerates with different oxygen reaction orders.

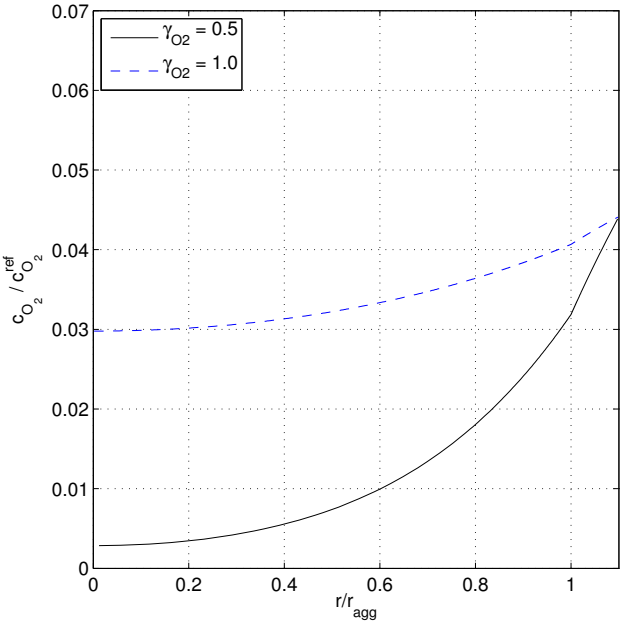

(b) Oxygen profiles for water-filled agglomerates with different oxygen reaction orders.

Figure 2.15: Comparison of water-filled agglomerates with differing reaction orders. Operating conditions of $x_{O_2} = 0.100$ and $\eta_c = 0.55\,V$.

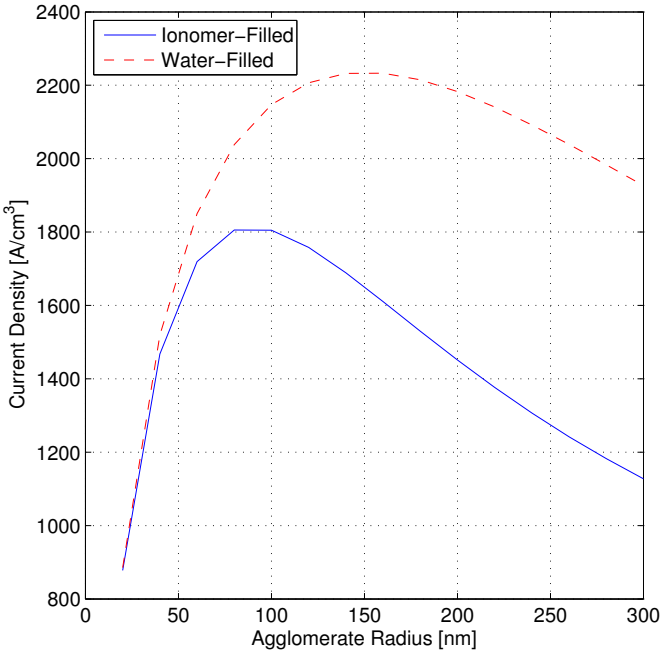

Figure 2.16: Response by the two models to changes in agglomerate size for a thin film thickness of 10nm.

size of the agglomerates will always be smaller if the assumption is made that the pores are water-filled. This has particular implications on the results presented in chapters 3 and 4.

Chapter 3

PEM Fuel Cell Modeling

3.1 Introduction

A number of approaches can be taken for modeling PEM fuel cells. Two common ones are empirical based (or reduced dimension) modeling and full physical modeling of the cell. The former is typically used to model stack and system processes, or component characteristics that can be compared to measured experimental data. Detailed physical modeling is used for a different purpose altogether. These types of models are typically used to analyze processes in a cell that cannot be observed or easily measured experimentally. The models must therefore be capable of predicting the measurable behavior of a cell while simulating the hidden physical phenomena occurring within. Models in the literature are now typically single cells in two- or three-dimensions, and can also be transient but generally at a smaller time scale - seconds, rather than minutes, hours, or days. The focus of this chapter is on the development of a 2D model of an MEA simulating the physics across the gas channels. Figure 3.1 demonstrates the reduction of a 3D cell model to the 2D computational domain. As the figure shows, the effects of gas flow under the current collector will be directly modeled. This is in contrast to an along the channel model, where changes in oxygen concentration and current densities may occur as the gasses flow from the inlet to the outlet of the cell. In the model presented here, gas is assumed to be provided in excess stoichiometries, and no significant depletion of reactants occur throughout the cell. The focus can then be placed on the effects of the diffusion through porous media, and on the reaction in the catalyst layer. Recall that the anode and cathode reactions are given by

$$2H_{2(g)} \rightarrow 4H^{+}_{(aq)} + 4e^{-} \tag{3.1}$$

(a) Section of a single cell showing two bipolar plates with gas channels around a membrane electrode assembly

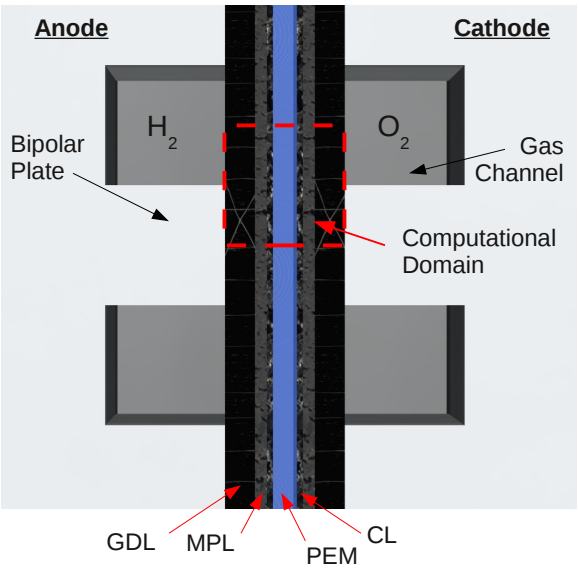

(b) Closeup on the section of the cell. The anode and cathode gas channels feed reactants to an MEA constructed with a GDL, MPL and CL on a thin membrane.

Figure 3.1: Three dimensional representation of a single cell used for the simulation. 3.1(b) shows the reduction of the problem from 3D to a 2D across-the-channel model for the computational domain

$$O_{2(g)} + 4H^{+}_{(aq)} + 4e^{-} \rightleftharpoons 2H_2O_{(l)} \tag{3.2}$$

The cathode catalyst layer reaction was the focus of Chapter 2. Therein, methods were presented to obtain a prediction of the current density given local operating conditions in the catalyst layer. Section 3.2.3 will discuss how each of these methods is integrated into the MEA model. This includes the integration of 1D agglomerate models solved with a BVP solver. This type of multiscale model is unique to this work; a similar case has not been found in the literature.

3.2 Membrane Electrode Assembly Model

This model is an extension of the work by Secanell [54], who describes the 2D MEA model solved using the finite element method (FEM). The model and assumptions are similar, and will be summarized here.

The MEA of a typical PEMFC will contain five transported species that are of interest: Hydrogen, Oxygen, Water, Protons, and Electrons. Equations must be developed to describe the movement of each of these species. First, the overlying

assumptions for the transport of each species must be outlined.

1. The cathode is fed with humidified air, i.e. a mixture of oxygen, water vapour, nitrogen.
2. The anode is fed with pure humidified hydrogen, i.e. a mixture of only hydrogen and water vapour.
3. The reacting gases contain no impurities.
4. All species behave as ideal gases.
5. The effects of convection in the MEA are negligible.
6. The membrane is impermeable to gases and electrons.
7. The cathode and anode remain at constant pressure.
8. Oxygen and water vapour are considered dilute species in Nitrogen in the cathode.
9. Water vapour is considered a dilute species in Hydrogen in the anode.
10. The transport of gases is modeled using Fick's Law of diffusion.
11. Proton transport only occurs in the electrolyte (ionomer membrane) phase.
12. Anion groups in the ionomer are in sufficient concentration to allow for the free movement of protons; transport is governed by Ohm's law.
13. Electron transport only occurs in the solid phase.
14. Electrons are free to flow through the solid phase; transport is governed by Ohm's law.

The assumption of no convection (5) is justified for two reasons. The model domain is at a small scale and through porous media, thus the dominant form of transport will be from the chemical potential (i.e. the concentration gradient). Small changes in pressure will not cause a significant change in the flux of a species through the domain. Secondly, from a modeling perspective, the domain is two dimensional and across the channel. Since the membrane is impermeable to gases (assumption 6), there is only one inlet/outlet at the cathode for humidified air and similarly at

the anode for humidified hydrogen. Modeling convection in such a domain leads to an equalization in pressure. From this perspective, assumption 7 comes as a direct result of 5 and 6.

Assumptions 1 and 7 lead to simplifications when developing the set of governing equations for the cathode. At constant pressure, the total concentration of the gas mixture will remain unchanged. The equations can then be developed using the molar fractions, rather than concentrations of gases. This allows for a reduction in the number of modeling equations, as Nitrogen is not of interest and simply represents the remaining fraction of gas mixture. A similar argument can be made at the anode. However, in this case of interest is the transport of water vapour. Although the molar fraction of hydrogen will determine the rate of the reaction, it can be easily determined based on the presence of water vapour.

Water is of interest as it is the only species that is present throughout the entire domain. Furthermore, it exists within two phases. Since the gas streams are humidified, vapour will exist wherever there is a presence of gas in the void space of the porous media. Water will also be present in liquid form in the cell. In this model, condensation of water in the pores is neglected. Models that account for this phenomenon are called *two-phase flow models* [15], and are a very active area of research [76]. Water will exist, however, in the ionomer membrane and the membrane phase of the catalyst layer. Water is absorbed in the membrane from the vapour in the pores and is transported in the membrane phase by chemical potential, and by electro-osmotic drag. Water vapour and liquid water in the membrane will therefore have to both be directly modeled and coupled by absorption/desorption rates in the anode and cathode catalyst layers.

Assumption 10 that gas transport is governed by Fick's law may be the broadest assumption made in this section. Fick's law applies for binary mixtures and infinitely dilute solutions, which applies well at the anode for humidified hydrogen [3]. Equation (3.3) is of a familiar form presented in Chapter 2.

$$\vec{N_i} = -D_{ij} \left(\nabla c_i\right) \tag{3.3}$$

The binary diffusion coefficients (D_{ij}) can be calculated using molecular theory of gases and thus the fluxes (N_i) for each species can be determined from the gradient of the concentration (c_i). It should be noted that the total flux in any direction should be zero. For multicomponent mixtures however, the gas diffusion is typically

more complicated. In this case, the Maxwell-Stefan equations should be used to determine the concentration profiles of each species.

$$\nabla x_i = RT \sum_{j \neq i} \frac{x_i N_j - x_j N_i}{p D_{ij}} \tag{3.4}$$

This equation gives the gradient of the mole fraction of species i (x_i) accounting for the effects of all other components j. Binary diffusion coefficients are used to relate the fluxes between each of the species. The cathode is best described by a multicomponent mixture of this type, but using these equations introduces a great deal of non-linearity into the system of equations (the concentrations and coefficients must be determined by the simulation). For a binary mixture, or for components that are sufficiently dilute in a solvent, Fick's equation can be derived from equation 3.4 if there is no convective flux.

The above assumptions about transport relate only to bulk species movement. The domain to be modeled is predominantly porous media. To help develop the modeling equations that will result, there must be further assumptions about the composition of the layers in the domain.

15. The GDL is modeled as a random anisotropic network of carbon fibers and pore space.

16. The MPL is modeled as a random isotropic mixture of solid conductive material (carbon) and pore space.

17. The CL is modeled as a random isotropic mixture of ionomer, solid conductive material (carbon) and pore space.

18. The electrochemical reaction takes place only inside of an agglomerate (whose structure is described in Chapter 2) which is comprised of the solid and ionomer phases in the CL.

19. The membrane is modeled as an isotropic electrolyte material.

These assumptions, coupled with the transport assumptions will allow the governing equations and constitutive equations to be defined based on the local subdomain in the simulation. Finally, some general modeling assumptions are made to simplify the system of equations.

20. The domain remains at constant temperature.

21. The model is solved at steady state.

By using assumption 20, two phenomena are implied. Firstly, the system controlling the flow of gases is able to accurately regulate the temperature of the incoming streams so that there will be no local fluctuation in temperature, nor any over the modeling time. Secondly, the heat generated by the reaction in the catalyst layer is not sufficient to significantly increase the temperature of the surrounding media and gases. This residual heat is conducted away through the cell cooling system. Finally, the last assumption is that the cell will develop an equilibrium over time and operate under steady state conditions.

3.2.1 Governing Equations

As described in the previous section, the movement of all the species through the domain must be described. A mass balance for each species is applied; the system is coupled through the source terms.

$$\begin{aligned}
\nabla \cdot (c_{tot} D_{O_2}^{eff} \nabla x_{O_2}) &= R_{O_2} \\
\nabla \cdot (c_{tot} D_{w}^{eff} \nabla x_{w}) &= R_{w} + S_{\lambda} \\
\nabla \cdot (\sigma_{m}^{eff} \nabla \phi_{m}) &= R_{H^+} \\
\nabla \cdot (\sigma_{s}^{eff} \nabla \phi_{s}) &= R_{e^-} \\
\nabla \cdot \left(n_d \tfrac{\sigma_m}{F} \nabla \phi_m + \tfrac{\rho_{m,dry}}{EW} D_{\lambda} \nabla \lambda \right) &= -S_{\lambda}
\end{aligned} \tag{3.5}$$

Each of the equations will be described in more detail over this section. In short, x_i represents the mole fraction (partial pressure) of gas i. The electric potentials are represented by ϕ. Finally, the membrane water content is described by λ. The reaction terms are given by R_i and water sorption into the membrane by S_λ.

The system of equations was reduced for the anode, i.e. the hydrogen equation was dropped. The movement of water through hydrogen fully describes the behavior of both species since the sum of the two molar fractions is 1. Similarly in the cathode, water vapour and oxygen diffuse in nitrogen and thus it is not required to model its movement. The first two equations therefore describe the movement of gaseous oxygen and water vapour through the domain. The next two equations describe the changes in potential in the electrolyte phase and solid phase by Ohm's law, which is derived from the transport of protons and electrons. The final equation describes

Table 3.1: List of subdomain names and abbreviations

Subdomain	Abbreviation
Anode Gas Diffusion Layer	AGDL
Anode Microporous Layer	AMPL
Anode Catalyst Layer	ACL
Membrane	PEM
Cathode Catalyst Layer	CCL
Cathode Microporous Layer	CMPL
Cathode Gas Diffusion Layer	CGDL

the movement of water through the membrane with a parameter λ, representing its water content. The details of this equation will be described later in the section on page 63. These governing equations are applied to each of the subdomains, where subdomain-specific effective parameters are applied. The subdomain names and abbreviations are tabulated in 3.1 and shown on the computational grid in Figure 3.2.

3.2.1.1 Boundary Conditions

Conditions must be imposed at the boundaries in order to obtain a solution to the set of partial differential equations. There are 6 boundaries in the domain shown in Figure 3.2

- Anode current collector at $(x, y) = \{x = 0, y = [0, \frac{W_{cc}}{2}]\}$.
- Anode gas channel at $(x, y) = \{x = 0, y = [\frac{W_{cc}}{2}, \frac{W_{cc}}{2} + \frac{W_{ch}}{2}]\}$.
- 2 Symmetric boundaries at $(x, y) = \{\forall x, y = 0 \text{ and } \frac{W_{cc}}{2} + \frac{W_{ch}}{2}\}$.
- Cathode current collector at $(x, y) = \{x = L_{MEA}, y = [0, \frac{W_{cc}}{2}]\}$.
- Cathode gas channel at $(x, y) = \{x = L_{MEA}, y = [\frac{W_{cc}}{2}, \frac{W_{cc}}{2} + \frac{W_{ch}}{2}]\}$.

where $L_{MEA} = L_a^{gdl} + L_a^{mpl} + L_a^{cl} + L^m + L_c^{cl} + L_c^{mpl} + L_c^{gdl}$, and L_a^{gdl}, L_a^{mpl}, L_a^{cl}, L^m, L_c^{cl}, L_a^{mpl}, L_c^{gdl} represent the anode GDL, MPL, and CL, membrane and cathode CL, MPL, and GDL thicknesses respectively. W_{cc} and W_{ch} represent the current collector and channel width. The conditions for each of the variables at the boundaries are listed below. Note that $\vec{n}$ is the normal to the boundary surface.

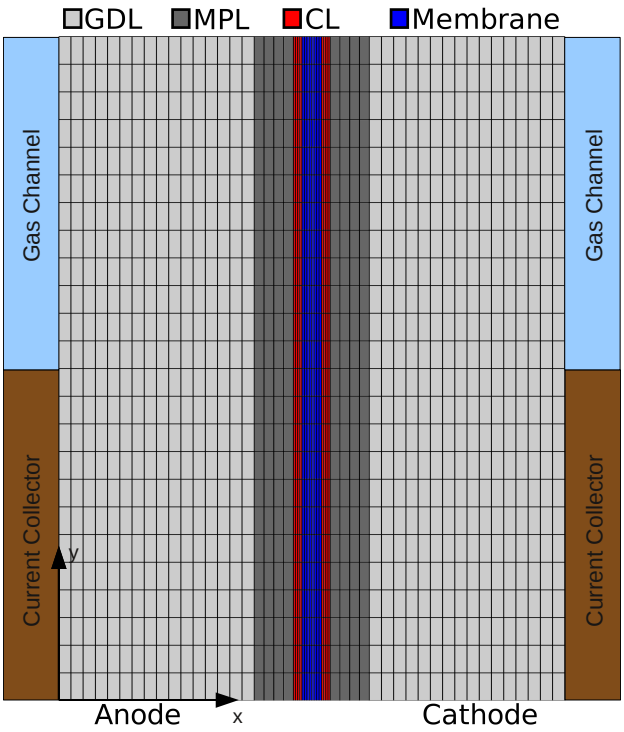

Figure 3.2: Grid representation of the computational domain used for modeling the MEA

Anode Current Collector:

$$N_{O_2} = \vec{n} \cdot (c_{tot} \vec{D^{eff}_{O_2}} \nabla x_{O_2}) = 0$$
$$N_w = \vec{n} \cdot (c_{tot} \vec{D^{eff}_{w}} \nabla x_w) = 0$$
$$\phi_s = 0$$
$$N_{H^+} = \vec{n} \cdot (\vec{\sigma_m} \nabla \phi_m) = 0$$
$$N_\lambda = \vec{n} \cdot \left(n_d \frac{\sigma_m}{F} \nabla \phi_m + \frac{\rho_{m,dry}}{EW} D_\lambda \nabla \lambda \right) = 0$$

Anode Gas Channel:

$$N_{O_2} = \vec{n} \cdot (c_{tot} \vec{D^{eff}_{O_2}} \nabla x_{O_2}) = 0$$
$$x_w = x^0_{w,a}$$
$$N_{e^-} = \vec{n} \cdot (\vec{\sigma_S} \nabla \phi_s) = 0$$
$$N_{H^+} = \vec{n} \cdot (\vec{\sigma_m} \nabla \phi_m) = 0$$
$$N_\lambda = \vec{n} \cdot \left(n_d \frac{\sigma_m}{F} \nabla \phi_m + \frac{\rho_{m,dry}}{EW} D_\lambda \nabla \lambda \right) = 0$$

Cathode Current Collector:

$$N_{O_2} = \vec{n} \cdot (c_{tot} \vec{D_{O_2}^{eff}} \nabla x_{O_2}) = 0$$
$$N_w = \vec{n} \cdot (c_{tot} \vec{D_w^{eff}} \nabla x_w) = 0$$
$$\phi_S = V_{cell}$$
$$N_{H^+} = \vec{n} \cdot (\vec{\sigma_m} \nabla \phi_m) = 0$$
$$N_\lambda = \vec{n} \cdot \left(n_d \frac{\sigma_m}{F} \nabla \phi_m + \frac{\rho_{m,dry}}{EW} D_\lambda \nabla \lambda \right) = 0$$

Cathode Gas Channel:

$$x_{O_2} = x_{O_2}^0$$
$$x_w = x_{w,c}^0$$
$$N_{e^-} = \vec{n} \cdot (\vec{\sigma_S} \nabla \phi_S) = 0$$
$$N_{H^+} = \vec{n} \cdot (\vec{\sigma_m} \nabla \phi_m) = 0$$
$$N_\lambda = \vec{n} \cdot \left(n_d \frac{\sigma_m}{F} \nabla \phi_m + \frac{\rho_{m,dry}}{EW} D_\lambda \nabla \lambda \right) = 0$$

At the symmetric boundaries, the fluxes for all components are zero. The no flux conditions for protons and membrane water content at the boundaries listed above should be applied for a generalized solution method. It should be noted that for the solution method used in this work, those boundary conditions effectively shift to the CL boundary. It is explained in section 3.2.2 that these equations are not solved outside of the domains where they exist, e.g. the membrane and catalyst layers. The same applies for the oxygen boundary conditions in the anode and hydrogen in the cathode. An alternate method is to solve all of equations in all domains, and set transport properties to *nearly* zero. This method, however, may introduce some numerical instability and is not computationally efficient.

3.2.1.2 Constitutive Equations

Many of the terms and coefficients in the generalized system of equations presented in (3.5) are defined by expressions describing alternate physical processes within the cell. These constitutive equations define the behavior of the solution variables over the domain.

Reactions - One of the largest contributors are the source terms, which fully couple the system of equations. The reaction source terms (R_i) describe either the

consumption or production of the species in the subdomain and are related to the current density and the reaction stoichiometry. The sorption source term (S_λ) links the two phases of water by giving the absorption rate. These terms are typically not defined on all domains. For example, the reaction terms will exist only in the catalyst layer, defined by the local current density. For the first four equations, the source terms are

$$R_{O_2} = \begin{cases} \frac{i_{CL}}{4F} & \text{in the CCL} \\ 0 & \text{all others} \end{cases} \tag{3.6}$$

$$R_w = \begin{cases} -\frac{i_{CL}}{2F} & \text{in the CCL} \\ 0 & \text{all others} \end{cases} \tag{3.7}$$

$$R_{H^+} = \begin{cases} i_{CL} & \text{in the CCL} \\ -i_{CL} & \text{in the ACL} \\ 0 & \text{all others} \end{cases} \tag{3.8}$$

and

$$R_{e^-} = \begin{cases} -i_{CL} & \text{in the CCL} \\ i_{CL} & \text{in the ACL} \\ 0 & \text{all others} \end{cases} \tag{3.9}$$

where i_{CL} is the local volumetric current density in the catalyst layer given, for example, by the Butler-Volmer equation (2.11) or by an agglomerate model (2.46) discussed in Chapter 2. Using the same expression in all equations couples the behavior of each of the species. Applying the reaction stoichiometry from equations (3.1) and (3.2) ensures conservation of mass applies within the computational domain.

Membrane Modeling - The final equation in system (3.5) gives the water movement through the domain by a parameter λ, defined as the amount of water absorbed in the membrane. The concentration of sulphonic groups is used as the reference, so that lambda represents the number of water molecules per acid group; i.e.

$$\lambda = \frac{c_{H_2O}}{c_{SO_3^-}} \left[\frac{\text{mol}_{H_2O}}{\text{mol}_{SO_3^-}} \right] \tag{3.10}$$

where the concentration of SO_3^- in the ionomer can be approximated as in Chapter 2 by equation (2.62). Reiterating,

$$c_{SO_3^-} \left[\frac{mol}{cm^3} \right] = \frac{\rho_{m,dry}}{EW} \left[\frac{g/cm^3}{g/mol} \right] \tag{3.11}$$

The transport of this water is then defined by the flux, which can be broken up into three terms. The first is convective flux, which is ignored in this case, assuming

the anode and cathode will be at the same pressure. Once this is neglected, the model takes on the same form as that presented by Springer et al. [72]. The model accounts for two transport processes: diffusive flux and electro-osmotic drag. Diffusion takes on a similar form as for water in the gas phase,

$$\vec{N}_{w,diffusion} = -D_{H_2O}\nabla c_{H_2O} \tag{3.12}$$

however, the coefficients must be redefined. Using equation (3.10) and (3.11), the concentration of water can be substituted for λ.

$$c_{H_2O} = \lambda c_{SO_3^-} = \frac{\rho_{m,dry}}{EW}\lambda \tag{3.13}$$

and

$$\vec{N}_{w,diffusion} = -\frac{\rho_{m,dry}}{EW}D_\lambda \nabla\lambda \tag{3.14}$$

if the diffusion coefficient for water in the membrane is defined as D_λ.

Water also moves by electro-osmotic drag. This is a process where proton flux causes water movement due to dragging from the polarity of the water molecule. The number of water molecules dragged per proton can be determined experimentally, and can potentially range from zero to much greater than 1. Springer et al. [72] use a linear relationship between the drag coefficient and water content, with a fully hydrated membrane with $\lambda = 22$ carrying 2.5 molecules of water. This reduces at lower hydration levels, so the drag coefficient (n_d) becomes a linear relation of water content.

$$n_d = 2.5\frac{\lambda}{22} \tag{3.15}$$

The protonic flux has already been defined by Ohm's law,

$$\vec{N}_{H^+} = \frac{\vec{i}}{F} \tag{3.16}$$

and

$$-\sigma_m^{eff}\left(\nabla\phi_m\right) = \vec{i} \tag{3.17}$$

The flux of water can then be defined as

$$\vec{N}_{w,drag} = n_d\vec{N}_{H^+} \tag{3.18}$$

and finally,

$$\vec{N}_{w,drag} = -n_d\frac{\sigma_m}{F}\nabla\phi_m \tag{3.19}$$

This flux term is nonlinear in the coefficient, as the proton conductivity, σ_m, is also dependent on the water content. The conductivity is determined empirically, and is a function of membrane hydration and temperature [73].

$$\sigma_m(\lambda, T) = \left(0.020634 + 0.01052\lambda - 1.0125 \times 10^{-4}\lambda^2\right) \left[\frac{E}{R}\left(\frac{1}{T_0} - \frac{1}{T}\right)\right] \tag{3.20}$$

Where $T_0 = 303K$ and conductivity is given in S/cm. The coefficients of the equation were determined by fitting experimental data from BekkTech LLC [74] for the specific ionomer NR-211® from DuPont. The membrane conductivity is related to its water content through the relative humidity of the surroundings. This relationship is given by the sorption isotherm, discussed below.

In the anode and cathode catalyst layers, water is transported through the membrane, but is also in balance with the vapour phase. The sorption isotherm determines the equilibrium condition of liquid water inside the membrane in an atmosphere of vapour. This isotherm is dependent on the temperature of the membrane, but also the activity of the surrounding water vapour [73].

$$\lambda_{eq}\left(a_w, T\right) = \left[1 + 0.2352a_w^2\left(\frac{T(^oC) - 30}{30}\right)\right]\left[14.22a_w^3 - 18.92a_w^2 + 13.41a_w\right] \tag{3.21}$$

where,

$$a_w = \frac{p_{H_2O}}{p_{sat}(T)} = RH \tag{3.22}$$

The sorption isotherm and the resulting membrane conductivity are shown in Figure 3.3. These properties are nonlinear and cause a large variation in effective properties over the domain. Furthermore, the sorption isotherm has a direct effect on the local absorption/desorption of water vapour in the catalyst layers.

Local water sorption will then occur from a concentration imbalance of water at the gas/liquid interface. The rate of absorption/desorption is determined by a rate constant, k_λ and the concentration is again determined from λ by equation (3.13).

$$S_\lambda = \begin{cases} k_\lambda \frac{\rho_{m,dry}}{EW}(\lambda_{eq} - \lambda) & \text{ACL, CCL} \\ 0 & \text{all others} \end{cases} \tag{3.23}$$

where, similar to Secanell [54], k_λ is set to 10,000 to ensure that the water produced in the CL does, in fact, hydrate the membrane. This represents a very fast absorption/desorption time between water in the vapour phase and membrane phase.

The mass balance for water in this phase combines the two flux terms defined above with the source term to yield the fifth equation in the system (3.5):

$$\nabla\left(n_d\frac{\sigma_m}{F}\nabla\phi_m + \frac{\rho_{m,dry}}{EW}D_\lambda\nabla\lambda\right) = -S_\lambda$$

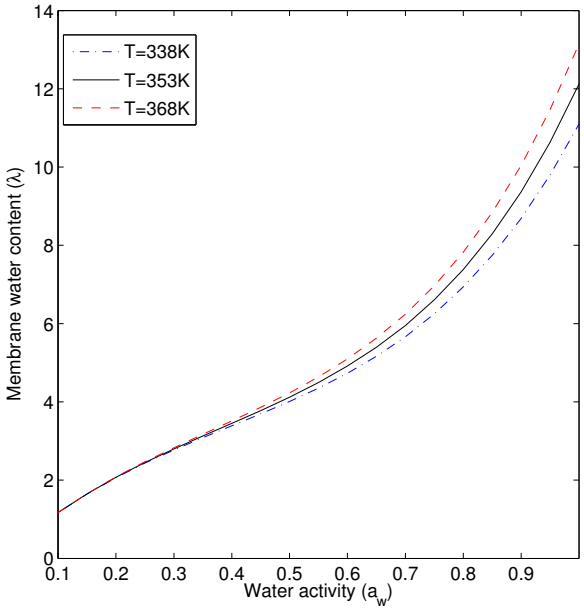

(a) Sorption isotherm at varying temperatures.

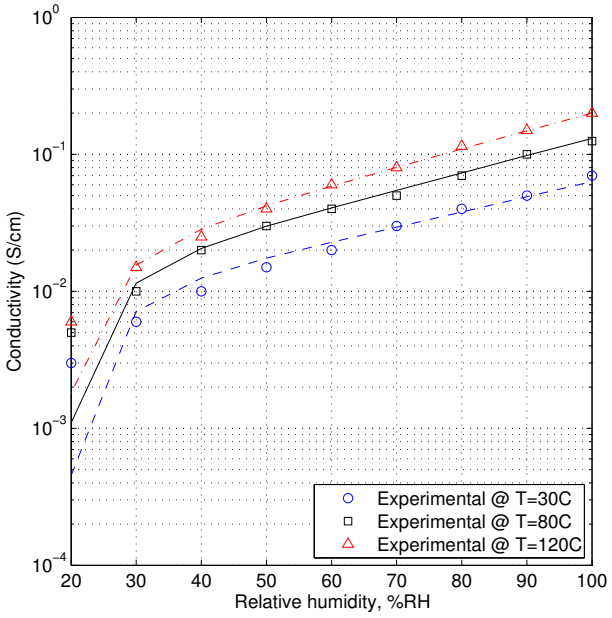

(b) Membrane conductivity at varying temperatures as a function of relative humidity.

Figure 3.3: Membrane sorption isotherm and the resulting membrane conductivity. Conductivity is calculated for NRE-211 from BekkTech [74] and presented as a function of λ in equation (3.20) but plotted here (in dashed lines) as a function of RH.

This source term is also included into the water vapour transport equation to enforce the conservation of mass.

$$\nabla \cdot (c_{tot} D_w^{eff} \nabla x_w) = R_w + S_\lambda$$

Effective Transport Properties - The system of equations is solved over multiple unique subdomains, each with different characteristics. In this work, these subdomains are comprised of porous materials and must account for multiple species transport. Therefore, the bulk properties for diffusion and conductivity don not apply, and must reflect transport in the pores. This work is based on that by Secanell [54] and similarly, percolation theory is used to model species transport through porous domains. In short, percolation theory states that there is a minimum volume fraction of the transporting medium for which transport will occur. Below this volume fraction, a network sufficient for transport does not exist. For example, a gas diffusing to all points in a random porous material (from one direction) must pass through an interconnected network of pores. In a random network of pores with a small volume fraction, it is unlikely that the pores at the inlet are connected to the pores in the middle of the domain, and even less likely that the gas will reach the outlet. It is postulated that there exists a threshold value of porosity (ε^{th}) below which transport does not occur.

$$D^{eff} = D \left(\frac{\varepsilon - \varepsilon^{th}}{1 - \varepsilon^{th}} \right)^{\mu} \Theta(\varepsilon - \varepsilon^{th}) \tag{3.24}$$

where $\Theta(x)$ is the Heaviside unit step function

$$\Theta(x) = \begin{cases} 0 & \text{for } x < 0 \\ 1 & \text{for } x > 0 \end{cases} \tag{3.25}$$

The constants in these functions depend strongly on the media being modeled. In particular, μ determines the shape of the curve, i.e. how quickly the curve approaches zero at low porosity and how it behaves at higher porosity. These values will be discussed in the context of 2 different materials used in PEMFC, isotropic and anisotropic.

Catalyst layers can be modeled as a random porous material with spherical particles, similar to the agglomerates discussed in chapter 2. It is generally accepted in percolation theory that μ lies between 1.7 and 2.0 for a three-dimensional lattice of this type, and that the threshold value can be determined experimentally [54]. The catalyst layer, however, has been shown to contain micropores on the scale

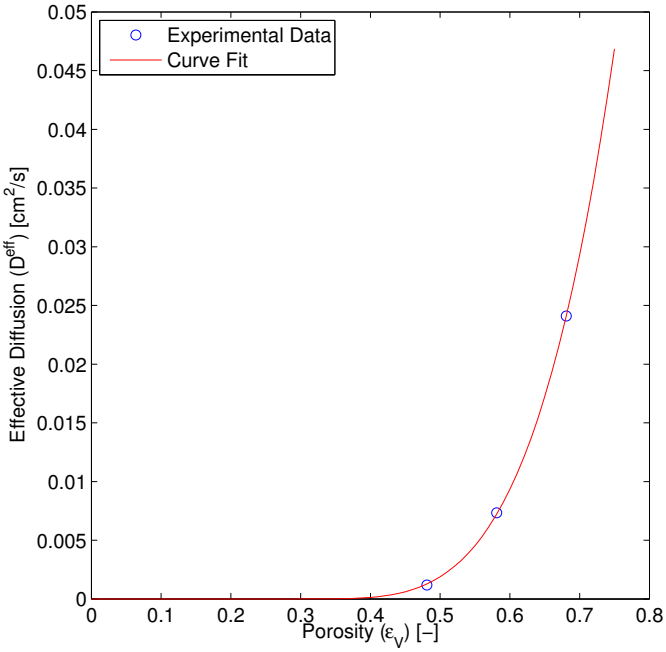

Figure 3.4: Curve fit of the oxygen diffusion coefficient from Yu and Carter [77] in electrodes of differing porosities.

where Knudsen effects are dominant [17]. In this work, percolation theory is used in conjunction with experimental data for diffusion in an electrode, rather than modeling the direct effect of diffusion in pores on the nanometer scale. The effective diffusion coefficient for oxygen is calculated in the cathode by fitting a curve to data recently presented by Yu and Carter [77]. Threshold value, ε^{th}, and μ are used to fit the data with the bulk diffusion coefficient fixed at a value given by the Chapman-Enskog equation. The porosity threshold is set to a value of 0.3, while μ was set to 4.0. This curve fitting allows for the values to be interpolated for electrodes with different porosities. The result of the curve fit is shown in Figure 3.4.

The GDL is a random porous material, however, most are constructed with carbon fibers in a certain orientation, making it anisotropic. The fibers lie flat and stacked on a plane. For fibers lying on the y-z plane, large pores are seen in the x-direction, which facilitate gas transport. Transport in the in-plane direction (y- or z-directions) is slightly more restricted, as gas moves around and along the fibers. Tomadakis et al. [78] found a relation that takes a similar form to percolation theory

Table 3.2: Percolation constants for each of the subdomains used in the MEA simulations

Parameter	Value
Gas Diffusion Layer (GDL)	
ϵ_V^{th}	0.118
μ_V^x	0.785, [79, 80]
μ_V^y	0.521, [79, 80]
ϵ_S^{th}	0.0
μ_S^x	1.5
μ_S^y	1.0
Microporous Layer (MPL)	
ϵ_V^{th}	0.118
μ_V	2.0
ϵ_S^{th}	0.118
μ_S	2.0
Catalyst Layer (CL)	
ϵ_V^{th}	0.3
μ_V	4.0
ϵ_S^{th}	0.118
μ_S	2.0
ϵ_N^{th}	0.0
μ_N	2.0

that applies to gas transport in fibrous materials.

$$D_i^{eff} = D\,\varepsilon\left(\frac{\varepsilon - \varepsilon^{th}}{1 - \varepsilon^{th}}\right)^{\mu^i}\Theta(\varepsilon - \varepsilon^{th}) \tag{3.26}$$

Using this method, the diffusion coefficient D_i^{eff} will be different for transport in multiple directions, i based on the choice of μ^i.

The GDL is also responsible for electron transport. In this case, however, electrons tend to encounter less resistance as they travel along the fibers in the y- and z-directions, whereas in the x-direction they are forced to constantly jump between the contact points on the overlying fibers. Percolation theory applies better to electron transport in the GDL. Secanell [54] discusses the transport phenomena in the GDL extensively and obtains values for threshold porosities and transport constants from experimental work [79–81].

Transport for each phase in the porous layer can be modeled by percolation theory; Table 3.2 shows the constants used in this work for each of the subdomains.

3.2.2 Solution Method

The system of nonlinear equations are solved using Newton's method by linearization. The solution, u, is updated iteratively until the residual $R(u^n)$, is reduced to the desired tolerance. Following the generic formulation for Newton's method,

$$\left[\frac{\partial R\left(u^n\right)}{\partial u}\right](-\delta u) = \left[R\left(u^n\right)\right] \tag{3.27}$$

Here, u must be defined as a vector of the solution variables to the system of equations R.

$$\vec{u} = \{x_{O_2},\ x_{H_2O},\ \phi_m,\ \phi_s,\ \lambda\} \tag{3.28}$$

The iterative nature of the problem requires an approximation of the residual for the right hand side of the equation. For a solution at iteration $n+1$, the equation is evaluated at iteration n. The linearized system is solved for the unknowns δu and the solution is updated.

$$u^{n+1} = u^n + \delta u$$

Each equation in the system must be transformed into the form presented in equation (3.27). For example, the first equation for oxygen transport

$$\nabla \cdot (c_{tot} D_{O_2}^{eff} \nabla x_{O_2}) = \frac{i_{CL}}{4F}$$

becomes

$$\nabla \cdot \left(c_{tot} D_{O_2}^{eff} \nabla \delta x_{O_2}\right) - \frac{1}{4F} \sum_j \left(\frac{\partial i_{CL}^n}{\partial u_j}\right) \delta u_j = \nabla \cdot \left(c_{tot} D_{O_2}^{eff} \nabla x_{O_2}^n\right) - \frac{i_{CL}^n}{4F} \tag{3.29}$$

Once the equations have been linearized, they can be discretized and applied to the grid using the finite element method (FEM). The Galerkin method is used to obtain the weak form of the problem. To achieve this, each of the variables is transformed to follow a standard shape function over each of the elements. The equation is then multiplied by a test function, w, and integrated over the domain, Ω. In the Galerkin method, the test and shape functions are identical. This method transforms the differential system into a linear algebraic system. The solution to the problem is a set of piecewise-continuous functions where the solution vector contains coefficients to the shape function at each of the nodes in the element.

The weak form of equation (3.29) can be written as

$$\int_\Omega w \nabla \cdot \left(c_{tot} D_{O_2}^{eff} \nabla \delta x_{O_2}\right) \mathrm{d}\Omega - \int_\Omega w \frac{1}{4F} \left(\sum_j \frac{\partial i_{CL}}{\partial u_j} \delta u_j\right) \mathrm{d}\Omega$$

$$= \int_\Omega w \nabla \cdot \left(c_{tot} D_{O_2}^{eff} \nabla x_{O_2} \right) \, \mathrm{d}\Omega - \int_\Omega w \frac{i_{CL}}{4F} \, \mathrm{d}\Omega$$

By applying the rules of vector calculus and Green's theorem, this equation becomes:

$$- \int_\Omega \left[\nabla w \left(c_{tot} D_{O_2}^{eff} \right) \nabla \delta x_{O_2} \right] \mathrm{d}\Omega - \int_\Omega w \frac{1}{F} \left(\sum_j \frac{\partial i_{CL}}{\partial u_j} \delta u_j \right) \mathrm{d}\Omega$$

$$+ \int_\Gamma \left[w \left(\vec{n} \cdot \nabla \left(c_{tot} D_{O_2}^{eff} \delta x_{O_2} \right) \right) \right] \mathrm{d}\Gamma$$

$$= - \int_\Omega \left[\nabla w \left(c_{tot} D_{O_2}^{eff} \right) \nabla x_{O_2}^n \right] \mathrm{d}\Omega - \int_\Omega w \frac{i_{CL}}{4F} \, d\Omega$$

$$+ \int_\Gamma \left[w \left(\vec{n} \cdot \nabla \left(c_{tot} D_{O_2}^{eff} \delta x_{O_2} \right) \right) \right] \mathrm{d}\Gamma$$

where Γ represents the boundary.

The gradient operators are applied in the x- and y-dimension in this case, and the discretization occurs by applying this equation to each individual element. The solution variables u are mapped to the element shape function w so that the solution is the scalar values at each node k on the element.

$$u = \sum_{k=1}^{N} u_k^{(e)} w_k^{(e)} \tag{3.30}$$

The integral terms on each element boundary become negligible, as internal boundaries are assumed to have continuity. For elements on the domain boundary, a mix of Dirichlet and Neumann conditions are applied. For the Dirichlet boundary conditions, the unknown is the change in the variable at the boundary, since the Newton method is being used. This term is constant between iterations so the contribution to the equation is 0 and can be dropped. For the Neumann boundary conditions, in all cases the fluxes are equal to 0, e.g.

$$\left(c_{tot} D_{O_2}^{eff} \right) \left(\vec{n} \cdot \nabla x_{O_2} \right) = 0 \tag{3.31}$$

and the term also disappears. In the case where the variable is not being solved in the domain adjacent to the boundary (e.g. λ is not solved in the MPL or GDL), the boundary effectively moves inward. In the global matrix there will be no interaction between the adjacent cells in the subdomains, therefore it behaves similar to a boundary. If a flux terms is not specifically applied at this internal boundary, then it will be 0.

The integrals over the cell are obtained by Gaussian integration at Gauss points determined by the order of the polynomial shape function.

Some of the nodal values are shared between adjacent cells, so the full system across the domain must be assembled. This results in a global system matrix and residual vector. FCST, the Fuel Cell Simulation Toolbox [54] is designed to assemble each cell matrix and residual and assemble the global equations cell by cell. FCST interfaces with a finite element library in C++ called deal.II (Differential Equations Analysis Library) [82], which provides state-of-the-art tools for grid handling, shape function and degree of freedom handling, solving, and output for post processing. It is important to note that over some of the subdomains, not all equations are assembled and solved. This is a product of using Newton's method to obtain the solution. Since the solution to the linear system gives the update vector for the variables, any variable that is known to not change can be dropped from the equations on the subdomain. For example, oxygen does not exist in any of the anode subdomains or in the membrane. The *initial solution* in these subdomains can be set to zero. As the Newton solver obtains a solution iteratively, the value is not updated since no equation is solved. This is one of the benefits to designing a specialized program for finite element analysis, as skipping assembly saves computational time and relaxes the resources required for the linear solver, which may need to handle many hundreds of thousands of degrees of freedom.

After the system is assembled using some of the tools from deal.II, the linear problem is solved by the direct solver UMFPACK [83], which is also used in other FEM software packages such as COMSOL[84]. Once a solution is obtained with the desired residual, a new system is solved on an adaptively refined grid to better approximate the solution in areas with the largest error. This usually corresponds to areas with the steepest gradients between cells.

Finally, the total cell current is obtained in the post-processing stage by integrating over the cells in the catalyst layer and evaluating the volumetric current density at the final solution. A typical measure of cell performance, the current density in A/cm^2, is evaluated based on the in-plane unit surface area of the cell, which is the y-z plane in this case. Since the simulations occur in the x-y plane and assumes a unit length in z, dividing the total cell by the height, y, will give the cell current density. i_{cell}.

3.2.3 Catalyst Layer Agglomerate Models

It is now necessary to discuss how the current density is obtained in the catalyst layer, and how the agglomerate model is integrated. This is not possible without first discussing the volume fraction relations within the catalyst layer.

From section 3.2.1.2 is it evident that the porosity of the media in each subdomain has an impact on the transport properties. In the GDL, the porosity can typically be obtained from the manufacturer, or by experimental testing. Furthermore, the remaining volume fraction is the solid material. In the catalyst layer, the parameters are not as easily obtained. The layer will have a solid, electrolyte, and pore phases. Conventional catalyst layers are fabricated with an ink comprised of the solid nanoparticles with ionomer in a solvent. The ink is applied to the membrane as a $10-20\mu m$ coating and dried so that the solvent evaporates. The structure that results is not evident, but it is clear that the ink composition will have an effect on the volume fractions. The structure and density of the materials can be used to estimate the volume fraction of solid in the layer [85]

$$\varepsilon_S = \left(\frac{1}{\rho_{Pt}} + \frac{1 - Pt|C}{Pt|C\, \rho_c} \right) \frac{m_{Pt}}{L^{cl}} \tag{3.32}$$

where ρ_{Pt} and ρ_c are the platinum and carbon densities, $Pt|C$ is the platinum to carbon ratio of the support particles, m_{Pt} is the platinum loading in the CL, and lastly, L^{cl} is its thickness. All of these parameters are known prior to catalyst layer fabrication with the exception of the thickness, which can be measured post-fabrication.

Similarly, the volume fraction of electrolyte can be found if its mass fraction (X_N) in the ink composition is known [85]

$$\varepsilon_N = \frac{X_N}{\rho_{N,dry}(1 - X_N)} \frac{1}{Pt|C} \frac{m_{Pt}}{L^{cl}} \tag{3.33}$$

The porosity of the layer (ε_V) is then given by the remaining volume fraction.

$$\begin{aligned} \varepsilon_S + \varepsilon_N + \varepsilon_V &= 1 \\ \varepsilon_V &= 1 - (\varepsilon_S + \varepsilon_N) \end{aligned} \tag{3.34}$$

This characterization of the catalyst layer seems to be independent of the assumed structure, i.e. the presence of agglomerates. The macroscale properties, however, directly affect the assumptions made about agglomerates. The pore structure on the inside of agglomerates will be on the nano-scale, and are called the

primary pores in the CL, while the larger pores at the macroscale are called secondary pores. In most models using agglomerates, the primary pores are assumed to be filled with ionomer. Few studies, however, link the macroscale properties to the agglomerate microstructure. Secanell et al. developed relations to describe this inextricable link [33]. They describe the solid and electrolyte volume fractions by the (ionomer-filled) agglomerate structure:

$$\varepsilon_S = n_{agg}\left(\frac{4}{3}\pi r_{agg}^3\left(1-\epsilon_{agg}\right)\right) \tag{3.35}$$

$$\varepsilon_N = n_{agg}\frac{4}{3}\pi\left(r_{agg}^3\left(\epsilon_{agg}-1\right)+\left(r_{agg}+\delta_{agg}\right)^3\right) \tag{3.36}$$

$$\varepsilon_V = 1-\varepsilon_S-\varepsilon_N \tag{3.37}$$

where n_{agg} is the number of agglomerates per unit volume in the catalyst layer. Since the solid volume fraction is known, n_{agg} can be determined through equation (3.35). Note that this is contingent on the assumption that the agglomerates are perfectly spherical, and that a size and porosity of the agglomerate is known. Obtaining the electrolyte volume fraction from equation (3.33) also allows the thickness of the thin film, δ_{agg}, to be determined. This effectively reduces the number of unknown structural parameters of the agglomerate that must be chosen for the simulation to two, r_{agg} and ϵ_{agg}.

An alternate assumption can be made for the primary pores; they can be filled with water. This is discussed at length in Chapter 2, but what effect does that have on the catalyst layer structure? If the primary pores are filled with water, ionomer can only exist on the outside of the agglomerate and thus, the thin film must be thicker. The primary pores are still not gaseous under this assumption, so the volume of water must now be accounted for. These changes can be reflected in the equations for the ionomer and pore volume fractions.

$$\varepsilon_N = \frac{4}{3}\pi n_{agg}\left(r_{agg}^3\left(\epsilon_{agg,N}-1\right)+\left(r_{agg}+\delta_{agg}\right)^3\right) \tag{3.38}$$

$$\varepsilon_W = n_{agg}\left(\frac{4}{3}\pi r_{agg}^3\epsilon_{agg,W}\right) = \frac{\varepsilon_S\epsilon_{agg}}{1-\epsilon_{agg}} \tag{3.39}$$

$$\varepsilon_V = 1-\varepsilon_S-\varepsilon_N-\varepsilon_W \tag{3.40}$$

Equation (3.38) is remarkably similar to that developed by Secanell et al. [33] (3.36), except for the definition of $\epsilon_{agg,N}$ - the fraction of agglomerate containing ionomer. Similarly, the fraction of water in the CL is given by equation (3.39), where

$\epsilon_{agg,W}$ is the fraction of the agglomerate containing water. In this case, $\epsilon_{agg,N}$ and $\epsilon_{agg,W}$ will be zero and the agglomerate porosity, respectively. But defining the variables in this way allows more flexibility in the model, i.e. cases between these two extremes can be investigated. Finally, it is shown through equation (3.40) that the assumed porosity of the CL is reduced by making the water-filled assumption.

The catalyst layer porosity has two effects on the model. The first is that oxygen diffusion in the catalyst layer will be more limited and restrict the oxygen available for the reaction. The second is a more numerical effect that comes from taking a volume averaged approach. The reaction source terms in system (3.5) are defined as the reaction rate per unit volume of the catalyst layer. The current densities given by the agglomerates, however, are defined using a spherical reference volume that only represents the solid and ionomer (and water) phases in the CL. The representative volume of the agglomerate therefore does not take the CL porosity into account. As a result, the agglomerate current must be scaled to the catalyst layer reference volume.[1]

$$i_{CL} = i_{agg}\left(1 - \varepsilon_V\right) \tag{3.41}$$

Changing the porosity will therefore have multiple and compounded effects on the results of the MEA model.

At the cathode, the agglomerate models presented in Chapter 2 are used to predict the current. A similar formulation for the current in an agglomerate is given at the anode, however, dual-path kinetics from Wang et al. [86] is used to describe the reaction rate.

3.2.3.1 Implementation

Agglomerate CL models in the literature use an analytical expression to obtain the current density, such as that described in section 2.2.2.2 and Appendix A.1. These analytical expressions limit the range of applicability of the model as they are restricted by further assumptions. It is desirable to have a flexible agglomerate model. This, however, requires that a solution must be obtained numerically (see section 2.2.2.1). Such an implementation is called a multiscale model; an agglomerate problem is solved to give properties described on the sub-grid scale of the FEM problem. Using these sub-grid calculations is practical in that it avoids redefining the whole problem or changing the grid to represent a microstructure. On the other hand,

[1] See also equation (A.27) in Appendix A.1

it is impractical as it adds complexity and - perhaps most importantly - time to the numerical simulation. The implementation of a multiscale agglomerate model is also not a trivial task; only a single example in 1D has been found in the literature related to fuel cell modeling [35]. Figure 3.5 shows the difference in the process for the analytical and multiscale agglomerate model, as applied to the cathode.

For this MEA model, there are two requirements of a multiscale agglomerate: accurately predict the current, and obtain a good estimate of the derivatives with respect to each of the solution variables. In terms of the equations presented in section 3.2.2, the agglomerate must be able to give i_{CL} and $\frac{\partial i_{CL}}{\partial u_j}$ for all u_j. The former is inherent in the model and described in Chapter 2; the latter must be obtained by numerical differentiation. While an analytical derivative would be more efficient, using the numerical derivative is much more convenient. The MEA model required a gradient with respect to the solution variables at the boundary of the agglomerate. Analytically, this is very difficult to obtain, as the entire solution is dependent on this value. The analytical derivative of the current density can be obtained for any point within the agglomerate, i.e. $\frac{\partial i(r)}{\partial u_j}$, but this does not capture the interaction between all other points. These derivatives, however, can be obtained numerically by simply perturbing the input variables. A simple method is forward differencing, where the gradient is calculated based on the secant between two points.

$$\frac{\partial f(\vec{x},\vec{u})}{\partial u_i} = \frac{f(\vec{x},\vec{u}+\delta u_i) - f(\vec{x},\vec{u})}{\delta u_i} \tag{3.42}$$

where δu_i is the perturbation, or step size around the point. The choice in step size is important for nonlinear models, as it will determine the accuracy of the gradient. Too large and accuracy is lost; too small and there is a risk that rounding error becomes a factor. To reduce this risk, step size analysis was performed for both models across the range of operating conditions. The solution was found to be nearly linear with oxygen concentration, however, the model is very nonlinear with respect to the overpotential, so this is the more critical test.

A useful benchmark for accuracy appears for both the water-filled and ionomer-filled agglomerate models. Based on the use of Butler-Volmer kinetics and the simplified Tafel equation, the derivatives with respect to solid potential and electrolyte potential should be equal and opposite since $\eta_c = E^{eq} - (\phi_s - \phi_m)$. This can be used as a numerical test for accuracy. The figures below show the phenomenon at work. To normalize the results for any reaction rate, the results were transposed to

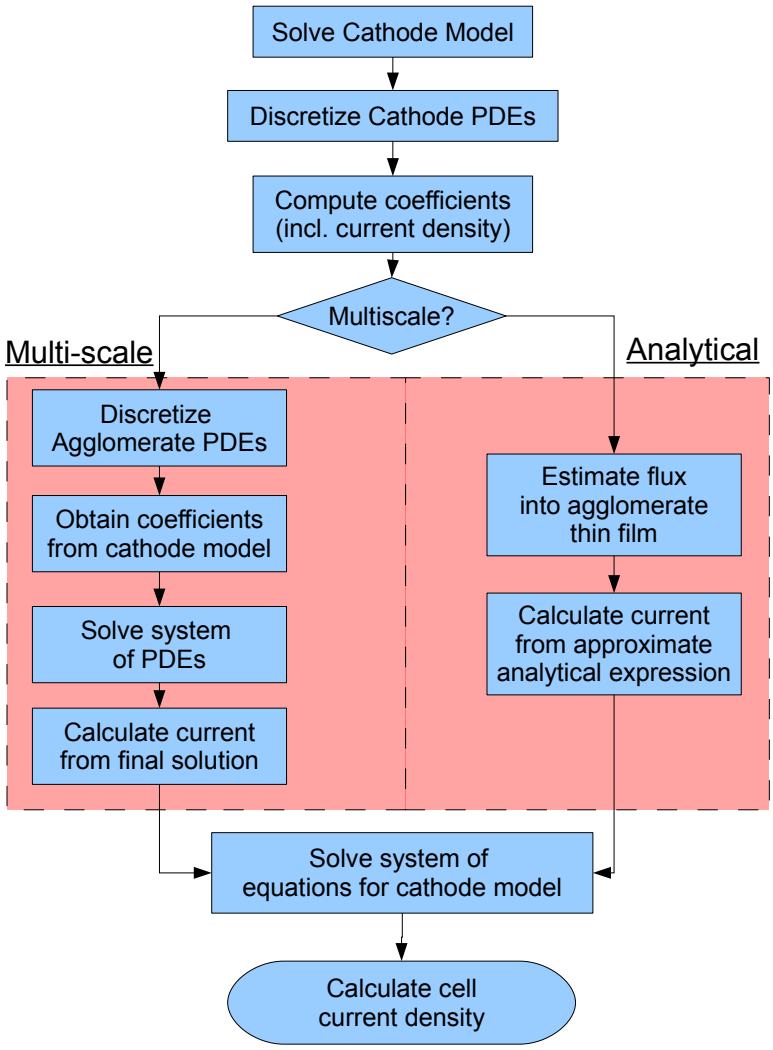

Figure 3.5: Flowchart for the implementation of a multiscale agglomerate model. The agglomerate is used to predict the local volumetric current density for the system of equations in the FEM formulation. In the case of a multiscale model, a separate system of equations must be solved for the agglomerate, and post-processing yields the current density. This adds significant time and computational requirements to the finite element simulation.

0 - the point where the gradient with respect to each of the potentials were of equal magnitude (the assumed "Actual Gradient"). The gradients are then normalized to show percentage change. For example

$$\% \text{ Deviation } = \frac{\text{Estimated Gradient - Actual Gradient}}{\text{Actual Gradient}} \times 100\% \tag{3.43}$$

The figures in 3.6 show a sample of the results at two different overpotentials for both the water-filled and ionomer-filled agglomerate models. All of the results show a zone of numerical instability for very small step sizes, typically below $10^{-10}\,V$. There exists a range of step sizes for both models where the gradients level off around a common point, which can be said to be the most accurate approximation of the gradient for forward differencing. For step sizes that are too small, the gradients are not accurate enough due to the non-linearity of the solution. A step size of $10^{-7}\,V$ was chosen to approximate the gradient for the multiscale model.

3.3 Results and Discussion

The above discussion is a summary of the model development by Secanell et al. [54]. Their MEA model, and reduced models of the anode and cathode have been validated numerically and experimentally, and used in many publications for design and optimization. [11, 33, 52–54, 56, 87] The contribution from this work comes from the integration of the multi-scale agglomerate models into the cathode catalyst layer. In this section, characteristic results from the model will be explained. The multi-scale model will be validated against an analytical model based on the work by Secanell et al. [33] and Sun et al. [4] to ensure accurate implementation. Finally, the difference between the water-filled and ionomer-filled agglomerates in the context of the catalyst layer - a comparison never before seen in the literature.

3.3.1 Characteristic Solution

The model equations are solved over the grid with the subdomain sizes listed in Table 3.3. Each of the subdomain properties is listed in Table 3.4, and a particular focus is put on the catalyst layer structure and microstructure in Table 3.5. Finally, the transport and electrochemical properties of each of the layer are listed in Tables 3.6 and 3.7, respectively.

The finite element problem is solved on a grid discretized using Lagrangian elements with quadratic shape functions. A Newton solver with a parabolic line

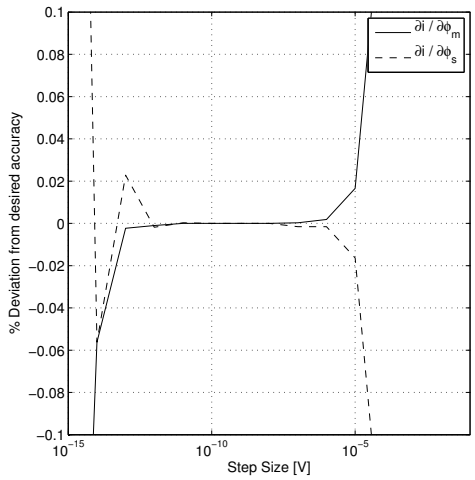

(a) Gradient accuracy of the ionomer-filled agglomerate at 0.2V overpotential

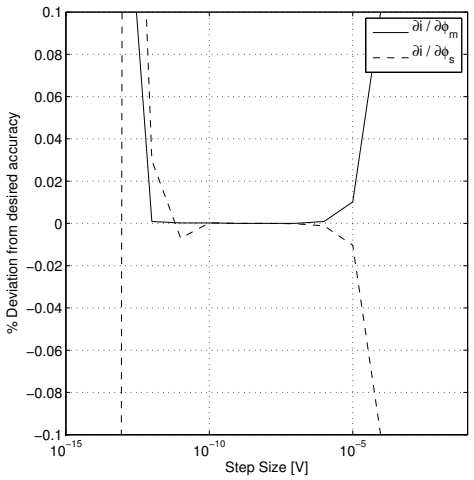

(b) Gradient accuracy of the ionomer-filled agglomerate at 0.5V overpotential

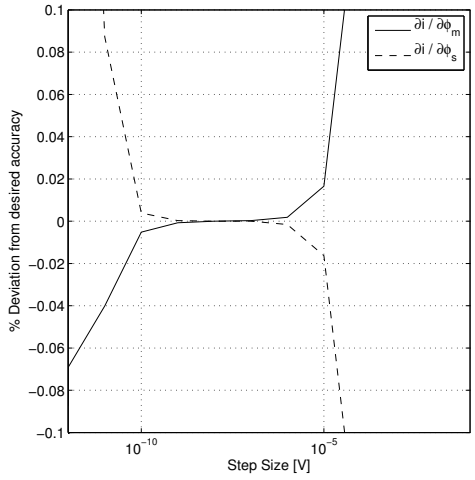

(c) Gradient accuracy of the water-filled agglomerate at 0.2V overpotential

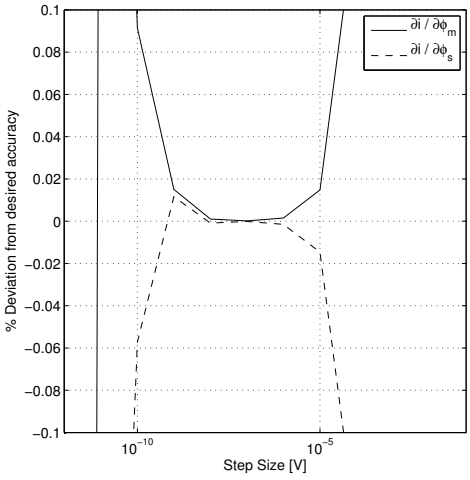

(d) Gradient accuracy of the water-filled agglomerate at 0.5V overpotential

Figure 3.6: Gradient accuracy by step size for multiscale agglomerate models

Table 3.3: Electrode geometry

Parameter	**Value**
Channel width, [cm]	0.1
Current collector width, [cm]	0.1
GDL thickness, L^{gdl}, $[\mu m]$	250
MPL thickness, L^{mpl}, $[\mu m]$	50
CL thickness, L^{cl}, $[\mu m]$	10
Membrane thickness, L^{m}, $[\mu m]$	25

Table 3.4: GDL, MPL, CL, and Membrane physical properties

GDL Structure	
ε_S	0.6
ε_V	0.4
MPL Structure	
ε_S	0.4
ε_V	0.6
CL Physical Properties	
ρ_{Pt}, $[g \cdot cm^{-3}]$	21.5, [49]
ρ_c, $[g \cdot cm^{-3}]$	2.0, [49]
ρ_N, $[g \cdot cm^{-3}]$	2.0, [49]
Nafion loading (%wt)	30
m_{Pt}, $[mg/cm^2]$	0.4, [88]
$Pt\|C$	0.46, [88]
A_v, $[cm^2 \cdot cm^{-3}]$	2×10^5
Membrane Properties	
EW, $[g \cdot mol^{-1}]$	1100

search method is used to obtain convergence down to 10^{-9}, i.e. the L2 norm of the total residual vector for all five variables is smaller than 10^{-9}. The grid is refined adaptively, whereby 30% of cells with the largest errors (by interior boundary fluxes) are chosen for refinement. The current density is evaluated at every level of refinement to check for a grid independent solution.

The catalyst layer of this MEA model uses the analytical approximation of current density given by the ionomer-filled agglomerate model. This expression is modified from the works by Secanell et al. [11, 33, 54] and thus the results will not be identical. Chapter 2 confirmed that this expression matches the 1D model and therefore can be used for validation of the multiscale MEA model. Recall equation

Table 3.5: CL Structure and Microstructure by agglomerate type

	Agglomerate Type	
	Water-filled	Ionomer-Filled
ε_S	0.253	0.253
ε_N	0.186	0.186
ε_W	0.084	-
ε_V	0.476	0.560
CL Microstructure		
r_{agg} $[nm]$	100	100
ϵ_{agg}	0.25	0.25
δ_{agg} $[nm]$	15.8	9.2

Table 3.6: GDL, MPL and CL transport properties

Parameter	**Value**
Bulk gas diffusion properties	
D_{O_2,N_2}, $[cm^2 \cdot s^{-1}]$	0.2741, [89]
D_{H_2O,N_2}, $[cm^2 \cdot s^{-1}]$	0.2907, [89]
D_{H_2O,H_2}, $[cm^2 \cdot s^{-1}]$	1.1390, [89]
GDL physical properties	
$\sigma^{gdl}_{S,XX}$, $[S \cdot cm^{-1}]$	16.03
$\sigma^{gdl}_{S,YY}$, $[S \cdot cm^{-1}]$	272.78
MPL physical properties	
σ^{mpl}_{S}, $[S \cdot cm^{-1}]$	88.84
CL physical properties	
σ^{cl}_{S}, $[S \cdot cm^{-1}]$	88.84
σ^{cl}_{N}, $[S \cdot cm^{-1}]$	$(0.005139\lambda - 0.00326)e^{1268(\frac{1}{303}-\frac{1}{T})}$
$H_{O_2,N}$, $[\frac{Pa \cdot cm^3}{mol}]$	3.1664×10^{10}, [4]
$H_{H_2,N}$, $[\frac{Pa \cdot cm^3}{mol}]$	6.94×10^{10}
$D_{O_2,N}$, $[cm^2 \cdot s^{-1}]$	$9.726\, e-6$ (cm^2/s), [70]
$D_{H_2,N}$, $[cm^2 \cdot s^{-1}]$	12.8×10^{-6}, [90]
Membrane Properties	
k, $[s^{-1}]$	1×10^4 [54]
n_d	1.0 [32]

Table 3.7: Catalyst layer electrochemical properties

Parameter	**Value**
Cathode electrochemical properties	
α	1, [12, 13, 64]
n	4, [4, 12, 13]
γ_{O_2}	1.0, [4, 12, 13]
γ_H	1.0, [7, 12, 13]
i_0^{ref}, $[A \cdot cm^{-2}]$	2.707×10^{-8}[12, 13]
$c_{O_2}^{ref}$, $[mol \cdot cm^{-3}]$	0.725×10^{-5}, [12, 13]
Anode electrochemical properties	
j_{OT}, $[A \cdot cm^{-2}]$	0.47, [86]
j_{OH}, $[A \cdot cm^{-2}]$	0.01, [86]
γ	1.2, [86]
$c_{H_2}^{ref}$, $[mol \cdot cm^{-3}]$	0.59×10^{-6}, [90, 91]

(2.46) for the volumetric current density

$$i_{agg} = 4F\bar{V}_{agg}\frac{P_{O_2}}{H_{O_2,N}}\left[\frac{1}{E_r k_c} + \frac{\delta_{agg} r_{agg}^2}{3\left(r_{agg} + \delta_{agg}\right) D_{O_2,N}}\right]^{-1}$$

Transport phenomena across the full MEA are shown in Figures 3.7 and 3.8. This simulation is of a cell at a constant temperature of 80℃ , where the anode and cathode gas streams are maintained at 1atm pressure with 70% relative humidity. The cell voltage is maintained at $0.7\,V$ resulting in a cell current density of $0.215\,A/cm^2$. A cell voltage of $0.7\,V$ was chosen to illustrate the phenomena in the cell at a moderate performance point. The operating point is near the center of the polarization curve and shows kinetic effects in the CL, and the onset of diffusive and ohmic effects. This is not, however, demonstrative of the mass transport limitations that become influential on cell performance at higher current densities.

Starting with the oxygen profile in Figure 3.7(a), it can be seen that from the inlet the air diffuses through the anisotropic GDL, encountering much less resistance in the x-direction towards the CL compared with the y-direction under the current collector. The sharp change in the contour occurs when oxygen reaches the MPL, which is of much lower porosity. The reaction proceeds in the CL and consumes available oxygen. The membrane, however, represents a boundary so that no oxygen can diffuse and enter the anode. Water, however, exists on both sides of the membrane, and is shown in Figure 3.7(b). It is shown here that the cell is well humidified as there is not much variation in the mole fraction from the 70% RH at the inlets. Water is in higher concentrations under the land area of the cathode, as

is it being produced by the reaction. From here it has two paths to exit the cell. The first is back towards the channel, so it must diffuse through the MPL and GDL. The second is to absorb into the membrane and diffuse towards the anode side. This process can be seen in Figure 3.8(b), an exploded view of the two catalyst layers and the membrane. Higher concentrations of absorbed water (λ) exist on the cathode side, and therefore water will follow the concentration gradient to the anode, where it hydrates the ACL, and can go through desorption process into the gas phase.

The solid phase (electric) potential, shown in Figure 3.7(c), is set to a reference of 0 at the anode side and to the cell voltage of $0.7V$ at the cathode current collector. The electric potential sees little to no variation within the anode and cathode sides, on the order of $1.5\,mV$ in each with most of the losses from poor conduction in the through-plane direction in the GDL.

The electrolyte potential is plotted in Figure 3.8(a) across the anode catalyst layer, membrane, and cathode catalyst layer. There are only marginal losses on the anode side due to good proton conduction and fast reaction kinetics. The losses are purely ohmic and thus linear through the membrane but only amount to roughly $15\ mV$. The remaining losses come in the cathode catalyst layer where proton transport is more limited than in the membrane, and sluggish reaction kinetics cause high activation losses.

The phenomenon occurring in the cathode are of particular interest. Figure 3.9 shows the oxygen, overpotential, and current density profiles within the catalyst layer. The overpotential is defined as: $\eta_c = E^{eq} - (\phi_s - \phi_m)$, but the variation in ϕ_s is less that $0.1mV$ within the catalyst layer. Since the equilibrium potential is constant, all of the variation comes from ohmic and activation losses in the electrolyte potential - ϕ_m. Oxygen variation within the layer is plotted in Figure 3.9(a), but the variation is small. The reaction is therefore mostly driven by the overpotential, as can be seen by the similarities in Figures 3.9(b) and 3.9(c).

3.3.2 Multiscale Validation

The characteristic solution above was obtained using an analytical model for the agglomerate current density. Chapter 2 showed that the analytical and numerical models give identical results for a reaction that is first order with respect to oxygen concentration. In this section the numerical model will be integrated into the catalyst layer and the model above will be used to validate the implementation.

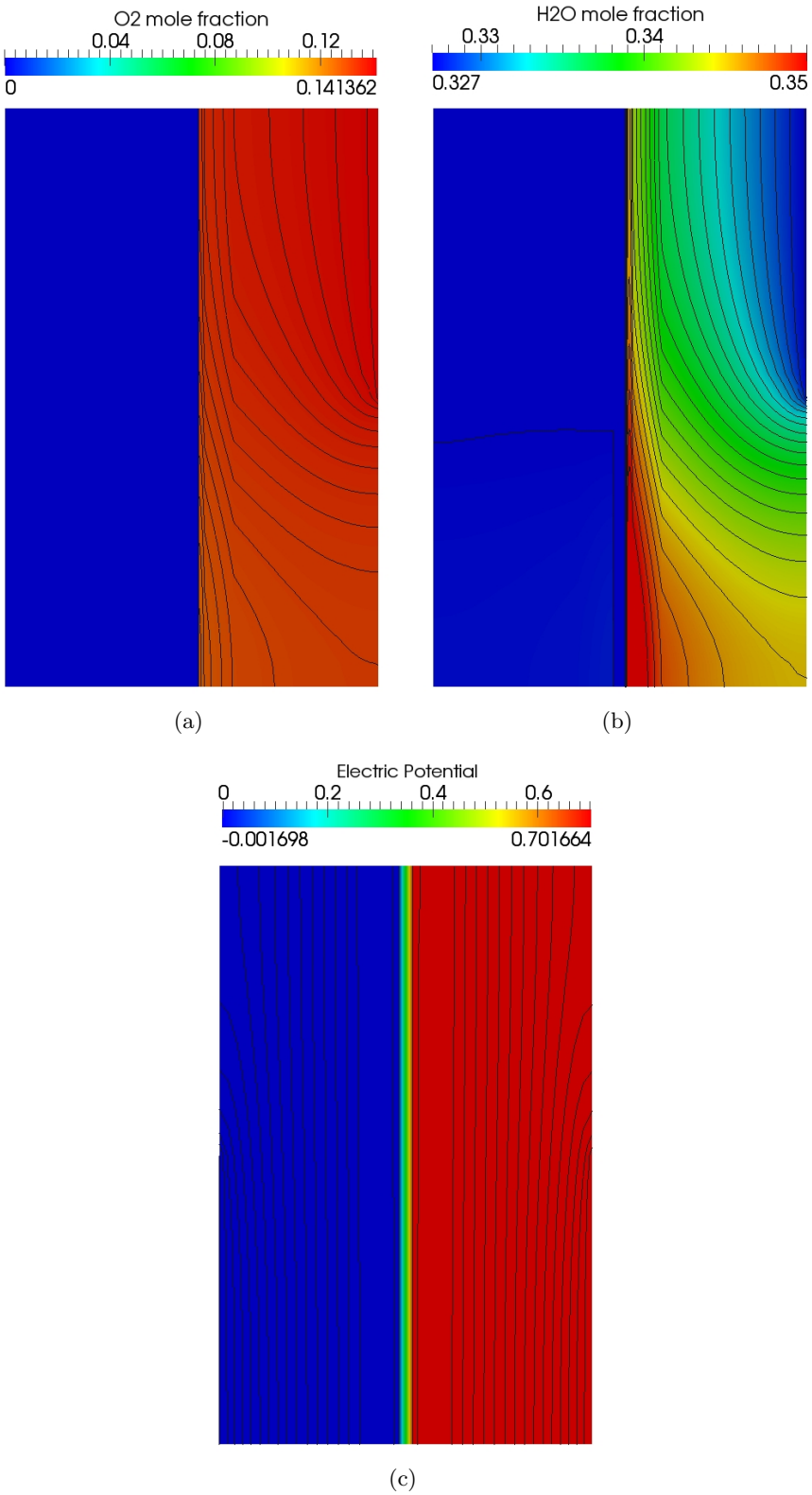

Figure 3.7: (a) Oxygen, (b) water vapour, and (c) electric potential distributions within the MEA. Refer to Figure 3.2 for the domain layout.

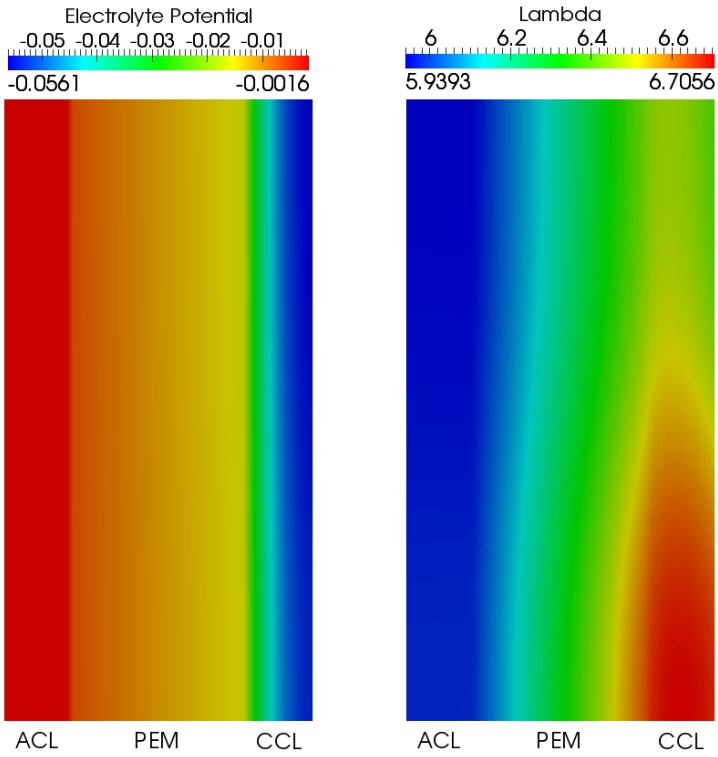

(a) (b)

Figure 3.8: (a) Electrolyte potential and (b) membrane water content distributions through the ACL, PEM, and CCL. The thickness has been expanded 10x for clarity)

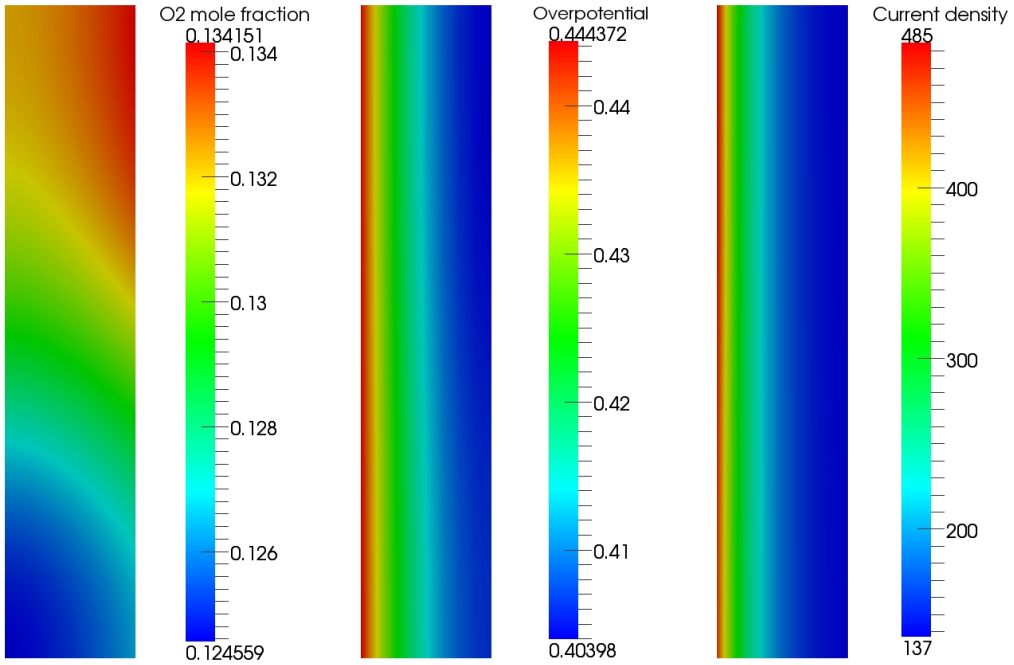

(a) (b) (c)

Figure 3.9: (a) Oxygen, (b) overpotential, and (c) current density profiles in the cathode catalyst layer. The CL thickness ($10\,\mu m$) has been enlarged 20X for clarity.

The first test is to confirm the convergence of the model using the analytical agglomerate expression. The convergence tolerance is first set to a value of 10^{-9}. This means that the L2 norm of the total residual vector for all 5 variables will be less than 10^{-9}. This is a strict convergence tolerance and with the numerical agglomerate model this may lead to prohibitively long computational times. The convergence tolerance will be relaxed to 10^{-6}, but first it must be confirmed that the model produces the same results.

A grid study at the two levels of convergence is presented in Figure 3.10. The study was performed at two different current densities to ensure adequate convergence over the range of operating conditions. Figures 3.10(a) and 3.10(b) show the results at a cell voltages of $0.7\,V$ and $0.4\,V$, producing current densities of $215\,mA/cm^2$ and $1444\,mA/cm^2$, respectively. The high current density case will be the best indicator of convergence, as further refinement of the grid and added degrees of freedom (dof) will more accurately capture the large variations over the small width of the catalyst layer. The figures allow two conclusions to be drawn. Firstly, relaxing the convergence tolerance to 10^{-6} does not change the results down to the

Table 3.8: Multiscale agglomerate validation showing the current densities of the MEA for different agglomerate model configurations

	Analytical	Multiscale	Multiscale (averaged)
$i_{cell}(0.7V)$ $[mA/cm^2]$	215.209	215.208	215.177
$i_{cell}(0.4V)$ $[mA/cm^2]$	1443.98	1443.97	1442.59

desired level of precision (which is given here to 6 significant digits or $0.001 mA/cm^2$). Secondly, refining the grid adaptively to approximately 100,000 degrees of freedom is more than sufficient to get a grid independent solution at any condition. The current density is an integral quantity of the grid, dependent on all of the solution variables, so it is a very good indicator of a grid independent solution. The difference in current density between the lowest level of refinement (30,000 dofs) and the highest is less than 1%, while changes from 50,000, to 100,000, to 200,000 dofs change the current less than 0.1%. This is a strong indication that the solution at these two points is stable.

The multiscale model using an ionomer-filled agglomerate is tested against these two cases to validate the implementation. The grid refinement is stopped at approximately 100,000 dofs with a convergence tolerance of 10^{-6}. Table 3.8 lists the difference between the two models at low and high current density. The multiscale model has two values. The first is the value given by assuming an identical implementation of the model at the cell level. The values at each quadrature point in the cell are required to obtain an accurate value for the integral in the assembly of the system matrix. Since the model uses 2^{nd} order elements, this means that 9 evaluations are required per cell, which is computationally costly for solving the agglomerate model. If the element is sufficiently small the variation in the solution variables should also be small, and the values can be averaged to obtain a single value of current density. The second value is the current density obtained if the averaging method is used. It can be seen that the multiscale model and analytical model are nearly identical, while the averaging technique changes the current density by approximately 0.1% in both cases. Averaging the current across the cell leads to slower convergence of the Newton solver, but still saves computational time (40% in this case).

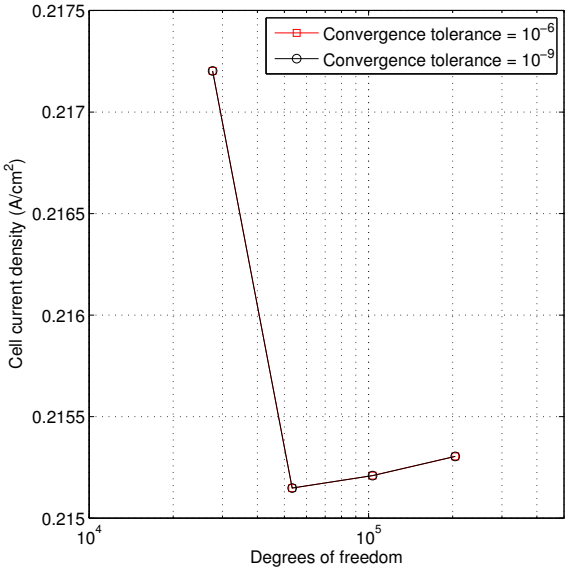

(a) Grid study at low current density

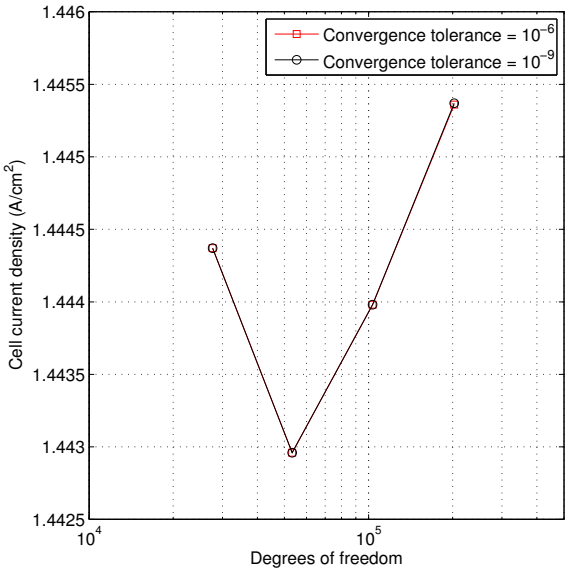

(b) Grid study at high current density

Figure 3.10: Grid study at two levels of convergence tolerance. The study is performed at low and high current densities to ensure convergence over the operating range of the cell. The evaluation of current density is an indicator of a stable, grid-independent solution.

3.3.3 Water-Filled Agglomerate Multiscale Model

The previous section demonstrated that a multiscale implementation of the ionomer-filled agglomerate model was successful. Chapter 2 directly compared individual water-filled agglomerates to ionomer-filled. The two agglomerates must lastly be compared in the context of the full MEA. The comparison will be made on two levels, the polarization curve for overall effects and within the catalyst layer to investigate the local effects.

Comparing the polarization curves for the two types of agglomerates will give an indication of the transport limitations at the nanoscale, but since the assumption of agglomerate type reflects the structure of the catalyst layer (see Table 3.4), macroscale transport effects must also be taken into account. Figure 3.11 shows the performance curves for the two different models at 80℃, and inlet pressures of 1atm with 70% relative humidity. For the water-filled agglomerate, convergence of the model could not be obtained for current densities higher than 1 A/cm^2. As discussed in Chapter 2, the agglomerate model is sensitive to input parameters and a generalized solution method for all operating conditions is difficult to develop. Conditions vary widely in the catalyst layer when high currents are being drawn, and a single point for which a solution can not be obtained causes the program to fail. Nevertheless comparisons can be made through the kinetic and the ohmic region, and towards the start of the mass transport region of the curve.

From a broad perspective, the figure shows that the difference in the predictions between the two models are quite small and, therefore, the type of agglomerate does not significantly affect fuel cell performance predictions under these conditions. This result provides more insight into the difference between the two types of agglomerate models at the catalyst layer level. However, the results are only shown for a single set of operating conditions due to the length of time required per simulation. In the most extreme case, a single data point took nearly 57 hours to obtain. Further investigation is required and may reveal larger differences. Some important differences between the two models can still be observed at these conditions.

The only differences in the kinetic region come from the volume averaging approach in the catalyst layer. The two agglomerates will produce roughly the same current density, but since the catalyst layer porosity is reduced with a water-filled

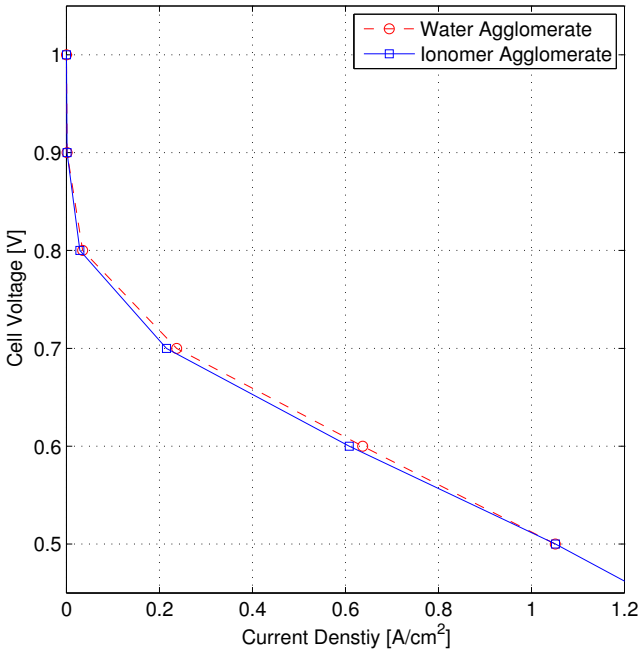

Figure 3.11: Comparison of multiscale agglomerate models

agglomerate, a higher average current is observed at the catalyst layer level. Recall

$$i_{CL} = i_{agg}\left(1 - \varepsilon_V\right)$$

Once operating in the ohmic region the water-filled agglomerate outperforms the ionomer-filled. This is as anticipated by the results shown in Chapter 2. Around $1\,A/cm^2$, the water-filled model starts experiencing mass and charge transport limitations inside the agglomerate and, as a result, water and ionomer-filled models provide the same results. If the trend were continued, higher transport losses would occur with the water-filled model at both the micro- and macro-scale. These trends could only be simulated previously in the literature using ionomer-filled agglomerates with very large radii [92], well beyond the size observed in microscopy studies [39].

The polarization curves in Figure 3.11 provide a unique opportunity to look at the differences between the two agglomerates in the catalyst layer. At a cell voltage of $0.5\,V$ the two models give exactly the same current of $1.05\,A/cm^2$. All of the cell components are identical, and thus the only differences will come from the distribution of reactants and current in the CL - a direct result of the differences in the agglomerates. Figure 3.12(a) shows the difference between the oxygen distributions for catalyst layers with ionomer-filled agglomerates (left) and water-filled

agglomerates (right). It is immediately clear that the lower porosity in the layer causes greater transport resistance for oxygen. The same results can be seen in Figure 3.12(b), where the water produced by the reaction does not diffuse as easily out of the CL and towards the channel. The partial pressure is very close to saturation pressure for these conditions. This drives the absorption rate up towards the membrane, keeping it well hydrated and water flowing to the anode side.

The oxygen concentration at the CL-MPL boundary (right) is nearly identical for both models; towards the membrane, oxygen depletion with the water-filled model is significant, especially under the current collector. The oxygen depletion is also due to the differences in reaction rates from the two agglomerates. Figure 3.13 shows the differences in the reaction profiles for the given overpotentials. It can be seen in Figure 3.13(a) that the overpotential distribution does not change significantly between the two models, however, the overpotentials are starting to be in the range where there is a notable discrepancy in the agglomerate models. This is shown in Figure 3.13(b), where the reaction rates towards the MPL are higher for the water-filled model, but are flatter towards the membrane than the ionomer-filled model due to the drop in oxygen concentration.

The reaction for the ionomer-filled model is much more shifted towards the membrane; through the first 60% of the thickness, the current densities are much higher than the water-filled model. However, it drops much lower closer to the MPL. The interesting comparison between these two models is that they give the same average current density over the catalyst layer. This means that the disparity in current density towards the membrane is balance by the inverse trend towards MPL. This phenomenon is similar to the processes occurring within the agglomerates themselves, where the water-filled model has a much flatter reaction profile.

The results shown here have implications for catalyst layer and cell design. For example, if modeling studies indicate that the reaction is heavily shifted towards the membrane, a case can be made to fabricate a catalyst layer which takes advantage of this effect, e.g. changing the platinum loading in certain areas. The water-filled model shown here still indicates a reaction shifted towards the membrane, but not quite as dramatically; the reaction is more evenly distributed through the thickness. It is evident that the difference in results can sway design decisions, and lead to a better understanding of the processes occurring within the cell.

The results are highly dependent on the choice in parameters - kinetic, transport,

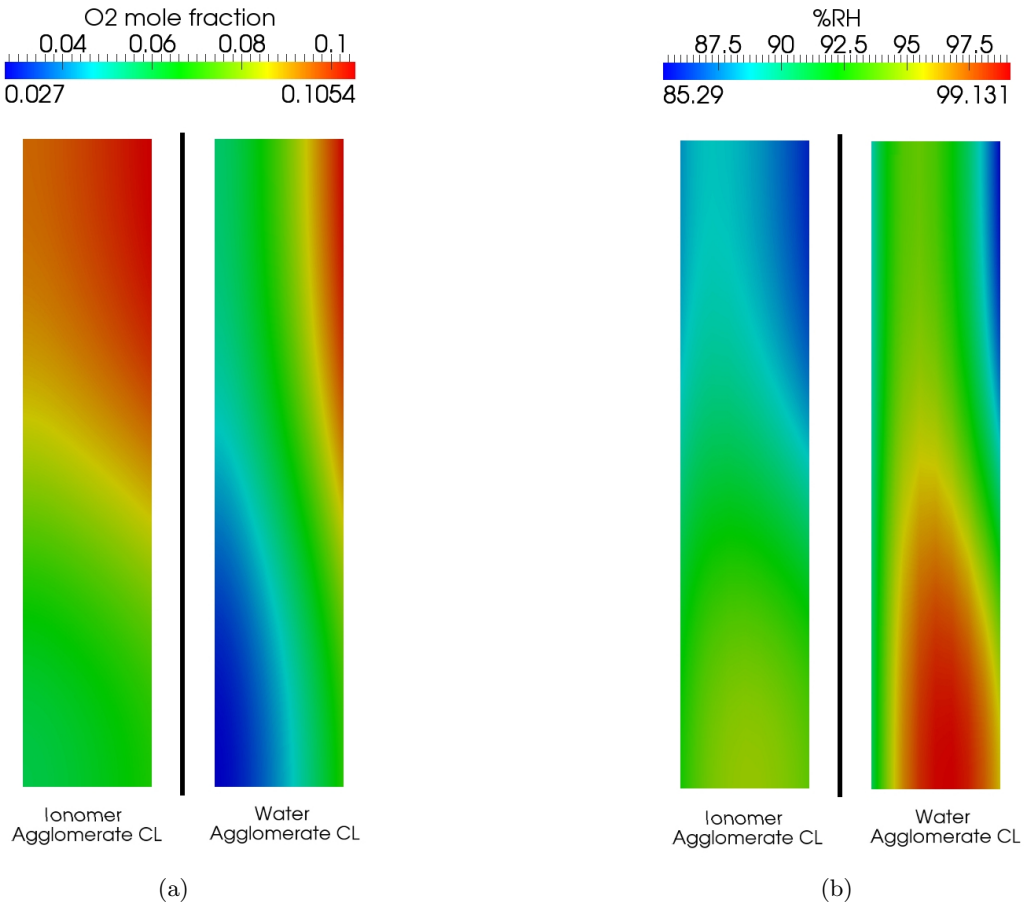

(a) (b)

Figure 3.12: Distribution of (a) oxygen and (b) water vapour within the cathode catalyst layer at 1.05 A/cm^2. The CL thickness (10 μm) has been enlarged 20X for clarity. The catalyst layer with ionomer-filled agglomerates is shown on the left and the water-filled agglomerates on the right.

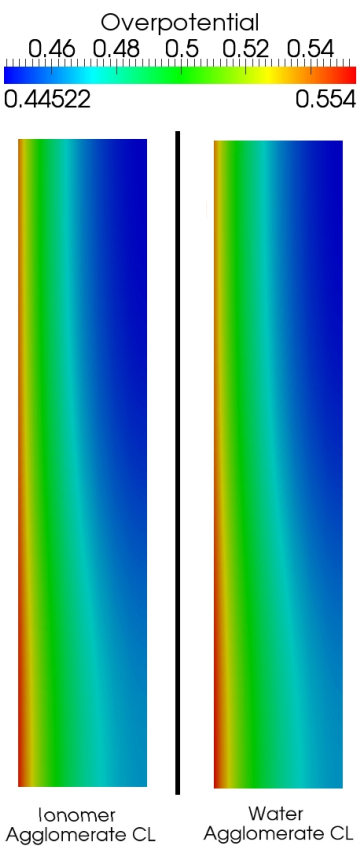

(a) Overpotential distribution within the CCL for ionomer- and water-filled agglomerates.

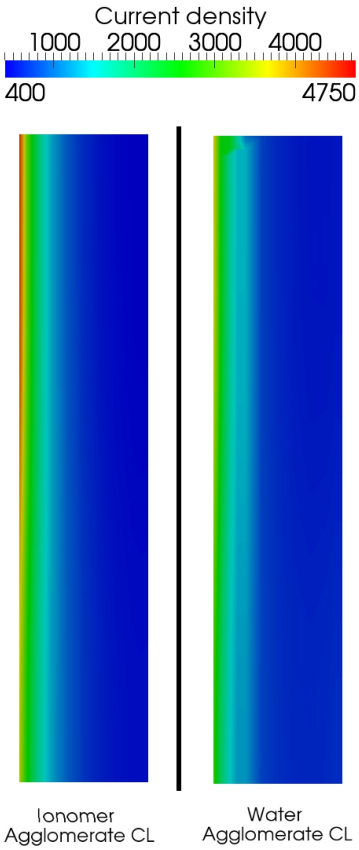

(b) Current density distribution within the CCL for ionomer- and water-filled agglomerates.

Figure 3.13: (a) Overpotential and (b) local current density profiles within the cathode catalyst layer at $1.05\,A/cm^2$. The CL thickness ($10\,\mu m$) has been enlarged 20X for clarity. The catalyst layer with ionomer-filled agglomerates is shown on the left and the water-filled agglomerates on the right.

and structural. The scope of this work did not allow for a comprehensive parameter study to compare the water- and ionomer-filled agglomerate models and how they behave in the MEA. Results for the multiscale water-filled agglomerate model are computationally expensive and difficult to obtain for a wide range of operating conditions. Though the results are only valid for this single set of parameters, it is concluded that the two models do not differ significantly in their trends and predictive capabilities.

Chapter 4

Catalyst Layer Parameter Estimation

4.1 Introduction

The objective of parameter estimation is to minimize modeling error by systematically obtaining values for unknown or uncertain parameters by matching model and experimental data. In the case of nonlinear models, linear regression analysis does not suffice for characterizing a set of model parameters. It is necessary in that case to use a nonlinear optimization-based method. Least-squares methods have a characteristic formula that does not differ based on the choice of model, therefore, a number of optimization methods and algorithms exist that take advantage of the known structure. A generic least-squares optimization formulation is

$$\begin{array}{ll} \text{minimize:} & \frac{1}{2}\sum_{i=1}^{n}\left[r_i\left(\vec{x}\right)\right]^2 \\ \text{w.r.t:} & \vec{x} \\ \text{s.t:} & x_j^{lb} \leq x_j \leq x_j^{ub} \end{array} \tag{4.1}$$

where r_i is the residual at point i between the model and experimental values, and x_j are the parameters to be estimated. In this case r_i is the difference in average current density of a cell a given cell voltage, over a range of operating conditions: temperature, pressure, and relative humidity.

4.2 Nonlinear Least-Squares Parameter Estimation

In this work, least-squares parameter estimation will be applied to the nonlinear PEMFC membrane electrode assembly model described in Chapter 3. A numerical framework has been developed within the Fuel Cell Simulation Toolbox (FCST) that allows for fuel cell modeling and optimization. The framework will be briefly

discussed in section 4.2.2.1, but first the least-squares optimization problem must be developed.

4.2.1 Problem Formulation

The FCST framework allows parameter estimation to be applied to any set of variables in the model; the focus of this study is to characterize the structure of the cathode catalyst layer by estimating structural parameters of the agglomerates. It was previously shown that the ionomer-filled model does not significantly differ from the water-filled model, and therefore the analytical ionomer-filled agglomerate model will be used in the MEA simulation. It should be noted that the framework allows for any model to be used for parameter estimation or optimization. The water-filled agglomerate model could be used with these methods, but the simulations to be described below would take months rather than weeks to complete. The objective of this study is to determine the radius (r_{agg}), porosity(ϵ_{agg}), and active area of platinum (A_v) of an ionomer-filled agglomerate in the catalyst layers of a PEMFC. The problem is formulated as:

$$\begin{array}{ll} \text{minimize:} & \frac{1}{2}\sum_{i=1}^{n}\left[I_i^{exp} - I_i^{model}\left(\vec{x}\right)\right]^2 \\ \text{w.r.t:} & \vec{x} = r_{agg}, \epsilon_{agg}, A_v \\ \text{s.t:} & 15nm < r_{agg} < 250nm \\ & 0.05 < \epsilon_{agg} < 0.45 \\ & 8.0 \times 10^3 < A_v < 4.0 \times 10^6 \end{array} \tag{4.2}$$

The variables are bounded to prevent divergence and testing of infeasible values. These bounds are based on predictions on the range of uncertainty of each variable based on previous values reported in the literature. The first two parameters in the formula can be used to fully characterize the catalyst layer. First, the radius of the agglomerate, r_{agg}, and the porosity, ϵ_{agg}, are selected independently. The equations developed by Secanell et al. [33] relating the volume fractions to the agglomerate structure are then used to determine the thickness of the electrolyte film surrounding the agglomerate (see section 3.2.3). These parameters are all determined assuming that the composition of the catalyst layer, i.e. the platinum loading, the fraction of Platinum on Carbon support particles, and the electrolyte loading in fabrication, determines the volume fraction of electrolyte and pores, and that these volume fractions are independent of the microstructure and operating conditions. These parameters are set in both the anode and cathode since the cells in question are

fabricated with identical catalyst layers. The last parameter is the active area of platinum catalyst, A_v, at the cathode. The active area in the anode is held constant since the kinetics are fast. The upper and lower bounds of this variable corresponds approximately to the range of uncertainty in the reference exchange current density since they are related by the Tafel equation. Therefore, these three parameters fully characterize the microstructure and kinetics of the catalyst layer.

To determine the quality of fit, the root mean square of the residuals is evaluated across all data points.

$$F(\vec{x}) = \sqrt{\frac{1}{N}\sum_{i=1}^{n}\left[I_i^{exp} - I_i^{model}(\vec{x})\right]^2} \tag{4.3}$$

This measure allows the quality of fit to be determined independently of the number of points in the data set. A low quality of fit is indicated with a high value of F, while $F = 0$ is the result for a perfect fit.

4.2.2 Solution Method

4.2.2.1 Optimization Interface Framework

The least-squares parameter estimation problem is solved by coupling the fuel cell analysis code - the Fuel Cell Simulation Toolbox (FCST) - to the optimization package DAKOTA [93]. The interface is designed so that analysis package has access to select optimization strategies and options directly from DAKOTA, without the use of input files. Conversely, DAKOTA's packages have access to manipulate variables in the analysis code, and are able to get solutions and gradient calculations (if available) for each function evaluation. This clean, seamless integration of the two software packages allows for better data management, simplified user controls, and a faster interface for large scale optimization problems. A schematic of the program is shown in Figure 4.1. Note that this method of coupling the analysis and optimization algorithms will not be as efficient as those that directly couple model equations with the optimization algorithm like Carnes and Djilali [58], but is more versatile in its ability to change models, optimization algorithms and program options.

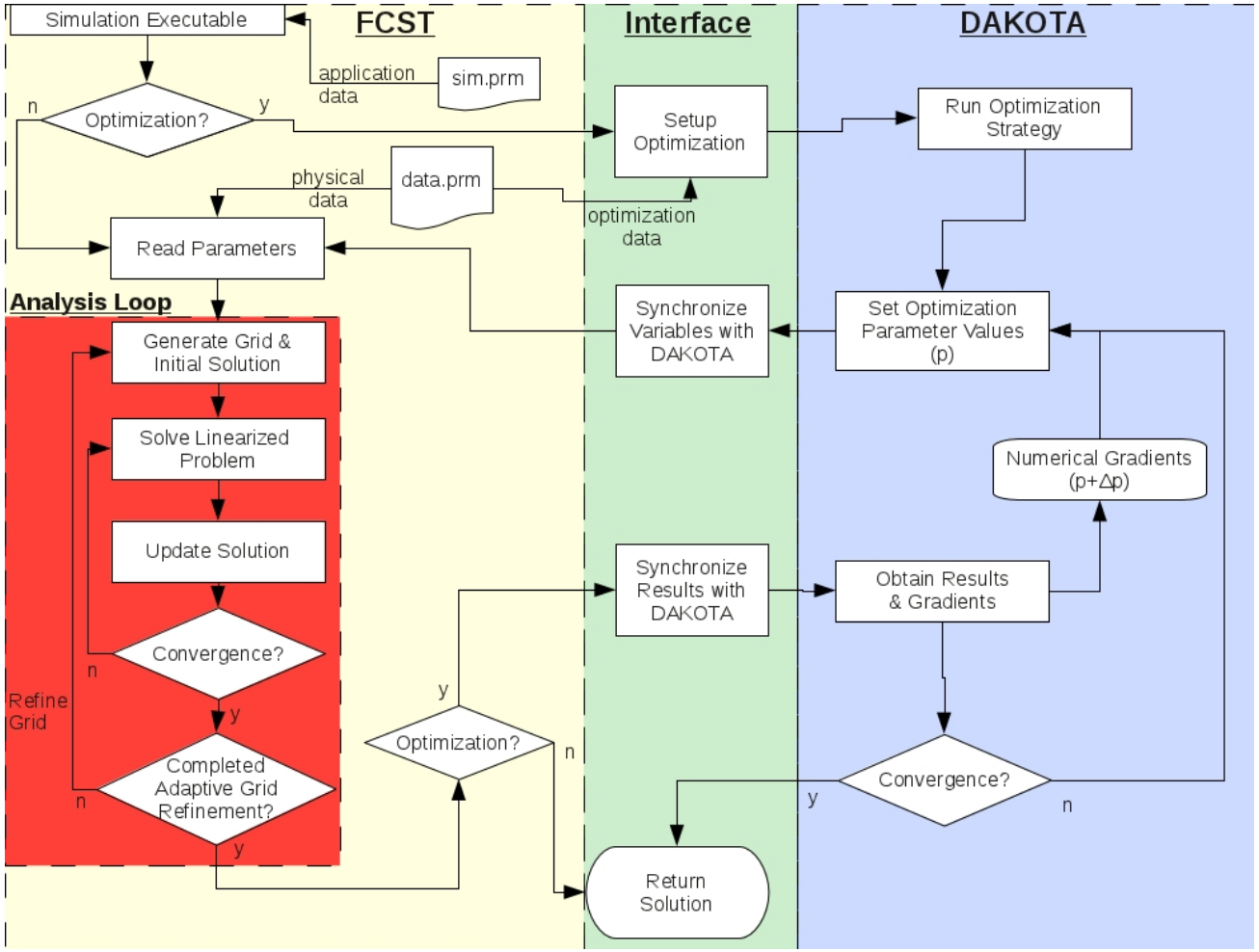

Figure 4.1: Schematic of the fuel cell analysis code and DAKOTA Optimization interface

Similar to the optimization formulation presented by Secanell [11], the solution to a fuel cell optimization or parameter estimation problem is obtained through a number of iterative loops. The analysis loop shown in Figure 4.1 solves the governing equations for a given mesh using an integrated Newton solver, while an adaptive mesh refinement loop ensures that the solution is grid independent[1]. The solution or objective function is evaluated by the analysis code and returned to DAKOTA. Gradients, if required, can be obtained either analytically or numerically through finite differencing for each parameter. Convergence of the optimization algorithm is controlled by the change in the objective function, the relative change in the design variables, or the total number of iterations.

There are two types of optimization algorithms that can be used for optimization: gradient-based, and non-gradient-based. The gradient based methods exhibit faster convergence than non-gradient-based, but are typically local methods, and therefore the final solution is dependent on the starting point. Non-gradient-based methods are generally global methods, where the entire parameter range is tested. For the least-squared problem presented here, three algorithms were tested in order to ensure a reliable solution, two gradient-based methods and a global method. The first is a gradient-based algorithm specific to least-squares problems; the last two are generic global and local methods that can work for any model and objective function.

An algorithm specifically tailored to nonlinear least-squares parameter estimation, NL2SOL [94], was used from DAKOTA's optimization libraries [93]. The algorithm is an adaptive secant-based method that periodically uses a first-order approximation of the Hessian matrix to determine the solution direction and step size. Solutions are obtained for each point on the experimental polarization curve before the residuals, r_i, are evaluated and returned to the optimization loop. The algorithm evaluates the gradients and uses the sensitivity around every data point to construct the Hessian approximation. It has been shown to exhibit faster convergence than the Gauss-Newton method and Maquardt method for problems with a residual that does not tend to zero. The choice here is appropriate, as the problem being considered samples fuel cell data from a large range of operating conditions. Data points predicted by a model may not necessarily tend to the experimental data at the solution for all operating conditions. In works previously published by the author [92], the NL2SOL algorithm was used in this exact manner to obtain a local

[1]This is identical to the method presented in Chapter 3

optimal solution.

In order to ensure that the final solution is valid, a global method that tests the parameters across their full range must be used. Multi-start methods can be used with gradient based methods to tests the solution obtained from different start points. A multi-start strategy with the NL2SOL algorithm is generally accurate and robust, but for the set of parameters and the uncertainty range being investigated, the algorithm was determined to be unsuitable. It was found that the gradient approximation near the variable bounds (specifically small r_{agg}, ϵ_{agg}, and low A_v), were inaccurate and would not lead to a global minimum. The gradient approximation was changed to a second-order method (central-differencing), and a step-size study gave good precision in the gradient approximation, but not the accuracy required. Central differencing also requires two extra function evaluations per variable to obtain a gradient approximation. This leads to long computational times on a similar scale to global methods.

Based on the inconclusive preliminary results by the NL2SOL algorithm, a hybrid sequential multi-strategy optimization formulation was developed [93]. The strategy employed a global method to obtain an approximation of a solution, where a local gradient-based method then takes over to find an exact solution to a lower level of convergence.

The global method chosen for this application is the dividing rectangles method, specifically an enhanced method developed at North Carolina State University called NCSU-Direct [95]. The parameter space forms a hypercube, and the method starts by evaluating the objective function at the center. It then obtains evaluations at equally spaced distances from the center towards the edges of the hypercube (i.e. $c \pm \delta$). The distance δ is defined as $1/3$ of the total edge distance of the cube. Based on an evaluation criteria, the cube is divided along one of the axis into rectangles. The algorithm then uses a measure based on an estimation of the function's Lipschitz constant to determine whether the rectangle is potentially optimal. The best rectangle is divided into cubes and the process is repeated starting with the cube having the smallest objective function. Figure 4.2 shows the process in 2 dimensions from the beginning. The advantages to using such a method is that gradient information is not required and global convergence is more likely. Other specific benefits to this algorithm exist, such as handling hidden constraints. As an example, if a solution does not exist or can not be obtained for a given set of parameters, the

analysis code will return NaN, or *Not a Number*. This algorithm recognizes that as a constraint and constructs a feasibility front, where nearby values are used in place of infeasible ones. Gradient based methods typically fail as soon as a solution cannot be obtained.

Once objective function (4.2) converges to a tolerance of 10^{-3} around its minimum through the NCSU algorithm, a local method takes over, using the global coarse solution as its starting point. The algorithm converges to 10^{-4} for added accuracy. The local method used is a simple quasi-Newton algorithm with a line-search to ensure reduction of the residual at every iteration. The algorithm can be found in the OPT++ library of optimization algorithms in DAKOTA [93]. Numerical gradients are obtained using a central differencing scheme, with a step size of $x_j \times 10^{-3}$, or a 0.1% change in the current value of the variable.

4.2.3 Experimental Setup

In order to estimate the agglomerate structure by parameter estimation as described above, the model must be compared to a set of experimental data. The National Research Council Canada - Institute for Fuel Cell Innovation (NRC-IFCI) has provided polarization curve data for this purpose. The following is a summary of their cell construction and testing process.

A 25cm^2 (5x5cm) catalyst coated membrane (CCM) and MPL was inserted between two SIGRALET 24BC GDLs and assembled into a single cell with straight flow-through channels. The catalyst layers have a platinum loading of 0.4mg/cm^2 and 30%wt Nafion loading. The single cell was evaluated in a fuel cell test station (100W, Scribner 850C, Scribner Associates, Inc.). H_2 (purity 99.99%) flow rates were held constant at 2 SLPM (Standard Litres Per Minute), while air flow rates were held constant at 5 SLPM. The high gas flow rates, equal to excess stoichiometries, were used to ensure that the gas supply to the catalyst layer was not limited by mass transport. The results presented in section 4.3 are for four polarization curves at 30%, 50%, and 70% relative humidity, 95℃, and at 1 and 2 atmospheres. The input parameters for the set of data is presented in Table 4.1 and the dimensions of the cell are listed in Table 4.2. Note that the dimensions are similar to those used in Chapter 3, as only the CL thickness has changed.

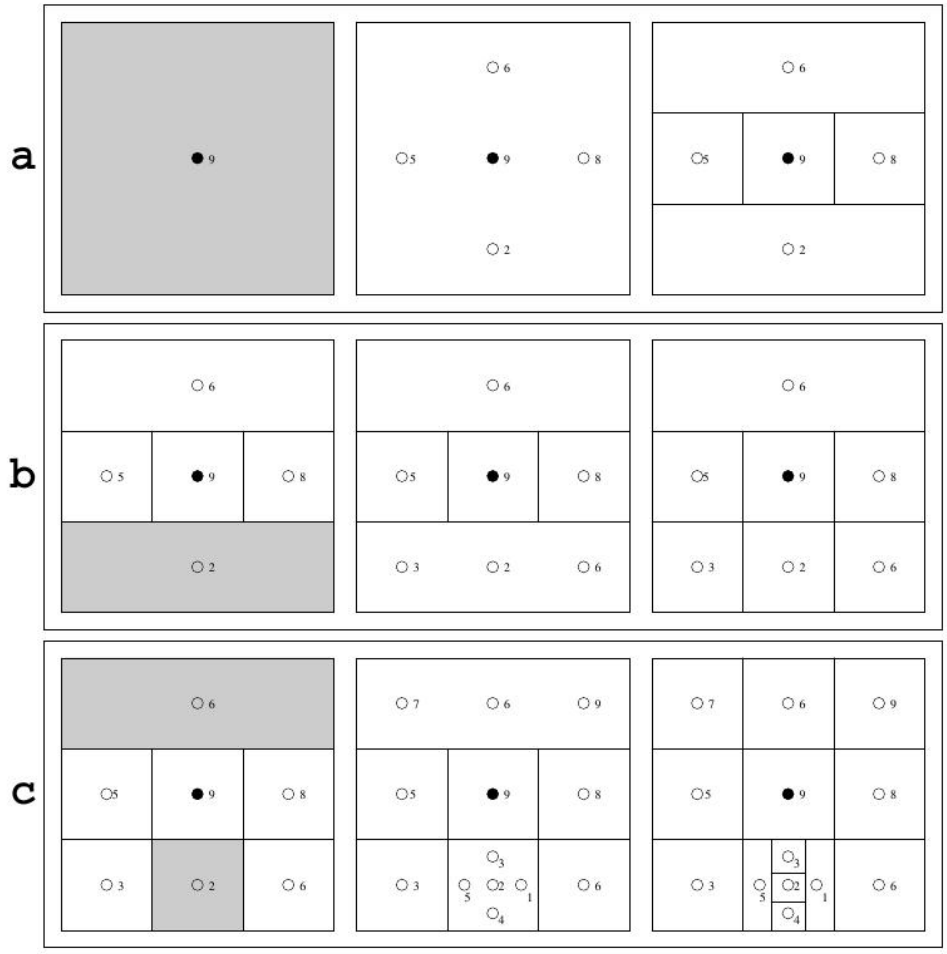

Figure 4.2: Schematic of the dividing rectangles (DIRECT) optimization algorithm from [95]. Row **a** shows the hypercube (square), and the division of the evaluation points. The value of the objective function is shown next to each point. Row **b** shows a shaded, potentially optimal rectangle, and its division in the subsequent columns. Row **c** then shows another potentially optimal rectangle being divided, and the best cube being divided (twice - identically to step **a**). The process repeats until the convergence criteria are met.

Table 4.1: Cell operating conditions

	Operating Conditions		
Data Curve	Temperature (K)	Pressure (atm)	Relative Humidity (%)
A	368	1	30
B	368	1	50
C	368	1	70
D	368	2	50

Table 4.2: Electrode geometry

Parameter	Value
Channel width, [cm]	0.1
Current collector width, [cm]	0.1
GDL thickness, L^{gdl}, [μm]	250
MPL thickness, L^{mpl}, [μm]	50
CL thickness, L^{cl}, [μm]	11
Membrane thickness, L^{m}, [μm]	25

4.3 Results and Discussion

Two sets of results were obtained and will be discussed in this section. Parameter estimation of an MEA with an ionomer-filled agglomerate microstructure was first conducted for a single curve, as is typically done by parametric studies in the literature. However, Springer [96] and Guo [59] suggested that estimating the model parameters simultaneously over a range of operating conditions gives a much better confidence in the results than estimating the parameters individually for each polarization curve. The second study presented in this section, therefore, is conducted using all four curves from Table 4.1.

Single Curve Fit - The MEA model was used to fit curve B from the data set. The curve fit is shown in Figure 4.3 and the results presented in Table 4.3.

From Figure 4.3 it is clear that the algorithm improves the quality of the fit over the initial solution at the center of the parameter space ($r_{agg} = 132.5\,nm$, $\epsilon_{agg} = 0.235$, $A_v = 3.9 \times 10^6$). The NCSU Direct algorithm is not a successive iterative process, therefore a convergence plot is not available. The algorithm evaluated the residual norm at 285 points across the parameter space to find one near the global minimum.[2] Final convergence was obtained through the Newton method in 1 iteration (14 function evaluations - 1 function evaluation followed by 12 evaluations for the gradient, and 1 final evaluation to check for convergence). The decrease in the active area brings the curve closer to the data in the kinetic region. The increase in the agglomerate radius and the decrease in porosity helps to increase some of the mass transport losses at high current densities. The most important result to note from Table 4.3, however, is that the agglomerate radius variable, r_{agg}, hit

[2]Note that the objective function to be minimized is the sum of the squares of the residual, given in equation (4.2). Therefore a single function evaluation is comprised of n solutions to the MEA model (where $n = 9$ for this case).

Table 4.3: Results from least-squares parameter estimation for a single curve fit

Parameter	Curve B
Agglomerate Radius (r_{agg}) [nm]	250
Agglomerate Porosity (ϵ_{agg}) [-]	0.169
CCL Active Area (A_v) [cm^2/cm^3]	1.7163×10^6
Quality of Fit ($F(x)$)	0.0314

its upper bound for size of 250 nm. This is one of the dangers of bound-constraint optimization. It means that a better solution can be obtained if the bound is relaxed, or unconstrained. This parameter is constrained so that the results are within the range of estimated particle sizes from microscopy studies in the literature [17, 39], which are typically in the $100 - 200\,nm$ diameter range. The model here predicts agglomerates of 500 nm in diameter, a significant increase over this estimated size. The remaining optimization becomes a trade-off in the other two variables and may not accurately represent the structure or kinetics of the agglomerate.

The active area of platinum is fit to a high value (nearly an order of magnitude higher than measured experimentally) to try to match the shape of the curve. The result, however, is that in the kinetic region the model over-predicts the performance of the cell. In the ohmic region, the data is fit quite well by a straight line, although the data seems to indicate some curvature. The agglomerate porosity converges to a low value of approximately 17% in order to fit the higher end of the curve where mass transport resistance is starting to have an effect. Across the entire range of the data, the model does not differ from the experiments by more than 55 mA, indicating a good quality of fit. However, it is expected that for fitting only one curve, the data points could be fit nearly exactly ($10 - 20\,mA$); the quality of the fit is not as high as expected.

The quality of the results cannot be discussed without mentioning the potential sources of error. There are uncertain parameters in the agglomerate, such as the oxygen diffusion coefficient in Nafion, $D_{O_2,N}$, which heavily influence the solution. Chapter 2 showed that the agglomerate model will give very different results based on the choice of parameters. Parameters such as oxygen diffusion through Nafion are plagued with uncertainty, and can vary up to an order of magnitude in different publications [70, 71]. Previous studies performed as a precursor to this work with the agglomerate model previously used by Secanell et al. [11, 33, 54] have indicated that decreasing the oxygen diffusion coefficient decreases the size of the radius predicted

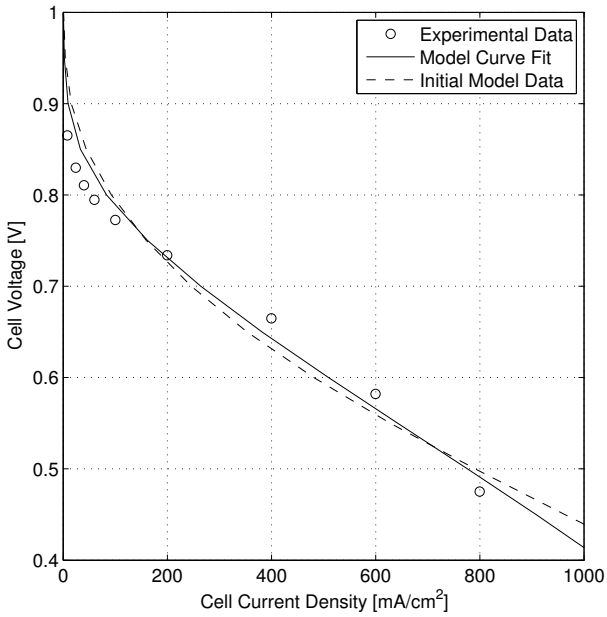

Figure 4.3: Single curve fit from least-squares parameter estimation

by parameter estimation [97, 98]. As the agglomerate models are similar, the results are likely to apply to this model as well. However, the decreased radius indicated in the results had no substantial effect on increasing the overall quality of fit. The model showed improved accuracy with the data at some operating conditions while the quality of fit at some operating conditions deteriorated. These studies were a good indication that the oxygen diffusion in Nafion is critical in determining the performance of a cell and a good approximation of the diffusion coefficient should be used in models. Unfortunately, in-situ measurements have not been reported in the literature, so results from testing with a Nafion membrane sample must be used. The estimated value will depend heavily on the method of preparation of the sample, and vastly different results can be obtained. Since the goal of this study is to characterize the structure of the agglomerate, uncertainty in all other parameters should be minimized. That task, however, is difficult to accomplish.

These sources of uncertainty make it possible that the results are skewed. The current density given by the agglomerates was shown in Chapter 3 to have coupled effects on the performance of the MEA model. These coupled effects make diagnosing the source of error extremely difficult. Furthermore, the presence of agglomerates in the CL cannot be confirmed experimentally, nor can many of the effects can be

measured. This is why some researchers call into question the agglomerate concept altogether. The modeled structure may be an oversimplification and idealization of the real structure of a catalyst layer and characterization of its exact size in relation to images may not be a useful measure. It may be more beneficial to define the size of an idealized agglomerate, as long as the model is a good predictor of cell performance. Bounded parameter estimation in that case would not be the most appropriate choice. It would also be a requirement to make it clear to modelers that the agglomerate is simply a tool to predict cell performance.

The experimental sources of error cannot be ignored either. There are inexact parameters from experimental measurement being used in the model, such as the catalyst layer thickness and porosity. As shown in Chapter 3, the porosity alone can affect the current density predicted by the model, especially when the conditions come near the onset of mass transport limitations. The data may also have some inconsistencies, as the repeatability of the the experiments is unknown. For the gathered data, it is not known how the results change for reproducing the experiments with the same cell, or reproducing the experiments from the fabrication stage. Such results would give a better indication of the variability in some of the parameters, and help determine the actual quality of the fit for parameter estimation.

Multiple Curve Fit - The agglomerate model is meant to characterize the behavior of a PEMFC over a wide range of operating conditions. It has just been demonstrated that the model can do so for a single operating condition, albeit to a marginally lower level of accuracy than expected. If agglomerates exist in the catalyst layer, they will be a product of the fabrication technique, not the conditions for which the cell is being run. Therefore, agglomerate parameters should be valid over a range of operating conditions to characterize the structure. It is expected that the quality of fit will deteriorate slightly, but that the trends will be captured by the model.

With this larger set of data, both the NL2SOL algorithm and the hybrid optimization method used previously were tested to ensure consistency. The hybrid optimization strategy was found to reduce the residual beyond the result from NL2SOL. The radius and porosity of the agglomerate settle at the same value for both algorithms, but the NL2SOL algorithm predicts an active area of nearly half of that predicted by the NCSU Direct algorithm. This is due to the sensitivity of the active

area on the solution and the inability of the numerical differencing scheme to resolve the gradients. Using a non-gradient based global method to get very close to the solution and proceeding with a local method is more robust than a gradient-based method. The trade-off for the global method is time. The NCSU Direct algorithm performed 849 function evaluations before switching to the local method, which performed a further 111 evaluations (including gradient evaluations) in order to arrive at a solution. This is in comparison to 62 evaluations by using NL2SOL as a single gradient-based method (note that multi-start methods would increase the number of required evaluations).

The final results for the fitting parameters at the global minimum are presented in Table 4.4. The agglomerate radius again tends its upper bound of $250\,nm$. This leads to a similar case to the single curve fit where the active area is increased to twice that of the single curve fit in order to match the data in the ohmic region. The agglomerate porosity is then reduced to approximately 12% to capture mass transport effects. Note that these results are very similar to those obtained for the single curve fit. This is a good indication that the agglomerate model with these parameters helps to fit the trends of the polarization curves, despite that the results are not necessarily an indication of the microstructure. Model trends can be seen in Figure 4.4, where all the curves are plotted over the whole range of current densities. To discuss the data in the kinetic region, Figure 4.5 shows a closeup of the curves up to $250\,mA/cm^2$.

Although the kinetics predict smaller losses, the trends are captured by the model. It can be seen that at very low current densities (below $100\,mA/cm^2$) the data indicates better performance of the cell at lower humidity. Within the kinetic range, a crossover occurs, where higher relative humidity leads to better performance. At very low current, membrane hydration will not play a significant role. The small increase in performance at low humidity levels comes from the higher concentration of oxygen and lower concentrations of water vapour in the inlet stream. As more current is drawn, ohmic effects become more significant. For the curves at 1atm there is first a crossover between the 30%RH curve and the 50%RH curve, and the 30%RH curve and the 70%RH curve near the same current of $60 mA/cm^2$ and finally the 50%RH curve and the 70%RH curve cross over around $100\,mA/cm^2$. These trends are followed by the model, but they occur much earlier in the curve (near $5-10\,mA/cm^2$) and are not as pronounced due to much faster

Table 4.4: Results from least-squares parameter estimation for fitting multiple curves

Parameter	All Curves
Agglomerate Radius (r_{agg}) [nm]	250
Agglomerate Porosity (ϵ_{agg}) [-]	0.116
CCL Active Area (A_v) $[cm^2/cm^3]$	3.5706×10^6
Quality of Fit ($F(x)$)	0.0529

reaction kinetics.

In the $400 - 800\, mA/cm^2$ region, shown in Figure 4.4, the trends are not captured for all the curves. The model can predict the performance at low humidity levels; the 30%RH and 50%RH curves are fit very well. At 70%RH, the experimental data indicates much better performance over the 50%RH case, likely due to a well hydrated membrane and high proton conductivity through the membrane and catalyst layers. At higher current densities there is a notable drop in performance beyond the typical ohmic losses. The model is not able to simulate either effect, using a constant slope to fit the data, with only a marginal performance increase over the 50%RH case.

The higher pressure case of 2atm and 50%RH on the inlet streams shows similar trends to the 1atm, 50%RH case. The kinetic losses are much smaller than measured, while the ohmic losses are slightly exaggerated. The data is fit by a constant slope, and at higher current densities the onset of mass transport losses is not able to be captured by the model. As expected, the overall quality of fit is not as good as the single curve, as indicated by the higher value of $F(x)$ in Table 4.4. Table 4.5 breaks down the quality of fit measure by curve. This shows that the model is best able to fit the data at 30%RH, and has difficulty with the case at 70%RH. The quality of fit for the cases at 50%RH are good, and the values between 1 and 2atm pressure are similar, showing that the fit quality is independent of pressure. Therefore, the model gives a good fit of all the data over the operating ranges, and can accurately capture the trends of increased pressure, but not of increasing relative humidity.

The results from this study show that the behavior of a PEMFC can be approximated, but not completely characterized by a steady-state, single phase, isothermal model with a catalyst layer agglomerate model. The agglomerate model helps capture some of the transport losses at medium and high current densities, making it a useful modeling tool. It cannot, however, completely characterize the structure of

Table 4.5: Quality of fit parameter by experimental curve

Curve	Quality of Fit ($F(\vec{x})$)
A	0.0324
B	0.0536
C	0.0610
D	0.0589
Overall	0.0529

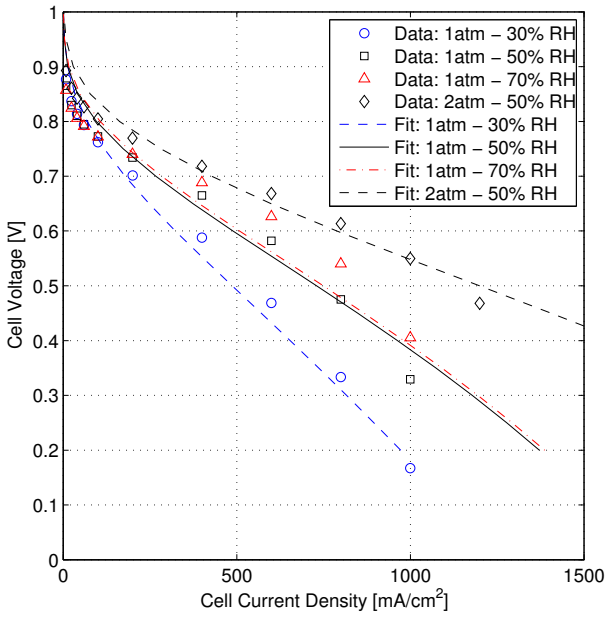

Figure 4.4: Multiple curve fit from least-squares parameter estimation

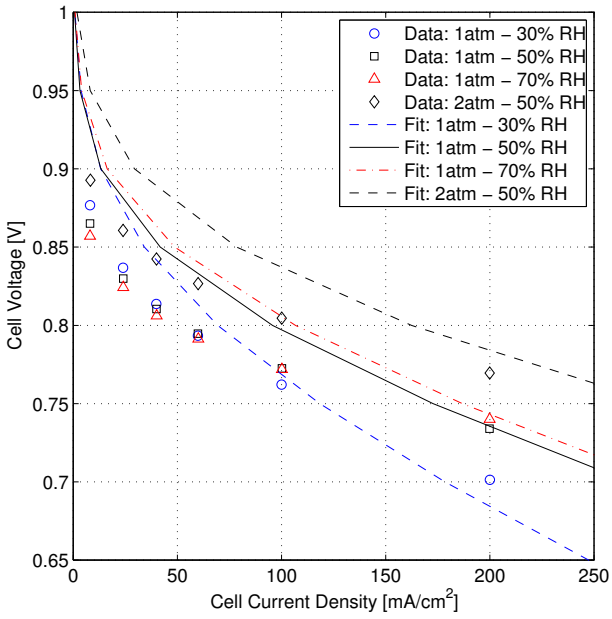

Figure 4.5: Kinetic region of multiple curve fit from least-squares parameter estimation

the catalyst layer and capture the trends across all operating conditions. It is evident that there are physical phenomena at work that are not being modeled. Those effects could be from temperature, two-phase flow, or three-dimensional phenomena, but the agglomerate model alone can not - and should not - be used to completely describe all of the mass transport losses. In this work, the source of error has not been pinpointed, whether it be experimental or modeling, and further studies with expanded data sets should be (and will be) performed. It should also be noted that despite the countless models that exist within the literature, this author has not found one that can demonstrate it characterizes PEMFC performance over a wide range of operating conditions. The objective of any model is to be able to do so; the work in this chapter described the development of a tool for estimating parameters within models of ever expanding complexity.

The complexity added by the water-filled agglomerate model developed in this work may help capture the trends and better characterize the structure of the catalyst layer. Specifically, the results from Chapter 3 showed increased performance in the ohmic region and higher mass transport losses towards 1 A/cm^2, which better characterizes this particular set of data. The scope of this work, however, did not allow for a full investigation of the water-filled agglomerate by parameter estima-

tion. Simulation times for the above optimization studies are measured in weeks due to the incredible amount of function evaluations required to obtain a solution. This timescale is for an MEA model that can be solved, on average, in less than a minute. An MEA model with a water-filled agglomerate in the cathode alone can take up to 57 hours to compute. Parameter estimation in this case is prohibitive.

Chapter 5

Conclusions and Outlook

5.1 Conclusions

The objective of this work was to be able to describe the catalyst layer with more detailed agglomerate models and characterize its microstructure by parameter estimation. To this end, agglomerate models in the literature were studied and two enhanced agglomerate models - an ionomer-filled and a water-filled model - were developed for use in a cathode catalyst layer model. A model by Secanell [54] of a 2D across-the-channel PEMFC membrane electrode assembly was enhanced and expanded by integrating the agglomerate models as a multiscale simulation. Lastly, nonlinear least-squares parameter estimation was performed with the MEA model to characterize the structure of the agglomerates using a framework developed specifically for fuel cell design and optimization.

There is conflicting discussion in the literature about the structure of the catalyst layer, the presence of agglomerates, and how they should be modeled. This work assumed that the catalyst layer can be modeled with a spherical agglomerate and looked explicitly at how two different assumptions affect the current density predictions. A water-filled model and an ionomer-filled agglomerate model with ionomer thin-films were developed to simulate cathode kinetics and mass transport effects at the nanoscale. The water-filled model provides the first example in the literature where the thin film is directly modeled and shown to have an effect on the results. A comparison of the two models showed that they produce the same current at low overpotentials (up to $\eta_c = 0.4\,V$) in the cathode due to adequate transport of oxygen through the agglomerate. In the ohmic region, at overpotentials above $0.4\,V$ and into the mass transport region up to overpotential of $0.9\,V$, the water-filled agglomerate outperforms ionomer-filled agglomerate. This is due to

increased oxygen transport but also from higher induced overpotentials from charge transport limitations inside the agglomerate. At overpotentials above $0.9\,V$ - an extremely unlikely condition in a cell - the two models again do not differ because all available oxygen is consumed at the surface of the agglomerate.

This study also took a first look at the behavior of a water-filled agglomerate under a half-order oxygen reaction. The reaction rate was shown to significantly increase over the first-order reaction, up to a full order of magnitude. The trends over the range of overpotentials, however, are very similar. The study shows that the behavior of the reaction and oxygen diffusion inside the agglomerate is very irregular, very nonlinear. This provides an interesting case for further analysis, but also is a challenging numerical problem and results could only be obtained for a limiting number of conditions.

The purpose of an agglomerate model is to be able to predict the current density in a catalyst layer. A standalone model is therefore only useful for nanoscale analysis of transport and kinetics. This work expanded on a multi-dimensional MEA simulation, originally developed by Secanell [54], to present the first instance of a state-of-the-art multiscale agglomerate model. The study also emphasized the inextricable link between the volume fractions of materials in the catalyst layer and the agglomerate structure. Assuming that a water-filled agglomerate exists in the catalyst layer leads to a reduced porosity since ionomer is displaced from the primary pores. This phenomenon was shown to have an effect on the distribution of reactants within the catalyst layer. Despite this difference, the cell current densities given by the MEA model do not differ significantly based on the choice of agglomerate. This result, however, is only confirmed for a single performance curve at one set of operating conditions. At up to 57 hours for a single data point, the MEA model with a water-filled agglomerate in the cathode requires the most computational resources; at this time scale extensive and detailed analysis becomes prohibitive. This long computational time comes even after several measures were implemented to reduce the computational cost. The short analysis, therefore, failed to help characterize the structure of the catalyst layer. It did, however, illustrate that the ionomer-filled model does not significantly differ from the water-filled model, and is useful in predicting PEMFC trends and characterizing the CL microstructure.

Finally, nonlinear least-squares parameter estimation was used in an attempt to characterize the structure of the agglomerates in the catalyst layer. For this

purpose, a tool was developed as an extension of the Fuel Cell Simulation Toolbox that directly links the optimization program DAKOTA to the fuel cell analysis code, opening up the full array of optimization options provided by DAKOTA while increasing the efficiency with seamless data handling between the two programs. The optimization-based parameter estimation method was demonstrated to work with a single curve and a set of curves at multiple operating conditions. Two methods were tested to ensure that a global minimum was obtained over the parameter space. In the end, a hybrid method using a non-gradient based algorithm (DIRECT) that switched to a local quasi-Newton method was more reliable than using a multi-start strategy with a specific method tailored to least-squares optimization. The results, however, showed that the current agglomerate-based model was unable to accurately characterize the agglomerate structure, as the algorithm predicted that an agglomerate radius at or above the realistic bounds best matches the data. The trends in the experimental data could also only be followed for certain operating conditions. The tool was extensively tested as demonstrated in the literature and through internal technical reports. Through all of these efforts, the exact source of error could not be pinpointed. The model was consistently improved with little effect on the results. Therefore, the experiments must have physical phenomena occurring within the cell that are not being modeled, or some inconsistencies exist within the data.

In summary, the catalyst layer microstructure of a polymer electrolyte membrane fuel cell was investigated through modeling studies looking at three aspects. First, the performance of different types of agglomerates was compared using enhanced models that are the first of their kind in the literature. These models were integrated into an MEA model to analyze their impact on catalyst layer performance. Lastly, an attempt was made to characterize the microstructure of the catalyst layer by parameter estimation. A robust tool and method was developed and successfully implemented, but the results from this particular set of data failed to characterize the structure of the layer. The studies and analysis performed in this work have created a platform for development and further study, which holds promise for computational PEMFC analysis and computational design.

5.2 Outlook

Over the course of this work, several novel models were developed for PEM fuel cell and catalyst layer analysis. The studies within looked at the broader aspects of model performance. Further work is needed to test and develop each of the models for validation and greater understanding.

The water- and ionomer-filled agglomerate models were shown to be similar at low and high current densities and only differ in the ohmic region. Agglomerate models are expected to introduce higher mass transport limitations and decrease catalyst utilization. While some of these effects can be seen, neither model is able to predict the steep drop in performance at high current densities seen in experimental data. This could be due to a variety of different effects from mass transport, to kinetics, to anisotropy of the structure. More comprehensive studies can be performed with critical parameters, specifically the oxygen diffusion coefficient and kinetic parameters. If oxygen diffusion is shown to be more limiting than simulated in this study, the agglomerates may give very different performance curves. The kinetics may also introduce different trends. A half-order reaction order with respect to oxygen was briefly investigated, but different reaction orders may better characterize the reaction. There is also not a firm consensus on the transfer coefficient, which has a profound impact on model behavior. The developed code also allows for completely different reaction kinetics to be simulated; the model is not constrained by Butler-Volmer kinetics and therefore a dual-path kinetic model, for example, could be used to describe the reaction in the agglomerate core. The last improvement to the agglomerate model would be to move to three dimensions. The assumptions made in this and all agglomerate models is that there is spherical symmetry. The unstructured nature of the catalyst layer means that there is likely anisotropic effects from uneven distributions of ionomer thin films and oddly shaped agglomerates.

The multiscale implementation of the agglomerate model shown in this work also leaves room for further study and development. The first step is to improve on the speed and robustness of the numerical code. The time required to solve an MEA model with a water-filled agglomerate model is prohibitive for comprehensive and detailed analysis. It is proposed that the agglomerate models be substituted with surrogate models for the bulk of the computations, or that a detailed parameter

map is developed for each agglomerate in order to improve the speed of access to the current density data. Once this is accomplished, the MEA model can be further studied with respect to changes in the reaction kinetics, transport properties, and agglomerate structure. This will allow for the electrodes to be better understood, characterized, and eventually custom designed.

The final component for this study was the parameter estimation and optimization framework. This is where much of the opportunity for future work lies. The framework is a tool developed for computational analysis and optimization of fuel cells, based on the methods used by Secanell [54]. The direct coupling of the optimization software to the analysis code provides countless opportunities and makes it a very versatile and powerful computational tool. It has been shown that there is a lack of parameter estimation or characterization studies performed with respect to fuel cells. This deficiency is not only for characterization of the CL microstructure, but determination of any set of parameters and their coupled effects on the model. It is suggested that for any model with a set of parameters with an unreasonable range of uncertainty be tested and characterized by parameter estimation. However, the model must first be validated - the usefulness of the tool is dependent on the model and data provided.

The model here was shown to match experimental data well at some operating conditions, but lack predictive capability at others. It is evident that at some conditions there is not sufficient detail and complexity in the model to predict cell performance. All models are simplifications of reality and physical processes, so it is likely that the model here does not capture all of the physical phenomena occurring within a cell. There are many suggested improvements for modeling. The area with much active research is two-phase flow modeling. Saturation and flooding of the cell can lead to significant mass transport limitations and decreased performance of the cell at high current densities, which is thought to better describe experimental trends. Modeling this behavior, however, is complex and very difficult to verify experimentally. The model presented here also does not include energy balances and is assumed to be isothermal. Heat rejection from the cell is also only a more prominent issue at higher current densities, and this approximation likely contributes to the discrepancy between model and experimental data. Lastly, the conditions throughout the cell are not completely uniform; the model here captures only 2-dimensional effects. The along-the-channel effects that this model ignores

should be directly simulated. The drawback to enhancing the model is the time requirements of optimization methods and the strain that added model complexity puts on the simulation. The benefit to this optimization framework, however, is that it is model independent; parameter estimation and optimization can be performed for any model with any level of complexity.

The analysis code and optimization routines used in this work have been shown to be accurate and faster than commercially available software [54], but for smaller scale simulations. The computing resources necessary for large scale simulations and larger optimization problems are too great for a single processor or small multi-processor machine. The final suggestion for improvement of the framework is massive parallelization of the code. This can be accomplished at several different levels. At the highest level, the optimization code can be run in parallel. This includes asynchronous evaluations of independent function evaluations, but also concurrent optimization iterator tasks. The next level is at the analysis code. FCST is capable of parallel computing to run a simulation. It is possible to segment a grid into subdomains and solve the entire problem in parallel. Similarly, a very large global matrix can be solved using a parallel linear algebra package such as those available in the Trilinos Project, integrated into deal.II [82]. All of these enhancements and possibilities open a pathway for fuel cell development, enhancing analysis and design through numerical simulation.

Bibliography

[1] M. Secanell, J. Wishart, P. Dobson, Computational design and optimization of fuel cells and fuel cell systems: A review, Journal of Power Sources 196 (8) (2011) 3690–3704.

[2] S. Rao, Y. Xing, Simulation of nanostructured electrodes for polymer electrolyte membrane fuel cells, Journal of Power Sources 185 (2) (2008) 1094–1100.

[3] R. O'Hayre, S.-W. Cha, W. Colella, F. Prinz, Fuel Cell Fundamentals, 2nd Edition, John Wiley & Sons Inc., New York, 2009.

[4] W. Sun, B. A. Peppley, K. Karan, An improved two-dimensional agglomerate cathode model to study the influence of catalyst layer structural parameters, Electrochimica Acta 50 (16-17) (2005) 3347–3358.

[5] S. Walch, A. Dhanda, M. Aryanpour, H. Pitsch, Mechanism of Molecular Oxygen Reduction at the Cathode of a PEM Fuel Cell: Non-Electrochemical Reactions on Catalytic Pt Particles, The Journal of Physical Chemistry C 112 (22) (2008) 8464–8475.

[6] Z. Shi, D. Song, H. Li, K. Fatih, Y. Tang, J. Zhang, Z. Wang, S. Wu, Z.-S. Liu, H. Wang, J. Zhang, A general model for air-side proton exchange membrane fuel cell contamination, Journal of Power Sources 186 (2) (2009) 435–445.

[7] Q. Wang, M. Eikerling, D. Song, Z. Liu, Structure and performance of different types of agglomerates in cathode catalyst layers in PEM fuel cells, Journal of Electroanalytical Chemistry 573 (2004) 61–69.

[8] Q. Wang, M. Eikerling, D. Song, S. Liu, Modeling of ultrathin two-phase catalyst layers in pefcs, Journal of the Electrochemical Society 154 (6) (2007) F95–F101.

[9] D. Harvey, J. Pharoah, K. Karan, A comparison of different approaches to modelling the pemfc catalyst layer, Journal of Power Sources 179 (1) (2008) 209–219.

[10] B. Andreaus, M. Eikerling, Catalyst layer operation in pem fuel cells: From structural pictures to tractable models, in: K. Promislow, S. Paddison (Eds.), Device and Materials Modeling in PEM Fuel Cells, Topics in Applied Physics 113, Vol. 41, Springer, 2009.

[11] M. Secanell, R. Songprakorp, N. Djilali, A. Suleman, Optimization of a proton exchange membrane fuel cell membrane electrode assembly, Structural and Multidisciplinary Optimization 40 (1-6) (2010) 563–583.

[12] A. Parthasarathy, S. Srinivasan, A. J. Appleby, C. Martin, Pressure dependence of the oxygen reduction reaction at the platinum microelectrode/nafion interface: Electrode kinetics and mass transport, Journal of the Electrochemical Society 139 (9) (1992) 2530–2537.

[13] A. Parthasarathy, S. Srinivasan, A. J. Appleby, C. Martin, Temperature dependence of the electrode kinetics of oxygen reduction at the platinum/nafion(r) interface - a microelectrode investigation, Journal of the Electrochemical Society 139 (9) (1992) 2530–2537.

[14] D. Sepa, V. M.V., D. A., Reaction intermediates as a controlling factor in the kinetics and mechanism of oxygen reduction at platinum electrodes, Electrochimica Acta 26 (6) (1981) 781–793.

[15] C.-Y. Wang, Fundamental models for fuel cell engineering, Chemical Reviews 104 (2004) 4727–4766.

[16] M. Grujicic, C. Zhao, K. Chittajallu, J. Ochterbeck, Cathode and interdigitated air distributor geometry optimization in polymer electrolyte membrane (PEM) fuel cells, Materials Science and Engineering B 108 (2004) 241–252.

[17] S. Thiele, R. Zengerle, C. Ziegler, Nano-morphology of a polymer electrolyte fuel cell catalyst layer-imaging, reconstruction and analysis, Nano Research (2011) 1–12.

[18] D. Bernardi, M. Verbrugge, Mathematical model of a gas diffusion electrode bonded to a polymer electrolyte, AIChE Journal 37 (8) (1991) 1151–1163.

[19] D. Bernardi, M. Verbrugge, Mathematical model of the solid-polymer-electrolyte fuel cell, Journal of the Electrochemical Society 139 (9) (1992) 2477–2491.

[20] C. Marr, X. Li, Composition and performance modelling of catalyst layer in a proton exchange membrane fuel cell, Journal of Power Sources 77 (1) (1999) 17–27.

[21] M. Eikerling, A. Kornyshev, Modelling the performance of the cathode catalyst layer of polymer electrolyte fuel cells, Journal of Electroanalytical Chemistry 453 (1-2) (1998) 89–106.

[22] D. Bevers, M. Wohr, K. Yasuda, K. Oguro, Simulation of a polymer electrolyte fuel cell electrode, Journal of Applied Electrochemistry 27 (11) (1997) 1254–1264.

[23] A. Kulikovsky, J. Divisek, A. Kornyshev, Modeling the cathode compartment of polymer electrolyte fuel cells: Dead and active reaction zones, Journal of the Electrochemical Society 146 (11) (1999) 3981–3991.

[24] L. You, H. Liu, A parametric study of the cathode catalyst layer of PEM fuel cells using a pseudo-homogeneous model, International Journal of Hydrogen Energy 26 (9) (2001) 991–999.

[25] Y. Rho, S. Srinivasan, Y. Kho, Mass transport phenomena in proton exchange membrane fuel cells using O2/He, O2/Ar, and O2/N2 mixtures. II. theoretical analysis, Journal of the Electrochemical Society 141 (8) (1994) 2089–2096.

[26] K. Broka, P. Ekdunge, Modelling the PEM fuel cell cathode, Journal of Applied Electrochemistry 27 (3) (1997) 281–289.

[27] F. Jaouen, G. Lindbergh, G. Sundholm, Investigation of mass-transport limitations in the solid polymer fuel cell cathode - I. Mathematical model, Journal of the Electrochemical Society 149 (4) (2002) A437–A447.

[28] J. Ihonen, F. Jaouen, G. Lindbergh, A. Lundblad, G. Sundhlom, Investigation of mass-transport limitations in the solid polymer fuel cell cathode - ii. experimental, Journal of the Electrochemical Society 149 (4) (2002) A448–A454.

[29] N. Siegel, M. Ellis, D. Nelson, M. Von Spakovsky, Single domain PEMFC model based on agglomerate catalyst geometry, Journal of Power Sources 115 (1) (2003) 81–89.

[30] K. More, R. Borup, K. Reeves, Identifying contributing degradation phenomena in pem fuel cell membrane electrode assemblies via electron microscopy, ECS Transactions 3 (1) (2006) 717–733.

[31] A. A. Shah, G. S. Kim, W.Gervais, A. Young, K. Promislow, J. Li, S. Ye, The effects of water and microstructure on the performance of polymer electrolyte fuel cells, Journal of Power Sources 160 (2006) 1251–1268.

[32] M. Eikerling, Water management in cathode catalyst layers of pem fuel cells, Journal of the Electrochemical Society 153 (3) (2006) E58–E70.

[33] M. Secanell, K. Karan, A. Suleman, N. Djilali, Multi-variable optimization of PEMFC cathodes using an agglomerate model, Electrochimica Acta 52 (22) (2007) 6318–6337.

[34] P. Jain, L. Biegler, M. Jhon, Sensitivity of pefc models to cathode layer microstructure, Journal of the Electrochemical Society 157 (8) (2010) B1222–B1229.

[35] Z. Xia, Q. Wang, M. Eikerling, Z. Liu, Effectiveness factor of pt utilization in cathode catalyst layer of polymer electrolyte fuel cells, Canadian Journal of Chemistry 86 (2008) 657–667.

[36] P.-C. Sui, L.-D. Chen, J. P. Seaba, Y. Wariishi, Modeling and optimization of a PEMFC catalyst layer, in: SAE SP-1425, Fuel Cell for Transportation, SAE, 1999, 1999-01-0539.

[37] D. Gerteisen, T. Heilmann, C. Ziegler, Modeling the phenomena of dehydration and flooding of a polymer electrolyte membrane fuel cell, Journal of Power Sources 187 (2009) 165–181.

[38] P. Jain, L.T. Biegler, M.S. Jhon, Optimization of Polymer Electrolyte Fuel Cell Cathodes, Electrochemical and Solid-State Letters 11 (10) (2008) B193–B196.

[39] S. Ma, C.-H. Solterbeck, M. Odgaard, E. Skou, Microscopy studies on pronton exchange membrane fuel cell electrodes with different ionomer contents, Appl Phys A 96 (2009) 581–589.

[40] R. Madhusudana Rao, R. Rengaswamy, Dynamic characteristics of spherical agglomerate for study of cathode catalyst layers in proton exchange membrane fuel cells, Journal of Power Sources 158 (2006) 110–123.

[41] S. Chan, Q. Tun, Catalyst layer models for proton exchange membrane fuel cells, Chemical Engineering Technology 24 (1) (2001) 51–57.

[42] C. Chen, T. Fuller, Modeling of h2o2 formation in pemfcs, Electrochimica Acta 54 (2009) 3984–3995.

[43] P. Das, X. Li, Z. Liu, A three-dimensional agglomerate model for the cathode catalyst layer of pem fuel cells, Journal of Power Sources 179 (2008) 186–199.

[44] P. Gode, F. Jaouen, G. Lindbergh, A. Lundblad, G. Sundholm, Influence of the compositon on the structure and electrochemical characteristics of the pemfc cathode, Electochimica Acta 48 (2003) 4175–4187.

[45] S. Kamarajugadda, S. Mazumder, Numerical investigation of the effect of cathode catalyst layer structure and composition on polymer electrolyte membrane fuel cell performance, Journal of Power Sources 183 (2008) 629–642.

[46] M. Perry, J. Newman, E. Cairns, Mass transport in gas-diffusion electrodes: A diagnostic tool for fuel-cell cathodes, Journal of the Electrochemical Society 145 (1) (1998) 5–15.

[47] A. A. Shah, G. S. Kim, P. Sui, D. Harvey, Transient non-isothermal model of a polymer electrolyte fuel cell, Journal of Power Sources 163 (2007) 793–806.

[48] Y. Bultel, P. Ozil, R. Durand, Modified thin film and agglomerate models for active layers of p.e. fuel cells, Electrochimica Acta 43 (9) (1998) 1077–1087.

[49] D. Song, Q. Wang, Z. Liu, T. Navessin, M. Eikerling, S. Holdcroft, Numerical optimization study of the catalyst layer of pem fuel cell cathode, Journal of Power Sources 126 (1-2) (2004) 104–111.

[50] D. Song, Q. Wang, Z. Liu, M. Eikerling, Z. Xie, T. Navessin, S. Holdcroft, A method for optimizing distributions of Nafion and Pt in cathode catalyst layers of PEM fuel cells, Electrochimica Acta 50 (16-17) (2005) 3359–3374.

[51] R. Madhusudana Rao, R. Rengaswamy, Optimization study of an agglomerate model for platinum reduction and performance in PEM fuel cell cathode, Chemical Engineering Research and Design 84 (A10) (2006) 952–964.

[52] M. Secanell, B. Carnes, A. Suleman, N. Djilali, Numerical optimization of proton exchange membrane fuel cell cathodes, Electrochimica Acta 52 (7) (2007) 2668–2682.

[53] M. Secanell, K. Karan, A. Suleman, N. Djilali, Optimal design of ultra-low platinum pemfc anode electrodes, Journal of the Electrochemical Society 155(2) (5) (2008) B125–B134.

[54] M. Secanell, Computational modeling and optimization of proton exchange membrane fuel cells, Ph.D. thesis, University of Victoria (November 2007).

[55] Z. Zhang, X. Wang, X. Zhang, F. Yu, Optimizing the performance of a single PEM fuel cell, ASME Journal of Fuel Cell Science and Technology 5 (2008) (031007–)1–9.

[56] M. Secanell, R. Songprakorp, A. Suleman, N. Djilali, Multi-objective optimization of a polymer electrolyte fuel cell membrane electrode assembly, Energy and Environmental Sciences 1 (3) (2008) 378–388.

[57] P. Berg, K. Promislow, J. S. Pierre, J. Stumper, B. Wetton, Water management in PEM fuel cells, Journal of the Electrochemical Society 151 (3) (2004) A341–A353.

[58] B. Carnes, N. Djilali, Systematic parameter estimation for PEM fuel cell models, Journal of Power Sources 144 (1) (2005) 83–93.

[59] Q. Guo, V.A. Sethuraman, R.E. White, Parameter estimates for a PEMFC cathode, Journal of the Electrochemical Society 151 (7) (2004) A983–A993.

[60] P. Jain, L.T. Biegler, M.S. Jhon, Parametric study and estimation in CFD-based PEM fuel cell models, AIChE Journal 54 (8) (2008) 2089–2100.

[61] P. Mukherjee, Q. Kang, C.-Y. Wang, Pore-scale modeling of two-phase transport in polymer electrolyte fuel cells - progress and perspective, Energy and Environmental Science 4 (2) (2011) 346–369.

[62] U. M. Ascher, R. J. Spiteri, Collocation software for boundary value differential-algebraic equations, SIAM J. Sci. Comput. 15 (4) (1994) 938–952.

[63] R. B. Bird, W. E. Stewart, E. Lightfoot, Transport Phenomena, 2nd Edition, J. Wiley and Sons, 2002.

[64] K. C. Neyerlin, W. Gu, J. Jorne, H. A. Gasteiger, Determination of catalyst unique parameters for the oxygen reduction reaction in a PEMFC, Journal of the Electrochemical Society 154 (10) (2006) A1955–A1963.

[65] J. Wang, F. Uribe, T. Springer, J. Zhang, R. Adzic, Intrinsic kinetic equation for oxygen reduction reaction in acidic media: The double tafel slope and fuel cell applications, Faraday Discussions 140 (2008) 347–362.

[66] K. Malek, M. Eikerling, Q. Wang, N. Titichai, Z. Liu, Self-organization in catalyst layers of polymer electrolyte fuel cells, Journal of Physical Chemistry C 111 (36) (2007) 13627–13634.

[67] E. Samson, J. Marchand, J.-L. Robert, J.-P. Bournazel, Modelling ion diffusion mechanisms in porous media, International Journal for Numerical Methods in Engineering 46 (12) (1999) 2043–2060.

[68] D. G. Archer, P. Wang, The dielectric constant of water and debye-h[u-umlaut]ckel limiting law slopes, Journal of Physical and Chemical Reference Data 19 (2) (1990) 371–411.

[69] S. J. Paddison, D. W. Reagor, T. A. Z. Jr., High frequency dielectric studies of hydrated nafion, Journal of Electroanalytical Chemistry 459 (1) (1998) 91–97.

[70] J. Peron, A. Mani, X. Zhao, D. Edwards, M. Adachi, S. T., Z. Shi, Z. Xie, T. Navessin, S. Holdcroft, Properties of nafion nr-211 membranes for pemfcs, Journal of Membrane Science 356 (1-2) (2010) 44–51.

[71] K. Kudo, T. Suzuki, Y. Morimoto, Analysis of oxygen dissolution rate from gas phase into nafion surface and development of an agglomerate model, ECS Transactions 33 (1) (2010) 1495–1502.

[72] T. Springer, T. Zawodzinski, S. Gottesfeld, Polymer electrolyte fuel cell model, Journal of the Electrochemical Society 138 (8) (1991) 2334–2342.

[73] C. K. Mittelsteadt, H. Liu, Handbook of Fuel Cells: Fundamentals, Technology, Applications, Vol. 5, John Wiley & Sons, Ltd, 2009, Ch. 23, pp. 345–358.

[74] L. BekkTech, In-plane conductivity testing procedures & results, Accessed: August 10, 2010 (2007).
URL `http://www1.eere.energy.gov/hydrogenandfuelcells/pdfs/htmwg_bekktech.pdf`

[75] L. Shampine, S. Thompson, J. Kierzenka, G. Byrne, Non-negative solutions of odes, Applied Mathematics and Computation 170 (1) (2005) 556–569.

[76] K. Jiao, X. Li, Water transport in polymer electrolyte membrane fuel cells, Progress in Energy and Combustion Science 37 (3) (2011) 221–291.

[77] Z. Yu, R. N. Carter, Measurement of effective oxygen diffusivity in electrodes for proton exchange membrane fuel cells, Journal of Power Sources 195 (4) (2010) 1079–1084.

[78] M. M. Tomadakis, S. V. Sotirchos, Ordinary and transition regime diffusion in random fiber structures, AIChE Journal 39 (3) (1993) 397–412.

[79] J.H.Nam, M.Kaviany, Effective diffusivity and water-saturation distribution in single- and two-layer PEMFC diffusion medium, International Journal of Heat and Mass Transfer 46 (2003) 4595–4611.

[80] J. Pharoah, K. Karan, W. Sun, On effective transport coefficients in pem fuel cell electrodes: Anisotropy of the porous transport layers, Journal of Power Sources 161 (1) (2006) 301–313.

[81] F. Barbir, PEM Fuel Cells: Theory and Practice, Elsevier Academic Press, 2005.

[82] W. Bangerth, R. Hartmann, G. Kanschat, `deal.II` Differential Equations Analysis Library, Technical Reference.
URL `http://www.dealii.org`

[83] T. A. Davis, Algorithm 832: Umfpack, an unsymmetric-pattern multifrontal method, ACM Transactions on Mathematical Software 30 (2) (2004) 196–199.

[84] COMSOL, COMSOL 3.2 Multiphysics User's Guide (September 2005).

[85] Q. Wang, M. Eikerling, D. Song, Z. Liu, T. Navessin, Z. Xie, S. Holdcroft, Functionally graded cathode catalyst layers for polymer electrolyte fuel cells. I. theoretical modeling, Journal of the Electrochemical Society 151 (7) (2004) A950–A957.

[86] J. X. Wang, T. E. Springer, R. R. Adzic, Dual-pathway kinetic equation for the hydrogen oxidation reaction on pt electrodes, Journal of the Electrochemical Society 153 (9) (2006) A1732–A1740.

[87] M. Secanell, B. Carnes, A. Suleman, N. Djilali, A PEM fuel cell cathode model for gradient-based optimization, in: III European Conference on Computational Mechanics, ECCOMAS, 2006.

[88] G. Bender, M. S. Wilson, T. A. Zawodzinski, Further refinements in the segmented cell approach to diagnosing performance in polymer electrolyte fuel cells, Journal of Power Sources 123 (2) (2003) 163–171.

[89] E. L. Cussler, Diffusion : Mass Transfer in Fluid Systems, 2nd Edition, Cambridge University Press, 1997.

[90] K. Karan, Assessment of transport-limited catalyst utilization for engineering of ultra-low pt loading polymer electrolyte fuel cell anodes, Electrochemistry Communications 9 (4) (2007) 747–753.

[91] S. Chen, A.Kucernak, Electrocatalysis under conditions of high mass transport rate: Oxygen reduction on single submicrometer-sized pt particles supported on carbon, Journal of Physical Chemistry B 108 (10) (2004) 3262–3276.

[92] P. Dobson, M. Secanell, Least-squares parameter estimation for catalyst layer agglomerate models, ASME Conference Proceedings 2010 (44045) (2010) 795–804.

[93] M. Eldred, et al., Dakota, a multilevel parallel object-oriented framework for design optimization, parameter estimation, uncertainty quantification, and sensitivity analysis. version 5.0 users manual., Tech. Rep. SAND2010-2183, Sandia National Laboratory (2010).

[94] J. E. Dennis Jr., D. M. Gay, R. E. Welsch, Adaptive nonlinear least-squares algorithm., ACM Transactions on Mathematical Software 7 (3) (1981) 348–368.

[95] D. E. Finkel, DIRECT Optimization Algorithm User Guide (2003).
URL `http://www.ncsu.edu/crsc/reports/ftp/pdf/crsc-tr03-11.pdf`

[96] S. TE, W. MS, S. Gottesfeld, Modeling and experimental diagnostics in polymer electrolyte fuel cells, Journal of the Electrochemical Society 140 (12) (1993) 3513–26.

[97] P. Dobson, M.Secanell, D. Song, Microscale optimization modeling: Advanced PEMFC for Near Term Commercialization Products, Tech. Rep. 9 (January 2011).

[98] P. Dobson, M.Secanell, D. Song, Microscale optimization modeling: Advanced PEMFC for Near Term Commercialization Products, Tech. Rep. 10 (Arpil 2011).

Appendices

Appendix A

Mathematical Derivations

A.1 Ionomer-Filled Agglomerate Model

A.1.1 Formulation of Model Equations

The derivation of an analytical solution for an ionomer-filled agglomerate model used in this work is described in this section. The description of the transport properties of oxygen in the agglomerate is presented in section 2.2. The model equations here start with an analysis of the oxygen flux through the thin film.

$$N_{O_2} = -D_{O_2,N} \frac{\mathrm{d}c_{O_2}}{\mathrm{d}r} \tag{A.1}$$

A solution is obtained by defining a the flux in the thin film equal to the consumption of oxygen in the agglomerate core, F_{O_2}, through the surface of the agglomerate.

$$F_{O_2} = -N_{O_2} \cdot 4\pi r^2 \tag{A.2}$$

$$\frac{\mathrm{d}c_{O_2}}{\mathrm{d}r} = \frac{1}{4\pi r^2} \frac{F_{O_2}}{D_{O_2,N}} \tag{A.3}$$

If the consumption of oxygen is constant, the integral becomes

$$\int_{r_{agg}}^{(r_{agg}+\delta_{agg})} \mathrm{d}c_{O_2} = \frac{F_{O_2}}{4\pi D_{O_2,N}} \int_{r_{agg}}^{(r_{agg}+\delta_{agg})} \frac{1}{r^2} \mathrm{d}r \tag{A.4}$$

$$c_{O_2}\left(r_{agg}+\delta_{agg}\right) - c_{O_2}\left(r_{agg}\right) = \left[\frac{F_{O_2}}{4\pi D_{O_2,N}} \frac{-1}{r}\right]_{r_{agg}}^{(r_{agg}+\delta_{agg})} \tag{A.5}$$

The boundaries are defined by the outer boundary - the gas/liquid interface (g/l) - and the inner boundary between the hydrated electrolyte and the solid-porous agglomerate core - the liquid/solid interface (l/s). Substituting and rearranging the equation yields

$$\frac{c_{O_2,(g|l)} - c_{O_2,(l|s)}}{\delta_{agg}} = \frac{1}{r_{agg}\left(r_{agg}+\delta_{agg}\right)} \frac{F_{O_2}}{4\pi D_{O_2,N}} \tag{A.6}$$

The concentration at the outer boundary is given by Henry's Law: $c_{O_2,(g|l)} = \frac{P_{O_2}}{H_{O_2,N}}$. To obtain the value at the inner boundary, all that remains is to define the consumption of oxygen in the agglomerate.

If an effectiveness factor (E_r) is defined as the average reaction in the agglomerate as a fraction of the reaction at the surface, the total reaction rate can be defined as

$$R_{O_2} = E_r k_c c_{O_2,(l|s)} \tag{A.7}$$

where k_c is the reaction rate at the surface for an oxygen concentration of $c_{O_2,(l|s)}$.

$$k_c = \frac{A_v}{(1-\varepsilon_V)} \frac{i_0^{ref}}{4F c_{O_2}^{ref}} \exp\left[\frac{\alpha_c F}{RT}\left(E_0 - (\phi_s - \phi_m)\right)\right] \tag{A.8}$$

The term $(1-\varepsilon_V)$ comes from the scaling of the active area, i.e.

$$A_{v(agg)} = \frac{A_v}{(1-\varepsilon_V)} \tag{A.9}$$

Typically, the active area for an electrode is given as the area per volume of catalyst layer. Since the agglomerate deals only with the solid and electrolyte phases, dividing by $(1-\varepsilon_V)$ gives the active area of Pt (cm^2_{Pt}) per volume of agglomerate (cm^3_{agg}). The equation for the effectiveness factor comes from the analytical solution of the system on the agglomerate domain.

$$E_r = \frac{1}{\phi_L}\left(\frac{1}{\tanh(3\phi_L)} - \frac{1}{3\phi_L}\right) \tag{A.10}$$

where ϕ_L is Thiele's modulus, which characterizes the reaction-transport process for a given geometry. For a sphere, the characteristic length is $\frac{r_{agg}}{3}$, so Thiele's modulus becomes

$$\phi_L = \frac{r_{agg}}{3}\sqrt{\frac{k_c}{D_{O_2}^{eff}}} \tag{A.11}$$

These equations allows for the definition of the total oxygen consumption within the agglomerate.

$$F_{O_2} = R_{O_2} V_{agg} = E_r k_c c_{O_2,(l|s)}\left(\frac{4\pi r_{agg}^3}{3}\right) \tag{A.12}$$

Substituting equation (A.12) into equation (A.6) for the concentration profile in the thin-film,

$$\frac{P_{O_2}}{H_{O_2,N}} - c_{O_2,(l|s)} = \frac{\delta_{agg}}{r_{agg}\left(r_{agg}+\delta_{agg}\right)} \frac{E_r k_c c_{O_2,(l|s)}}{4\pi D_{O_2,N}}\left(\frac{4\pi r_{agg}^3}{3}\right) \tag{A.13}$$

$$c_{O_2,(l|s)} = \frac{P_{O_2}}{H_{O_2,N}} \left[\frac{\delta_{agg} r_{agg}^2}{3\left(r_{agg} + \delta_{agg}\right)} \frac{E_r k_c}{D_{O_2,N}} + 1 \right]^{-1} \tag{A.14}$$

Now, the volumetric reaction rate in the agglomerate is given by equation (A.7). However, the current density is what is of particular interest in the simulation. Furthermore, the current density is based on the size of the agglomerate, not the entire domain. Therefore, a multiplying factor is required to transform the reaction rate per volume of the agglomerate core, to the current density of the entire agglomerate. First, the volume scaling factor is defined.

$$\bar{V}_{agg} = \frac{V_{agg}}{V_{tot}} = \frac{\frac{4\pi r_{agg}^3}{3}}{\frac{4\pi(r_{agg}+\delta_{agg})^3}{3}} = \frac{r_{agg}^3}{\left(r_{agg} + \delta_{agg}\right)^3} \tag{A.15}$$

Next, Faraday's constant and the reaction stoichiometry of the half reaction is applied to obtain the volumetric current density for the agglomerate, which can now be expressed as

$$i_{agg} = 4F\bar{V}_{agg} E_r k_c c_{O_2,(l|s)} \tag{A.16}$$

Substituting equation (A.14) for oxygen concentration into equation (A.16) for the current density,

$$i_{agg} = 4F\bar{V}_{agg} \frac{P_{O_2}}{H_{O_2,N}} \left[\frac{E_r k_c}{\frac{\delta_{agg} r_{agg}^2}{3(r_{agg}+\delta_{agg})} \frac{E_r k_c}{D_{O_2,N}} + 1} \right] \tag{A.17}$$

Rearranging,

$$i_{agg} = 4F\bar{V}_{agg} \frac{P_{O_2}}{H_{O_2,N}} \left[\frac{1}{E_r k_c} + \frac{\delta_{agg} r_{agg}^2}{3\left(r_{agg} + \delta_{agg}\right) D_{O_2,N}} \right]^{-1} \tag{A.18}$$

A.1.2 Alternate Formulation

The model developed above for this work differs from that derived by Sun et al. [4] and subsequently used by Secanell et al. [33] and many others. This section clarifies the derivation of the model presented in the literature.

The solution is obtained by assuming that the constant rate of consumption can be expressed in terms of the flux through the surface (at the inner or outer boundary, since the flux is constant). This assumption is only valid assuming that the concentration profile within the thin film is linear. Sun et al. [4] make this assumption by claiming δ_{agg} will always be small compared to the radius. Substituting for $F_{O_2} = N_{O_2} \cdot 4\pi r^2$ in equation (A.6),

$$\frac{c_{O_2,(g|l)} - c_{O_2,(l|s)}}{\delta_{agg}} = \frac{1}{r_{agg}\left(r_{agg} + \delta_{agg}\right)} \frac{N_{O_2} \cdot 4\pi r^2}{4\pi D_{O_2,N}} \tag{A.19}$$

Evaluating at the outer boundary, $r = r_{agg} + \delta_{agg}$, where $c_{O_2,(g|l)} = \frac{P_{O_2}}{H_{O_2,N}}$ by Henry's law, the flux through the agglomerate is obtained.

$$N_{O_2} = D_{O_2,N} \left[\frac{P_{O_2}}{H_{O_2,N}} - c_{O_2,(l|s)} \right] \frac{r_{agg}}{\delta_{agg} \left(r_{agg} + \delta_{agg} \right)} \tag{A.20}$$

However, the full area of the spherical agglomerate is not available to dissolve oxygen from a gas into the electrolyte since the catalyst layer is a continuous network of solid and electrolyte. If the consumption of oxygen is described on a 'per volume' basis, the reaction rate in the catalyst layer is given by

$$R_{O_2} = N_{O_2} a_{agg} \ \left[\frac{mol}{cm^3_{CL} s} \right] \tag{A.21}$$

where a_{agg} is the available surface area per unit volume of catalyst layer. An expression for this value is given by Secanell et al. [33]. Using Thiele's modulus, R_{O_2} can be obtained analytically for the reaction-diffusion process in the agglomerate, assuming the source term is linear with respect to oxygen concentration.

$$R_{O_2} = E_r k_c c_{O_2,(l|s)} \tag{A.22}$$

Similar to the derivation above, the active area in the catalyst layer is transformed into the active area in the agglomerate by excluding the volume fraction of void space in the catalyst layer, $(1 - \varepsilon_V)$. Consequently, equation (A.22) must be scaled back to the catalyst layer level. However, it is important to note that this correction is already applied to the reaction rate k_c, identical to equation (A.8). A detailed explanation of this step is not given by Sun et al. [4], so it is unclear why the change in the reference volume back to the catalyst layer level is applied at this stage.

$$R_{O_2} = \left(1 - \varepsilon_V\right) E_r k_c c_{O_2,(l|s)} \tag{A.23}$$

The final result will be an equation with mixed units of volume. Nevertheless, the expression can be derived by again following a similar procedure of substitution as above. The equation for concentration at the inner boundary becomes

$$D_{O_2,N} \left[\frac{P_{O_2}}{H_{O_2,N}} - c_{O_2,(l|s)} \right] \frac{r_{agg}}{\delta_{agg} \left(r_{agg} + \delta_{agg} \right)} a_{agg} = \left(1 - \varepsilon_V\right) E_r k_c c_{O_2,(l|s)} \tag{A.24}$$

Expressing this reaction rate in terms of current density per volume of catalyst layer,

$$i = 4F R_{O_2} = 4F \left(1 - \varepsilon_V\right) E_r k_c c_{O_2,(l|s)} \tag{A.25}$$

Finally, the concentration at the internal boundary can be eliminated and an equation for the current density can be obtained.

$$i = 4F\frac{P_{O_2}}{H_{O_2,N}}\left(\frac{1}{(1-\varepsilon_V)\,E_r k_c} + \frac{\delta_{agg}\,(r_{agg}+\delta_{agg})}{r_{agg}a_{agg}D_{O_2,N}}\right)^{-1} \tag{A.26}$$

To compare these two solutions, the current given in equation (A.18) must be scaled to a *per volume of catalyst layer* basis.

$$i_{agg} = 4F\bar{V}_{agg}\frac{P_{O_2}}{H_{O_2,N}}\left[\frac{1}{E_r k_c} + \frac{\delta_{agg}r_{agg}^2}{3\,(r_{agg}+\delta_{agg})\,D_{O_2,N}}\right]^{-1}$$

must therefore be reformulated to include a $(1-\varepsilon_V)$ term for scaling.

$$i_{agg} = 4F\bar{V}_{agg}\,(1-\varepsilon_V)\,\frac{P_{O_2}}{H_{O_2,N}}\left[\frac{1}{E_r k_c} + \frac{\delta_{agg}r_{agg}^2}{3\,(r_{agg}+\delta_{agg})\,D_{O_2,N}}\right]^{-1} \tag{A.27}$$

These equations differ slightly, but give a vast difference in current density predictions. Volume scaling by $\bar{V}_{agg}$ aside, there are two notable differences. The first is the definition of a_{agg}, which is a scaling factor that is used to represent a reduction in the available area for oxygen dissolution based on the three-dimensional structure of the catalyst layer. Physically, this is very difficult to define and can have a profound impact on when diffusion resistance begins to dominate in the cell. The author recommends that a 3-D model or a surrogate be used to study anisotropy of the agglomerate in the catalyst layer. Furthermore, it has been shown that this definition available area is unnecessary if the reaction is defined on a volumetric basis (see equation (A.12)) rather than by the flux through the surface.

The second is the method of scaling the variables to the catalyst layer level. The method presented in this work defines the reference volume as the agglomerate. As such, only a single scale transformation is required for a variable (A_v) determined experimentally based on the volume of the CL. While catalyst scale modeling requires a transformation back to a different unit volume, this can be easily applied after the result for the agglomerate current is obtained. In the derivation presented in [4] the multiple transformations become difficult to account for, and prone to error. The resulting equation of (A.26) actually defines the current on the agglomerate scale with the active area defined on the catalyst layer scale. This equation of mixed units is not evident, but its discovery leads to a better understanding of agglomerate models.